Title

Development of Magnetic Resonance Imaging Techniques to Visualize Gas-Solid Reactions in situ

Author

Jarenwattananon, Nanette Nalatporn

Publication Date

2017

UNIVERSITY OF CALIFORNIA
Los Angeles

Development of Magnetic Resonance Imaging Techniques to Visualize Gas-Solid Reactions *in situ*

A dissertation submitted in partial satisfaction
of the requirements for the degree
Doctor of Philosophy in Chemistry

by

Nanette Nalatporn Jarenwattananon

2017

ABSTRACT OF THE DISSERTATION

Development of Magnetic Resonance Imaging Techniques to Visualize Gas-Solid Reactions *in situ*

by

Nanette Nalatporn Jarenwattananon
Doctor of Philosophy in Chemistry
University of California, Los Angeles, 2017
Professor Louis-Serge Bouchard, Chair

More than 85% of all chemical industry products are made using catalysts, the overwhelming majority of which are heterogeneous catalysts that function at the gas-solid interface. Consequently, much effort is invested in optimizing the design of catalytic reactors, usually by modeling the coupling between heat transfer, fluid dynamics, and surface reaction kinetics. The complexity involved requires a calibration of model approximations against experimental observations, with temperature maps being particularly valuable because temperature control is often essential for optimal operation and because temperature gradients contain information about the energetics of a reaction. However, it is challenging to probe the behavior of a gas inside a reactor without disturbing its flow, particularly when trying also to map the physical parameters and gradients that dictate heat flow, mass flow, and catalytic efficiency. Although optical techniques and sensors have been used for that purpose, the former perform poorly in opaque media and the latter perturb the flow. NMR thermometry can measure temperature non-invasively, but traditional approaches applied to gases produce signals that depend only weakly on temperature, are rapidly attenuated by diffusion, or require contrast agents that may interfere with reactions. In this dissertation, we present a new NMR thermometry technique that circumvents these problems by exploiting the inverse relationship between NMR linewidths and temperature caused by motional averaging in a weak magnetic field gradient.

The motional averaging behavior of gases is fundamentally different from that of liquids, which can be explained using a more detailed theoretical description of the dephasing function that accounts for position autocorrelation effects. The traditional view of nuclear-spin decoherence in a field gradient predicts that in a fluid, NMR linewidth should increase with temperature; however, in gases we observed the opposite behavior. Furthermore, in an inhomogeneous field, the nuclear free induction decay signal exhibits fundamentally different time dependence between gases and liquids. The Carr-Purcell-Meiboom-Gill (CPMG) experiment has been used for decades to measure nuclear-spin transverse (T_2) relaxation times. In the presence of magnetic-field inhomogeneities, the limit of short interpulse spacings yields the intrinsic T_2 time. In gases, CPMG unexpectedly fails to eliminate the inhomogeneous broadening due to the non-Fickian nature of the motional averaging.

We exploit the motional averaging behavior of gases by non-invasively mapping gas temperatures during the hydrogenation of propylene in reactors packed with metal nanoparticles and metal-organic framework catalysts, with measurement errors of less than 4% of the absolute temperature. These results establish our technique as a non-invasive tool for locating hot and cold spots in catalyst-packed gas-solid reactors, with unprecedented capabilities for testing the approximations used in reactor modeling.

The dissertation of Nanette Nalatporn Jarenwattananon is approved.

Peter M. Felker

Jacob J. Schmidt

Louis-Serge Bouchard, Committee Chair

University of California, Los Angeles
2017

To my family, who have supported me through this journey.

Table of Contents

1 Introduction 1

1.1 Principles of NMR 1

1.1.1 Classical description of NMR 1

1.1.2 Main field B_0 2

1.1.3 Radiofrequency field B_1 3

1.1.4 Magnetic field gradients g 4

1.1.5 Free precession and Fourier transform NMR 4

1.1.6 Relaxation times 5

1.1.7 Bloch equations 6

1.1.8 Chemical shift 7

1.1.9 Spin echoes 7

1.2 *Operando* Measurements of Chemical Reactions 7

1.2.1 Heterogeneous catalysis 8

1.2.2 Microreaction technology 8

1.2.3 NMR imaging of heterogeneous reactions 10

2 Motional Averaging of Nuclear Resonance in a Field Gradient 12

2.1 Experimental Results and Discussion 17

2.2 Supplementary Data Analysis and Sample Data 20

2.2.1 Linewidth vs. temperature data 20

2.2.2 Linewidth vs. gradient data 20

2.2.3 Determination of error bars 21

2.3 Experimental Methods 21

2.3.1 Sample preparation 21
2.3.2 NMR methods 21
2.3.3 Temperature control 22

3 Breakdown of CPMG Spin Echoes in Inhomogeneous Fields 26
3.1 Experimental Results and Discussion 29
3.2 Control Experiments 32
3.2.1 Phase cycling and RF homogeneity 32
3.2.2 Convection currents 33
3.2.3 The free diffusion regime 36
3.2.4 Supplementary Equations 37

4 Thermal Maps of Gases in Heterogeneous Reactions 39
4.1 Experimental Results and Discussion 39
4.2 Supplemental Equations 46
4.2.1 Single component gases 46
4.2.2 Multiple component gas mixtures 48
4.2.3 Temperature in heterogeneous media 50
4.3 Control Experiments and Experimental Methods 53
4.3.1 NMR pulse sequence 53
4.3.2 Experimental set-up 54
4.3.3 Steady conditions 55
4.3.4 Image voxel geometry 56
4.3.5 Field-of-view alignment 57
4.3.6 Fiber-optic probe geometry 58
4.3.7 Effect of gradient direction 58

4.3.8 Effects of reaction rate 60
4.3.9 Temperature coefficients of single component gases 62
4.3.10 Temperature coefficients of gas mixtures 64
4.3.11 Temperature coefficients in heterogeneous media 64
4.3.12 Origin of the inhomogeneous lineshape in heterogeneous media 66
4.3.13 PtNP catalyst preparation 71
4.3.14 Pd-MOF catalyst preparation 71
4.3.15 Calibration of motional-averaging technique 73
4.3.16 Temperature mapping 73
4.3.17 T_1 relaxometry 73
4.3.18 T_2 relaxometry 74
4.3.19 Microreactor imaging 74

5 Concluding Remarks 75

A Pulse Sequences 77
A.1 Bruker Pulse Sequences 77
A.1.1 Spectroscopy Sequences 77
A.1.2 Imaging Sequences 80
A.2 Varian Pulse Sequences 83
A.2.1 Spectroscopy Experiments 83
A.2.2 Imaging Experiments 93

References 119

List of Figures

2.1 Measurement of molecular self-diffusion in a constant field gradient. A 90° radiofrequency (rf) pulse tips the magnetization. This resulting nuclear induction signal is measured in a constant gradient of amplitude g. The time evolution of magnetization, as described by the textbook [1–3] expression (Eq. 2.1), interrogates the molecular self-diffusion process. 13

2.2 Validation of the $T^{-1/2}$ law in the high-temperature regime ($T > C$) for gases. The values of $\ln T$ shown correspond to the temperature range $T = 180 - 490$ K. Three different gases were investigated: methane, acetylene, and propylene. The temperature dependence on linewidth (scaled to gradient strength) was found to be $\Delta f \propto T^{-0.47\pm0.04}$ (averaged over the three gases). Although different values of the applied gradient g are shown here to avoid overlapping of the curves (methane, g=0.15 G/cm; acetylene, g=0.07 G/cm; propylene, g=0.1 G/cm), the scaled linewidth is independent of g. 18

2.3 Temperature dependence of linewidth (Δf) in liquids. Nine different liquids were investigated, as shown by the different symbols. The values of $\ln(T)$ shown span the temperature range $T = 180 - 450$ K. A) For a fixed gradient strength of g=0.05 G/cm, all linewidths were broadened by a similar amount, hence the overlap in the data. At fixed g, the linewidth did not exhibit any detectable dependence on temperature. B) Increasing applied gradient strength did not alter the independence of linewidth on temperature. Applied gradient strengths were: nitromethane (1 G/cm), dichloromethane (dcm, 0.5 G/cm), acetonitrile (0.4 G/cm), chloroform (0.3 G/cm), benzene (0.3 G/cm), water (0.2 G/cm), trifluoroacetic acid (tfa, 0.1 G/cm), dimethyl sulfoxide (dmso, 0.1 G/cm), acetone (0.05 G/cm). Symbol in A refers to the same liquid as in B. 23

2.4 Dependence of linewidth (Δf) on applied gradient strength (g) for gases. Three different gases were investigated. Two different regimes are found: in the limit of strong applied gradients, Δf scales as $g^{1.0\pm0.1}$ whereas for weak gradients Δf scales as $g^{1.8\pm0.2}$. All data was acquired at ambient temperature. 24

2.5 Dependence of linewidth (Δf) on gradient strength (g) for liquids. Nine different liquids were investigated. Two different regimes are found: in the limit of strong applied gradients, Δf scales as $g^{1.1\pm0.1}$ whereas for weak gradients Δf scales as $g^{2.0\pm0.2}$. All data was acquired at ambient temperature. 24

2.6 A) Raw linewidth vs. temperature data for methane gas. The applied gradient strength was $g = 0.15$ G/cm, with FOV = 78 cm. B) Raw linewidth vs. temperature data for liquid dichloromethane. The applied gradient strength was $g = 0.3$ G/cm, with FOV = 94 cm. 25

2.7 A) Raw linewidth vs. gradient data for methane gas, acquired at 220 K. B) Raw linewidth vs. gradient data for liquid dichloromethane, acquired at 300 K. The continuous curves drawn through the data points are guides to the eye, and are not actual fits. 25

3.1 Measurement of T_2 in an inhomogeneous field (gradient, g) using a CPMG sequence. A 90° radio-frequency (r.f.) pulse tips the magnetization, which is refocussed by a series of n 180° pulses at intervals of 2τ. 27

3.2 Direct verification that signal decay in the presence of a magnetic-field gradient follows a time dependence of the form $\exp(-t/T_2)\exp(-t/b)$ for the gas and $\exp(-t/T_2)\exp(-(t/b_2)^3)$ for the liquid (solid lines, fit; dots, data). Here we show sample CPMG decay curves for τ=5 ms and g=0, 0.01, 0.05 and 0.5 G/cm. (a) Liquid-phase TMS (t^1). Number of scans (ns) = 1. (b) Gas-phase TMS (t^3). ns = 8. In both liquid and gas cases, we scanned multiple acquisitions (of ns = 1 and 8 for liquid and gas respectively) and a T_2 value with experimental error bars was derived for Figure 3. The fits to the respective models are excellent. Fits to the converse equation ($t^1 \leftrightarrow t^3$) do not yield acceptable fits (not shown here). 30

3.3 T_2 relaxation time of tetramethylsilane (TMS) vs interpulse spacing τ under conditions of magnetic field inhomogeneity (field gradient g, in G/cm). (a) Liquid-phase T_2 values approach the limit of no applied gradient as $\tau \to 0$. T_2 values shown range from 50 ms to 20 s. τ values shown range from 1 ms to 100 ms. Inset: Expansion of red boxed region. (b) Gas-phase T_2 values do not converge to a single value as $\tau \to 0$. T_2 values shown range from 18 ms to 1 s. τ values shown range from 1 ms to 100 ms. Inset: Expansion of red boxed region in A. (c) Data from (a) plotted on a linear scale. The straight lines are linear extrapolations as $\tau \to 0$. The g values are the same as in (a). (d) Data from (b) plotted on a linear scale. The straight lines are linear extrapolations as $\tau \to 0$. The g values are the same as in (b). 31

3.4 Signal decay of echo envelopes from multiple-spin-echo experiment in liquid water. τ = 10 ms. The trace was acquired in a single-shot; the points shown are the sum of signal for each echo, integrated over the time window between two consecutive RF pulses. The green trace is the phase cycling 90°_x–$(180^\circ_y$–$180^\circ_{-y})_n$ (green trace), and the "CPMG" phase cycling used in the paper 90°_x–$(180^\circ_y$–$180^\circ_y)_n$ (red squares) overlap almost perfectly. 33

3.5 Comparison of composite pulses vs regular hard pulses in a multiple-spin echo experiment. The decay rates are seen to be nearly identical. τ = 10 ms . . . 34

3.6 Temperature maps (axial images) of propylene gas in the NMR tube. The temperatures are derived from the “temperature coefficient” that relates NMR linewidth to temperature. The temperature dependence is described in [4]. The temperature mapping method is described in [5]. 34

3.7 Gas inside a porous media also displays temperature dependence of NMR linewidth as a function of applied gradient strength. 35

3.8 Pure gas displays temperature dependence of NMR linewidth as a function of applied gradient strength. 36

4.1 a) At higher temperatures, gas molecules move faster and molecular motion averages the effects of the dephasing gradient. Because the spins experience more of the average magnetic field, linewidths are narrower. FWHM, full-width at half-maximum. b) Without a gradient, the linewidth is weakly dependent on temperature. As we turn on the external gradient, the linewidth dependence on temperature grows and becomes independent of the nature of the porous medium. c) In the calibration experiment of b, we fit the propylene spectrum at each temperature to a sum of Lorentzian distributions to extract the linewidth. Temperature calibrations were performed for over 30 different systems. The particular data shown in b is an example of one system. 40

4.2 Orthogonal slices of the system determined by micro-computed tomography. The reactor shown here consists of a 10-mm Pyrex NMR tube, a gas inlet tube and a heterogeneous catalyst loaded on glass wool. To validate the NMR method, independent temperature measurements were made using fiber-optic probes placed at three different locations (arrows) within the NMR field of view (FOV). The approximate location of the FOV is indicated by the dashed box. The axial, coronal and sagittal planes correspond to those in Fig. 4.3. . 41

4.3 a), b) Two-dimensional NMR signal-to-noise ratio (SNR) maps (greyscale) and corresponding gas-phase thermal maps (color) of one reactor packed with 10-mm PtNP (a) and another packed with Pd-MOF (b). SNR maps detail the signal intensity of proton resonances used to derive the temperature. Each pixel corresponds to an in-plane, 0.73 mm × 0.73 mm region and is assigned a linewidth-based temperature. Temperature was calculated only for pixels with SNR$>$ 4 (blue outline). The temperature measurement was confirmed by fiber-optic temperature sensors placed within the FOV, indicated by circles on the thermal maps. Sensor probe alignment relative to the reactor is shown in Fig. 4.2. Thermal maps were generated for more than 15 experiments. The particular thermal maps shown above are two representative examples of those maps. 42

4.4 Signal enhancement from para-state hydrogen was used to provide detailed views inside the microreactor, which was held at approximately 418 K by using a variable temperature controller to preheat the gas flowing through a heat exchange radio-frequency (RF) coil. a) Schematic view; b) thermal map. The temperature calibration coefficient was 0.200 ± 0.006 Hz/K. The thermal map depicts temperature changes relative to the incoming gas. Spatial distributions of linewidths were mapped on five different reactors prepared similarly. Each reactor exhibited comparable heterogeneity in the temperature distributions. 45

4.5 Position autocorrelations $\langle x(t)x(0)\rangle/\langle x^2\rangle$ for particle motion driven by viscous thermal noise in the case of overdamped, underdamped and critically damped motion. For reference, the exponential decay $\exp(-t\gamma/2m)$ is shown ($\gamma = 1$, $m = 1$, $kT = 1$). 47

4.6 Temperature dependence of the NMR line broadening for several different values of the Sutherland constant C. The Sutherland constant separates the two temperature regions $\Delta f \sim T^{-7/2}$ $(T < C)$ and $\Delta f \sim T^{-1/2}$ $(T > C)$. For this calculation, we used $M/m = 10^{10}$, $g = 0.1$ G/cm and $\gamma_n = 2\pi \cdot 42.2 \times 10^6$ rad/s/T. 49

4.7 Temperature dependence of the NMR linewidth for a gas mixture (50-50) of propane and ammonia. Line broadening for the pure gases of individual components is shown for comparison. For this calculation, we used $M/m = 10^{10}$, $g = 0.1$ G/cm and $\gamma_n = 2\pi \cdot 42.2 \times 10^6$ rad/s/T. 50

4.8 Examples of porous media. (a) Glass wool. (b) Metal nanoparticles. (c) Two-phase random medium with σ-phase (solid) and β-phase (fluid). Flow/-transport is indicated by the arrows. The dotted circle denotes the averaging volume V. 51

4.9 NMR pulse sequence for acquisition of thermal maps. Only a single shot (no repetition) is shown. To get a 2D image, this sequence is repeated $n_1 \times n_2$ times while stepping the G_P gradient through the 2D phase encode scheme, where $n_1 \times n_2$ is the number of phase encode steps. 54

4.10 Experimental setup for acquistion of thermal maps. 55

4.11 NMR spectrum of the hydrogenation reaction catalyzed by Pd-MOF in a 10 mm reactor. The reaction was monitored for several hours and exhibits a constant conversion rate over time. 56

4.12 Temporal stability of thermal maps during the reaction. The hydrogenation reaction was catalyzed by Pd-MOF in a 5 mm reactor. Over the course of several hours, the reaction demonstrates constant conversion rate over time (Figure 4.11) as well as stable temperatures, as shown here. 57

4.13 Geometry of the image voxel. (a) 3D perspective view of a voxel from a coronal or sagittal projection in relation to the NMR tube. (Only a short section of the NMR tube is shown.) (b) 2D top view. The size of the voxel relative to the NMR tube is exaggerated for illustration purposes. Roughly speaking, the shape of the gas volume giving rise to NMR signal within a voxel is that of a horizontally-aligned parallepiped intersected with a vertical cylinder. . 58

4.14 Thermal maps acquired using x versus y gradients yield similar results within 4% error. The upper row corresponds to axial images acquired with a temperature gradient along the x-direction, and the lower row corresponds to axial images acquired with a temperature gradient along the y-direction. 59

4.15 Concentration map of propane (reaction product) in the YZ plane of the catalytic reactor using MOF catalyst. Together with knowledge of the flow velocity, this map yields convective and diffusive transport contributions to the conservation of mass species, from which we obtain the reaction rates. The reaction rates are averaged in a region of interest (ROI) over the heterogeneous medium (example ROI shown in white) to yield the average timescale of the reaction. 61

4.16 Packed bed reactors containing silica gel, ZIF-8, and Pd-MOF. The RF region of each reactor is boxed. 67

4.17 (a) Spectroscopic imaging produces a gas density image of the PtNP reactor system, in which each voxel contains its own NMR spectrum. Voxel size is approximately 0.7×0.7 mm^2. (b) At each voxel, linewidth Δf is determined by the full width at half maximum (FWHM) of a resonance. In the presence of applied magnetic field gradient G_T, the FWHM of the methyl resonance is broadened by a factor of 5. Here we compare the linewidth prior to reaction and without gradient G_T to the linewidth during a reaction with an applied gradient G_T. 69

4.18 Maps of the finite differences in temperatures between nearest-neighbor points relative to the local temperature: $(\Delta_x T)/T$ and $(\Delta_y T)/T$. These maps represent the differences in temperature between neighboring voxels (along x or y). For temperature profiles which are monotonic across a voxel, this finite difference provides an "upper bound" for the magnitude of the temperature gradient within a voxel. As can be seen, these internal gradients over a voxel are fairly small on average ($< 4\%$). Points near or at the edges are unphysical due to the large derivatives at the boundaries. 70

4.19 Typical length scales in a PtNP reactor system. (a) Thermal maps of of the PtNP reactor system. (b) Magnitude of ∇T, the numerical gradient of temperature across the PtNP reactor. (c) μ-CT images of NMR reactor. . . 72

List of Tables

4.1 Temperature coefficients for propylene at different applied gradient strengths. Pressure is 1.0 atm. 63

4.2 Temperature coefficients for three pressures of propylene. Typical error associated with these measurements is ± 0.01 Hz/K for the 0.0 mG/cm and 5.3 mG/cm systems, and 0.03 Hz/K for the 26.5 mG/cm system. 63

4.3 Temperature coefficients for propylene/ethane mixtures. Typical error associated with these measurements is ± 0.01 Hz/K for the 0.0 mG/cm and 5.3 mG/cm systems and ± 0.02 Hz/K for the 10.6 mG/cm system. Ratios given (2/3 and 1/14) are ratios of gas pressures. Total pressure of the mixtures in each tube was 2.0 atm. 65

4.4 Temperature coefficients for various types of packed-bed catalytic reactors. The typical error bar associated with these measurements on heterogeneous media is ± 0.01 Hz/K, ± 0.03 Hz/K and ± 0.09 Hz/K for the 0.0 mG/cm, 26.5 mG/cm, and 53.0 mG/cm systems, respectively. Pressures of each system were approximately 2.7 atm. 66

Acknowledgments

A great many people have contributed to my scientific education, my dissertation research, and my motivation to complete this dissertation. All of them have been integral to this body of work. Thank you. Dr. Keith Heidmann at Shorewood High School first got me interested in chemistry with his zany, enjoyable, and most importantly, understandable lectures. Profs. Dina Merrer, Marisa Buzzeo, and Sally Chapman, and Drs. Meena Rao and Jean Vadakkan inspired me to continue studying chemistry at Barnard College. At UCLA, my dissertation committee: Profs. Benjamin J. Schwartz, Peter M. Felker, Jacob J. Schmidt, and my advisor, Louis Bouchard have shaped me into the scientist I am now. My thanks and gratitude go to my classmates, collaborators, coworkers, and colleagues. In college, WKCR gave me a place to go when I needed to get out of lab; thank you Phil Schaap, Susanna Mendlow, and Ben Young. Jenna Bass, Dr. Brisa Hurlocker, Marina Orman, Olga Sokolovskya, and Dr. Stephanie Zaleski helped me get through hours of problem sets and quantitative analysis. From the Bouchard group, I want to thank all lab members and specifically Dr. Jonathan W. Brown and Dr. Stefan Glöggler, Alex Grunfeld, Jeff McCormick, Robin Möller-Gulland, and Trenton Otto. From the Molecular Instrumentation Center (MIC), I would like to thank Drs. Jane Strouse, Bob Taylor, Dafni Amirsakis, and Ignacio Martini for their support. Many others affiliated with UCLA, but neither MIC nor my research group, have also helped me stay sane over the years– my pchem cohort: John Abendroth, Erik Farr, Matt Fontana, and Devon Widmer; Dr. Chris Arntsen; Mary E.E. Clark and the rest of the UCLA Powerlifting team; Dr. Ben Finck; Gordon Huang; Dr. Kevin Miller; Steph Quan; and Dr. Michael T. Yeung. Finally, my family: thanks Mom, Dad, PJ, and of course my dog, Meebo.

Chapter 2 includes material that has been previously published in [4, 6, 7]. Chapter 3 includes material that has been submitted to *Physical Review Letters*, and is in revision. Chapter 4 includes material that has been previously published in [5]. This work was partially funded by a Beckman Young Investigator Award, a Camille & Henry Dreyfus Foundation New Faculty Award, the National Science Foundation through Grant Nos. CHE-1153159 and CHE-1508707, and a UCLA Dissertation Year Fellowship.

Vita

2007-2011	Centennial Scholar Barnard College
2009	ACS-POLYED Award for Excellence in Organic Chemistry Department of Chemistry, Barnard College
2011	B.A. Chemistry Barnard College
2012-2016	Magnetic Resonance TA Molecular Instrumentation Center, UCLA
2013-2014	Associate Alumnae of Barnard College Graduate Studies Fellowship Barnard College
2014	Honorable Mention Graduate Research Fellowship Program National Science Foundation
2014	Ernst Award Magnetic Resonance Division of the German Chemical Society
2014	M.S. Physical Chemistry C.Phil. Physical Chemistry UCLA
2016-2017	Dissertation Year Fellowship Graduate Division, UCLA
2017	Physical Chemistry Award for Outstanding Research Department of Chemistry, UCLA

Publications

N.N. Jarenwattananon and L.-S. Bouchard. “Breakdown of CPMG Spin Echoes in Inhomogeneous Fields.” *in revision.*

K. Youssef, N.N. Jarenwattananon, B. Archer, J.J.Mack, L. Iruela-Arispe, and L.-S. Bouchard. "4-D Flow Control in Porous Scaffolds: Toward a Next Generation of Bioreactors.” *IEEE Trans. Biomed. Eng.* 64, 61-69 (2017).

N.N. Jarenwattananon and L.-S. Bouchard. “Reply to a Comment on Motional Averaging of Nuclear Resonance in a Field Gradient.” *Phys. Rev Lett.* 117, 249702 (2016).

Y.N.Ertas, N.N. Jarenwattananon, and L.-S. Bouchard. “Oxide-Free Gadolinium Nanocrystals with Large Magnetic Moments.” *Chem. Mater.* 27, 5371-5376 (2015).

K. Youssef, N.N. Jarenwattananon, and L.-S. Bouchard. “Feature-Preserving Noise Removal.” *IEEE Trans. Med. Imag.* 34, 1822-1829 (2015).

N.N. Jarenwattananon and L.-S. Bouchard. “Motional Averaging of Nuclear Resonance in a Field Gradient.” *Phys. Rev Lett.* 114, 197601 (2015).

J.W. Brown, N.N. Jarenwattananon, T. Otto, J. L. Wang, S. Glöggler, and L.-S. Bouchard. “Heterogeneous Heck Coupling in Multivariate Metal-Organic Frameworks for Enhanced Activity and Selectivity.” *Catal. Commun.* 65, 105-107 (2015).

N.N. Jarenwattananon, S. Glöggler, T. Otto, A. Melkonian, W. Morris, S.R. Burt, O.M. Yaghi, and L.-S. Bouchard. “Thermal maps of gases in heterogeneous reactions.” *Nature* 502, 537-540 (2013).

CHAPTER 1

Introduction

1.1 Principles of NMR

Nuclear magnetic resonance (NMR) is used in a wide variety of fields such as biology and medicine [8–10], catalysis [11,12], chemistry [13–15], process control [16], and quantum computing [17]. In the field of chemistry, NMR is a tool for structural determination [18], chemical identification [19], materials characterization [20], and molecular dynamics studies [21]. Solid-state NMR and NMR microscopy are important techniques for molecular structure, dynamics, and characterization of crystalline, amorphous, porous, and soft materials [15]. Even the fields of food chemistry and food science [22] often utilize NMR. In the medical community, magnetic resonance imaging (MRI) has become an indispensable diagnostic tool. A comprehensive introduction to NMR and its wide variety of experimental and theoretical techniques could fill a library of books, see for example [2,23–31]. The following introduction is by no means rigorous, and is intended as a brief overview to introduce basic NMR concepts and discuss their potential for application in heterogeneous catalysis [11,32–39].

1.1.1 Classical description of NMR

A complete and accurate description of magnetic resonance requires quantum mechanics; however, in many cases, a classical treatment can sufficiently describe the macroscopic magnetic behavior. Atoms with an odd number of protons and/or odd number of neutrons possess nuclear spin angular momentum, and are capable of demonstrating the magnetic resonance phenomenon. The nuclear magnetic resonance is a physical phenomenon in which nuclear spins in a magnetic field absorb and emit radiofrequency (RF) radiation.

These nuclear spins, frequently referred to simply as “spins,” can be imagined as charged spheres that give rise to a small magnetic moment. In medical applications, proton (^{1}H) is the most commonly studied nucleus. Atoms such as phosphorus (^{31}P) and carbon (^{13}C) are also of interest; however, ^{1}H is by far the most commonly studied nucleus, including in this this dissertation. Henceforth, unless otherwise noted, we will assume the case of ^{1}H (proton) magnetic resonance. The magnetic resonance phenomenon is based on the interaction of the nuclear spin with three types of magnetic fields: 1) the external magnetic field B_0, 2) the radiofrequency field (RF) B_1, and 3) magnetic field gradients g.

1.1.2 Main field B_0

Quantum mechanics dictates that when a nucleus with spin quantum number I is placed in a magnetic field, the spin has $2I + 1$ non-degenerate energy levels. The ^{1}H nucleus is spin $I = 1/2$ and when placed in a magnetic field, has two distinct energy levels α and β. In the classical model, in the absence of an external magnetic field, the nuclear spins are randomly oriented and have zero net macroscopic magnetization. However, in the presence of a magnetic field B_0, nuclear spins align either parallel (low energy) or antiparallel (high energy) to B_0. On the macroscopic scale, the external field polarizes the sample, creating an excess of spins in the lower energy level which induces a net magnetization moment M_0. Another effect of placing the sample in an external field is that the nuclear spins exhibit resonance at the Larmor frequency, ω_L. The Larmor frequency of a particular nucleus is defined as:

$$\omega_L = -\gamma_n \times B_0 \tag{1.1}$$

and depends on both the gyromagnetic ratio of the nuclear spin γ_n and the external magnetic field strength B_0. The gyromagnetic ratio is a unique, known constant for each type of nucleus and is the ratio of a nucleus' magnetic moment to its angular momentum. For ^{1}H, the gyromagnetic ratio is 42.56 MHz/T. The nuclear spins can be excited by the appropriate RF magnetic field tuned to the Larmor frequency, and emit a signal with the same frequency. A classical analogy of nuclear spins is a spinning top, in which the nuclei precess about the field at a given frequency.

Traditionally, the direction of the field is the longitudinal direction, or the z'-direction.

The direction of the magnetic field B_0 defines the x', y' and z' directions. This coordinate system is known as the laboratory frame, and has x' and y' axes fixed in space.

1.1.3 Radiofrequency field B_1

In the presence of an external magnetic field B_0, the equilibrium state of magnetization is given as M_0. To obtain a magnetic resonance signal, we apply a radiofrequency (RF) magnetic pulse B_1 in the transverse (xy) plane. A B_1 pulse is a linearly oscillating magnetic field, with a transmitter frequency ω_{rf}. This frequency is very close to the Larmor frequency of the nuclear spins. This RF pulse applies a torque, which rotates the magnetization vector $\mathbf{M}$ away from the z'-axis. Once this motion starts, the bulk magnetization $\mathbf{M}$ begins to precess around the z'-axis at the Larmor frequency.

These motions have a complicated time dependence, and are more easily described in the rotating frame. If we consider the linearly oscillating RF field as the sum of two counter-rotating fields with angular frequencies $+\omega_{rf}$ and $-\omega_{rf}$, only the component that rotates in the same direction as the Larmor frequency is retained. The other field, $-\omega_{rf}$, can be imagined as hundreds of MHz off-resonance and has negligible effect on the spins. Now we can view the NMR experiment in the rotating frame, which rotates around the z'-axis with an angular frequency of ω_{rf}. In this frame, the radiofrequency field appears static, and pulses can be imagined as a static magnetic field B_1 orthogonal to the external field B_0. The rotating frame axes are labeled as x, y, and z, with the z-axis corresponding to the z'-axis of the laboratory frame.

In the rotating frame, the RF pulse causes the bulk magnetization to precess about the static field B_1 until it is turned off. A pulse about the $+x$-axis rotates $\mathbf{M}$ toward the $-y$-axis with an angular frequency of $\omega_1 = -\gamma_n B_1$. The flip angle β through which $\mathbf{M}$ rotates is given as $\beta = \omega_1 t_p$ where t_p is the pulse length. Typical flip angles are 90° to achieve a maximum excitation of transverse (xy) magnetization and 180° to invert the equilibrium magnetization.

In many experiments, including those in this dissertation, only pulses about the $x, y, -x$, and $-y$ axes are used, which is achieved by altering the phase of the RF field in the laboratory frame.

1.1.4 Magnetic field gradients g

In magnetic resonance imaging, spatial encoding is achieved by application of a magnetic field gradient g. For example, application of a gradient g_z in the $z-$direction creates an applied field of $B_0 + g_z z$. Regardless of directionality in the magnetic field gradient (x, y, or z), application of the magnetic field gradient leaves the combined magnetic field still pointing in the z-direction; however, in our example, the strength of the field varies as a function of the z-location, i.e., $g_z = dB_z/dz$. The precession frequency of the nuclear spins becomes a function of their spatial $z-$location. The Fourier transform of the free induction decay (FID) signal demonstrates the contribution from the differing frequency components, which can be mapped onto a particular z-location. The use of magnetic field gradients to create an inhomogeneous magnetic field is vital in magnetic resonance imaging, as well as the temperature mapping method we have developed in this dissertation.

1.1.5 Free precession and Fourier transform NMR

Given an NMR spectrum with a single resonant peak, e.g., the ^{1}H spectrum of water, the transmitter frequency ω_{rf} can be set exactly to match the Larmor frequency. A 90°_x pulse rotates the bulk magnetization into the $-y$-axis. If the resonance offset $\Omega = \omega_0 - \omega_{rf} = 0$, the bulk magnetization does not begin to precess around the $z-$axis, because the transformation from laboratory frame to rotating frame has removed the static field B_0. If, however, there is a resonance offset Ω, then there is a residual field ΔB_0 along the z-axis of the rotating frame. This residual field is given as $\Delta B_0 = \Omega/\gamma_n$. In this case, $\mathbf{M}$ will start to precess at the rate Ω about the z-axis as soon as the pulse is switched off.

As described above, a pulse generates magnetization in the xy plane. This magnetization, called the free induction decay (FID), is a sum of oscillating waves of different frequencies, amplitudes, and phases. In modern spectrometers, the FID is detected by two orthogonal detection channels, x and y. This type of detection is called "quadrature detection." For each resonance in a spectrum, two signals, cosine and sine functions of the offset frequency Ω, are acquired in the x and y channels respectively. Sometimes the two functions are referred to as the "real" and "imaginary" parts of a complex time domain signal $S(t)$:

$$\begin{aligned} S(t) &= [\cos\Omega t + i\sin\Omega t]\exp(-t/T_2) & & \\ &= \exp(i\Omega t)\exp(-t/T_2) & t &\geq 0 \\ &= 0 & t &< 0 \end{aligned} \tag{1.2}$$

As a function of time, the FID $S(t)$ can be converted to a frequency-domain function of the spectrum $S(\omega)$ by Fourier transformation:

$$S(\omega) = \int_{-\infty}^{\infty} S(t)\exp(i\omega t)dt. \tag{1.3}$$

This yields,

$$S(\omega) = A(\Delta\omega) - iD(\Delta\omega), \tag{1.4}$$

where

$$A(\Delta\omega) = \frac{1/T_2}{(1/T_2)^2 + (\Delta\omega)^2} \qquad \text{and} \qquad D(\Delta\omega) = \frac{\Delta\omega}{(1/T_2)^2 + (\Delta\omega)^2}. \tag{1.5}$$

The frequency offset, $\Delta\omega = \omega - \Omega$, is the offset measured from the center of the resonance Ω. $A(\Delta\omega)$ is the real part of the spectrum, an absorptive Lorentzian curve. This Lorentzian is centered on the frequency Ω and has a full-width at half max (FWHM) of $1/\pi T_2$. The corresponding imaginary part of the spectrum $D(\Delta\omega)$ is a dispersive Lorentzian.

In reality, the NMR spectrum rarely turns out with a pure absorptive and pure desorptive component in the lineshape. In order to obtain an absorption lineshape in the real part of the spectrum, we take linear combinations of the real and imaginary parts of the spectrum until we "phase" the spectrum. In imaging, we frequently utilize the spectrum in magnitude mode to circumvent phasing.

1.1.6 Relaxation times

The magnetization $\mathbf{M}$ produced by RF excitation does not remain in the transverse plane indefinitely. The population of energy levels α and β are equal only immediately after a 90° pulse. After a certain time period, the population distribution returns to thermal equilibrium in a process called "spin-lattice" or longitudinal relaxation. The relaxation time characterizing the return to the longitudinal-axis is called the spin-lattice, or T_1 relaxation time. The build-up of magnetization in the longitudinal-axis is:

$$M_z(t) = M_{z,eq}(0)[1 - \exp(-t/T_1)]. \tag{1.6}$$

The spin-lattice relaxation process redistributes the nuclear spin states to a Boltzmann distribution. Typically, the relaxation rates depend strongly on the NMR frequency and the magnetic field strength. In the hydrocarbon gases and liquids studied in this dissertation, T_1 values range from hundreds of milliseconds to over 20 seconds.

A second time constant characterizes the decay of the vector component in the xy-plane. In this case, the magnetization in the transverse plan returns back to an equilibrium value of zero. This second process is called spin-spin relaxation time and is characterized by the T_2 time constant. The initial xy magnetization decays to zero as:

$$M_{xy}(t) = M_{xy}(0)\exp(-t/T_2) \tag{1.7}$$

The transverse magnetization decays because the precessing nuclear spins lose phase coherence over time. Due to random fluctuations of the local magnetic field, the different spins experience random variations in the instantaneous precession frequency. T_2 values for the hydrocarbons studied in this dissertation range from hundreds of microseconds to hundreds of milliseconds for gases and milliseconds to seconds for liquids.

1.1.7 Bloch equations

The Bloch equation phenomenologically describes the magnetization vector $\mathbf{M}$ as:

$$\frac{d\mathbf{M}}{dt} = \mathbf{M} \times \gamma_n B - \frac{M_x\mathbf{i} + M_y\mathbf{j}}{T_2} - \frac{(M_z - M_0)\mathbf{k}}{T_1}, \tag{1.8}$$

in which $\mathbf{i}, \mathbf{j}$, and $\mathbf{k}$ are unit vectors in the x, y and z directions respectively; M_0 is the equilibrium magnetization generated by the main field B_0; and $\mathbf{B}$ includes the magnetic fields B_0, B_1 and any applied gradient g.

1.1.8 Chemical shift

The NMR frequency, or Larmor frequency, of a nucleus in a molecule is determined by the gyromagnetic ratio and the external field strength (Eq. 1.1). At a field strength of 9.4 T, protons resonate at 400 MHz. However, not all protons have identical resonance frequencies; the NMR frequency also depends on the local electron distribution, i.e., the position of the nucleus in a molecule and its surrounding environment. This effect is known as the chemical shift effect, and makes NMR a unique and attractive methodology in chemistry and biology. For example, the three chemically distinct protons in ethanol can be distinguished from one another, and biological chemists can resolve distinct signals for hundreds of protons in a protein.

1.1.9 Spin echoes

The decay of the free induction decay signal arises from interactions that cause the spins to precess at different frequencies, which destroys the phase coherence. There are two main causes of this decoherence: 1) the spin-spin relaxation process, which is induced by intramolecular and intermolecular magnetic fields and 2) spatial inhomogeneity of the static field B_0. A technique that can distinguish the two processes is the spin echo experiment [40–42]. In the basic spin echo experiment, a 90°_x pulse aligns the $\mathbf{M}$ magnetization into the $-y$-axis. The magnetization precesses freely and dephases for a time τ before a refocusing RF pulse flips $\mathbf{M}$ by 180°. Free precession for time τ causes the magnetization to realign along the $-y$ axis. The spin echo (and its modification, the stimulated echo [1,43,44]) experiment can be used to measure T_2 relaxation and diffusion processes, and is frequently used as a backbone for magnetic resonance imaging experiments.

1.2 *Operando* Measurements of Chemical Reactions

The study of chemically-reacting flows is of paramount interest to the fields of biology, physics, engineering, and chemistry. These systems and the physical phenomena underlying them are well-described by the theory of nonequilibrium thermodynamics [45]. Examples include: combustion processes [46], charge transport in ion exchange membranes [47], reactions on catalytic surfaces [48], chemical kinetics in laminar flow reactors [49], and optimization of catalytic reactors [50].

1.2.1 Heterogeneous catalysis

Catalysis is a fundamental component of many industrial processes, and considerable resources are spent optimizing these reactions. Over 85% of all chemical industry products are made using catalysts, the overwhelming majority of which are heterogeneous catalysts that function at the gas-solid interface [51–54]. However, probing the behavior of a gas inside a reactor is challenging because tools that do not disturb the chemically-reacting flow are required. In addition to being non-invasive, such tools must be able to measure the physical parameters and gradients that dictate heat flow, mass flow, and catalytic efficiency [33,35,55–58]. The complexity of these systems demands many approximations, which can only be tested with experimental observations of quantities such as temperature, pressure, concentrations, flow rates, etc [56,57]. A non-invasive experimental technique is needed to measure the catalytic, chemical, and physical gradients inside heterogeneous reactions.

1.2.2 Microreaction technology

Microreactors, defined as reactors on the millimeter scale or smaller, have increasingly gained importance in both laboratory and industrial applications [59–63]. Compared to conventional reactor systems, microreactors offer several advantages: reduction of waste catalyst, improved heat and mass transport due to increased specific surface area, as well as increased efficiency, safety and ease of process control [64, 65]. Chemically-reacting flows in microreactors have demonstrated highly efficient reactions when combined with immobilized solid catalysts [65, 66]. The increased safety is primarily attributed to fine control over reactant delivery, small reaction volume, and small-scale production of hazardous products and intermediates [64], which can allow for operation at conditions too dangerous for a conventional industrial set-up. However, when a catalyst is packed inside a millimeter-scale (or smaller) volume, spatial heterogeneities due to the catalyst packing and grain size occur.

Detailed insight into the spatiotemporal gradients in heterogeneous catalysis is important for rational design of new and more sustainable processes [67]. There is considerable interest in the working principles of catalysis, for example monitoring reaction progress in a microreactor, examining reaction kinetics in the presence of transport, evaluating catalyst performance over time, identifying phase transitions, and development of structure-to-performance relationships [68, 69]. Despite this interest, it is difficult to characterize and optimize heterogeneous reactors, especially microreactors and other laboratory-scale reactors due to lack of adequate tomographic methods. Our knowledge is still primarily based on input/output relationships and point measurements [67, 70–73], both of which take average measurements across an inhomogeneous system without consideration of spatial gradients.

Several experimental techniques have been utilized to extract information about the various catalytic gradients inside the reactor with varying degrees of efficiency [74–77]. Optical techniques [78–82] are both limited in opaque media and also are primarily point measurements. Even with a transparent reactor, the solid catalyst is often opaque. Sensor-based approaches [83,84] can be utilized to make point measurements of temperature, pressure, and chemical sensing inside the reactor, but lead to flow perturbations. X-ray based microscopy and spectroscopy can provide excellent time and spatial resolution [85–87] but require synchrotron light sources. Mass spectrometry is also an extremely sensitive technique, but has thus far been limited to point measurements [88–90] of conversion and comparing these point measurements to simulations. However, despite these important efforts, none of these techniques is capable of providing high resolution 3D maps of the flow, chemical species, temperature or pressure in a packed-bed reactor.

On the other hand, magnetic resonance imaging provides a means to overcome these issues due to its non-invasive nature and ability to “see” inside a microreactor. With magnetic resonance, information can be extracted from a chemically-reacting flow at the local level inside an operating reactor and used to study reactions and optimize reactors [32, 33, 91, 92].

1.2.3 NMR imaging of heterogeneous reactions

NMR spectroscopy and imaging have been applied to the study of catalysis [12] in operating reactions [35, 93]. Thus far, NMR has been applied to catalyst studies [94–97]; temperature [5, 98]; diffusion, velocity, flow, and transport phenomena [99–104]; conversion and spatial distribution of chemical species [34, 105–110].

The objective of this dissertation is to develop magnetic resonance imaging methods to extract thermodynamic parameters from catalytic reactions *in situ*, specifically, temperature of gases in operating reactions. Traditional NMR thermometry, a non-invasive technique, is based on the temperature dependence of the chemical shift [111, 112], spin-lattice and spin-spin relaxation times, diffusion in a pulsed-field gradient (PFG) [2], intermolecular multiple-quantum coherences (iMQC) [113], or contrast agents [114]. However, these established methods are not practical for gas phase reactions for several reasons: resonance frequency shift and relaxation times exhibit weak dependence on temperature, signals from PFG and iMQC experiments are rapidly attenuated by diffusion, and contrast agents constitute an additive that may interfere with reactions. My research has sought to develop a thermometry method as accurate as traditional NMR thermometry techniques. This technique provides a non-invasive tool to locate hot and cold spots in heterogeneous reactors, offering unique capabilities for testing the approximations used in reactor modeling. The method is robust relative to factors such as pressure, gas mixture composition, reactor type, catalyst type, reaction rate, and steady state conversion. Our technique outperforms other existing thermometry techniques, does not require added contrast agents, is non-invasive, and can provide detailed views of spatial variations in temperature. The motional-averaging NMR method reported here opens the door to studies of *in situ* thermodynamics and optimization of gas-phase reactors.

In chapter 2 of this dissertation, we investigated the motional averaging behavior of gases inside a magnetic field gradient. The motional averaging behavior of gases in an inhomogeneous field is fundamentally different from that of liquids and the difference is observed in the NMR linewidth. In gases, the NMR linewidth decreases as a function of temperature, which opposes the conventional NMR theory. We developed a more detailed theoretical framework, which accounts for memory losses and position autocorrelation effects. The effect of temperature and applied gradient strength on the NMR linewidth were studied. This more detailed description of the NMR dephasing function also predicts a t^1 time dependence in gases. In chapter 3 of this dissertation, we explicitly demonstrated the difference in signal decay due to motional averaging differences in liquids and gases. The Carr-Purcell Meiboom-Gill (CPMG) experiment, which is used in liquids to mitigate diffusion effects in inhomogeneous fields, failed to eliminate inhomogeneous broadening in gas NMR. In chapter 4 of this dissertation, we exploit the motional averaging behavior of gases in a field gradient to develop a NMR thermometry method. We used this method to image gas temperatures inside an operating chemical reactor, a first in the field. Finally, in chapter 5 we discuss implications of this work in the broader scientific community.

Magnetic resonance imaging is still a novel modality for studying chemical reactions *in situ*. Expanding the NMR toolkit for extracting thermodynamic parameters from heterogeneous reactions is key for useful, real-time reaction optimization. The motional averaging behavior studied and exploited in this dissertation is only one such tool in the toolkit. If we can continue to expand the way non-equilibrium thermodynamics is currently used, we can extract new, microscopic level views of the local thermodynamics inside a microreactor. This will have a positive impact on chemistry and, in particular, heterogeneous catalysis and chemical engineering research.

CHAPTER 2

Motional Averaging of Nuclear Resonance in a Field Gradient

For over six decades, diffusion-weighted nuclear magnetic resonance (NMR) has been the flagship experiment for measurements of molecular self-diffusion in free or confined geometries. Diffusion-based NMR experiments have a wide range of applications from porous media [115], catalysis [32], materials science and chemistry [20] to biomedicine [116]. Consider the simple experiment shown in Fig. 2.1, where the nuclear induction signal is read out in the presence of a magnetic-field gradient. The gradient modulates the magnetization spatially along the gradient's direction (assuming a sufficiently strong external field so that the gradient is unidirectional). Time evolution of this magnetization in the presence of diffusion effects provides a direct and unambiguous measurement of the self-diffusion process. In the traditional description of molecular self-diffusion [40, 41, 117–119], a molecule undergoes a random walk whereby at each time step, the nuclear spins accumulate phase increments that are randomly drawn from a normal distribution. In the presence of a magnetic-field gradient, the decoherence of the nuclear induction signal $S(t)$ follows the well-known textbook expression [2, 40, 41, 117–119]:

$$S(t) = \exp\left(-(1/3)\gamma_n^2 g^2 D t^3\right), \tag{2.1}$$

where γ_n is the nuclear gyromagnetic ratio, D is the self-diffusion coefficient, g is the applied gradient strength, and t is time. The t^3 dependence has been extensively validated and has been utilized to measure molecular self-diffusion coefficients in a wide variety of liquids [1–3]. In a gas, however, the situation is more complicated. The assumption of a normally-distributed phase accumulation at every time step is difficult to justify in light of the fact that gas molecules undergo much more rapid motion than in liquids, due to much longer free displacements between collisions. The farther the molecular displacements along the direction of the gradient, the faster the nuclear spins will lose memory of their immediate environment. This memory loss should be expected to enter the description of the decoherence process. Surprisingly, this simple aspect of free diffusion is still lacking a thorough experimental verification.

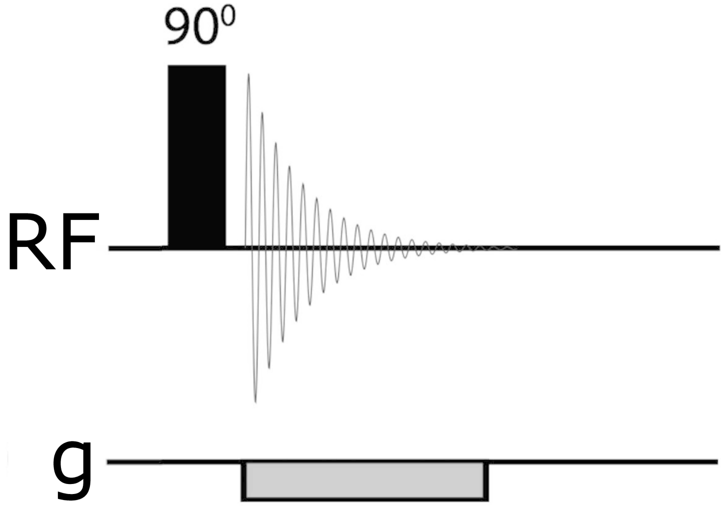

Figure 2.1: Measurement of molecular self-diffusion in a constant field gradient. A 90° radiofrequency (rf) pulse tips the magnetization. This resulting nuclear induction signal is measured in a constant gradient of amplitude g. The time evolution of magnetization, as described by the textbook [1–3] expression (Eq. 2.1), interrogates the molecular self-diffusion process.

The NMR signal, $S(t)$, from an ensemble of spins initially located at $x(0)$ is given by the expectation value of the phase factor:

$$S(t) = \left\langle \exp\left(i \int_0^t \omega(t')dt' \right) \right\rangle , \tag{2.2}$$

where $\omega(t)$ describes the time-dependent resonance frequency offset (in the rotating frame). In the presence of a magnetic field gradient g, the resonance frequency is $\omega(t) = \gamma_n g x(t)$, where $x(t)$, the position of the nuclear spin after time t, is a random process. If we assume a Gaussian random process that is stationary in the wide sense, this expectation value takes the form [119]:

$$\exp\left(i\gamma_n g \int_0^t \langle x(t')\rangle dt' - \gamma_n^2 g^2 \int_0^t \langle x(t')x(0)\rangle (t-t')dt'\right). \tag{2.3}$$

The first term, $\exp(i\gamma_n g \int_0^t \langle x(t')\rangle dt')$, encodes the position in the phase of the spins [120] after undergoing displacement but does not lead to decoherence unless the diffusion is not free. The second term describes signal decay, and consequently, affects linewidth. More complicated random processes may lead to higher-order terms, but we shall limit our discussion to the case where $x(t)$ is a wide-sense stationary Gaussian random process.

Over the timescale t of the NMR measurement, liquid phase molecules experience displacements that are much smaller than those in the gas phase. We may write this as $x(t) \approx x(0)$, for a liquid. This approximation, known as the Einstein-Fick limit, indicates that the position autocorrelation function can be approximated by the mean-square displacement:

$$\langle x(t)x(0)\rangle \approx \langle x(t)x(t)\rangle = 2Dt, \tag{2.4}$$

where D is the self-diffusion coefficient. It is known from experiments that in liquids, this limit holds [1–3]. However, D_{liquid} and D_{gas} differ by three orders of magnitude, and it is unclear if this approximation also holds for gases. Away from the Einstein-Fick limit, contributions from ballistic transport become significant. We note that substitution of the limit Eq. 2.4 into the second term of Eq. 2.3 recovers the result Eq. 2.1 as a special case.

In this chapter, we show that Eq. 2.1 does not hold for gases based on the analysis of linewidth as function of temperature T. Because $D(T)$ increases with T, Eq. 2.1 predicts that linewidth should increase with T. We find that gases instead undergo line narrowing with temperature. It is unclear by cursory inspection of Eq. 2.1 how gases may differ from liquids, especially in light of the fact that the dependence of line broadening on diffusion coefficient has been verified experimentally in several studies (see, for example, [1,121,122]). The key to establishing this distinction is a closer look at the temperature dependence of the line broadening mechanism, as explained below.

In the NMR experiment, nuclear spins are well isolated from the lattice and do not depolarize or randomize their phases when undergoing molecular collisions, in contrast to collisional broadening mechanisms in optics. Thus, the description of line broadening in such a "weak collision" regime reflects the histories of molecular displacements. The simplest way to account for this is through a position autocorrelation function. Suppose that the particle displacements are modeled using a generalized Langevin equation (GLE) with memory kernel:

$$M\dot{v} + \int_0^t \Gamma(t-t')v(t')dt' = \eta_f(t), \tag{2.5}$$

where M is the mass of the diffusing particle, $\Gamma(t)$ is a memory kernel, $v(t) = \dot{x}(t)$ is the particle velocity, $\dot{v}$ is its acceleration, and $\eta_f(t)$ is a stochastic force. The GLE has been validated experimentally for Brownian particles ($M \gg m$, where m is the mass of fluid particles); for example, in the studies [123–126] M was 10^{10} times larger than m. So while the GLE was not designed to model self-diffusion processes, it can be invoked to model viscous drag effects via the memory kernel. In what follows, we shall set $M = 10^{10} \cdot m$, which is the only regime we are aware of, where the GLE has been validated experimentally based on direct measurements of individual histories (namely, in Refs. [123–126]).

By the fluctuation-dissipation theorem, the stochastic force $\eta_f(t)$ describes colored noise, $\langle \eta_f(0)\eta_f(t)\rangle = kT\Gamma(t)$, where k is Boltzmann's constant. The time-correlation function $\langle x(t)x(0)\rangle$ is obtained from $\langle v(t)v(0)\rangle$ by integrating twice the velocity autocorrelation function

$$\langle v(t)v(0)\rangle = -\frac{d^2}{dt^2}\langle x(t)x(0)\rangle. \tag{2.6}$$

Projecting equation (2.5) with the operator $\langle v(0), \cdot\rangle$ yields the deterministic equation:

$$M\langle v(0)\dot{v}(t)\rangle + \int_0^t \Gamma(t-t')\langle v(0)v(t')\rangle dt' = 0. \tag{2.7}$$

Integrating this velocity autocorrelation function once

$$\nu(t) = \int_0^t \langle v(0)v(t')\rangle dt', \tag{2.8}$$

and using the equipartition theorem, $\langle v(0)v(0)\rangle = kT/M$, as the initial condition, we get:

$$M\dot{\nu}(t) + \int_0^t \Gamma(t-t')\nu(t')dt' = kT. \tag{2.9}$$

For the memory kernel to describe the delayed response of the surrounding fluid, we choose the Ornstein-Uhlenbeck process:

$$\Gamma(t) = (\gamma^2/m)\exp(-\gamma t/m),$$

where γ is the friction coefficient which is proportional to the viscosity of the medium and m is the mass of molecules in the surrounding medium causing friction. Denoting $\zeta_{-,+} = (\gamma/2m)(1 \mp \sqrt{1 - 4m/M})$, we obtain the solution to equation 2.9:

$$\nu(t) = \frac{kT}{M}\Big\{\frac{\gamma}{m\zeta_-\zeta_+} + \frac{1}{\zeta_+ - \zeta_-}\Big[\Big(1 - \frac{\gamma}{m\zeta_+}\Big)e^{-\zeta_+ t} - \Big(1 - \frac{\gamma}{m\zeta_-}\Big)e^{-\zeta_- t}\Big]\Big\}. \tag{2.10}$$

From this we get the position autocorrelation function,

$$\langle x(t)x(0)\rangle = \frac{kT}{M(\zeta_+ - \zeta_-)}\Big[\zeta_+^{-1}\Big(1 - \frac{\gamma}{m\zeta_+}\Big)e^{-\zeta_+ t} - \zeta_-^{-1}\Big(1 - \frac{\gamma}{m\zeta_-}\Big)e^{-\zeta_- t}\Big]. \tag{2.11}$$

This result was also derived by Nørrelykke [127] using a different method. In the Einstein-Fick approximation, $x(0) \approx x(t)$, and this position autocorrelation function reduces to $2Dt$. Equation 2.11 generalizes $S(t)$ outside the Einstein-Fick limit. There are three distinct regimes: overdamped ($M > 4m$), critically damped ($4m = M$), and underdamped ($M < 4m$). Standard Brownian motion of large particles is strongly overdamped ($M \gg m$). The Einstein-Fick limit occurs when the ratio $\gamma t/m$ is sufficiently large to cause appreciable decay of the Ornstein-Uhlenbeck kernel. Using γ based on the Stokes' law and $t = 40$ μs as the sampling time of the nuclear induction signal, we find that typical values of this ratio for liquids are $\gamma t/m \sim 1$ whereas for gases we have $\gamma t/m \ll 1$.

In the case of a gas, we may obtain the overall temperature by modeling γ using the Stokes' law, $\gamma = 3\pi\eta_v d$ (η_v, shear viscosity of the medium; d, sphere diameter), which holds in the limit of low Reynolds numbers and invoking the Sutherland's formula [128] for η_v:

$$\eta_v = \frac{\mu_0(T_0 + C)(T/T_0)^{3/2}}{T + C} \sim \frac{T^{3/2}}{T + C}, \tag{2.12}$$

where C is Sutherland's constant for the gas, μ_0 is the viscosity at temperature T_0. At low temperatures, $\eta_v \sim T^{3/2}$, whereas at high temperatures, $\eta_v \sim \sqrt{T}$. By substituting this into Eq. 2.12, we obtain at an expression for the envelope function of the signal decay for a gas which does not rely on the Einstein-Fick limit:

$$S(t) = \exp\left(-\gamma_n^2 g^2 \kappa t\right) \tag{2.13}$$

with

$$\kappa(T) = \frac{kT(-m\zeta_-^2\zeta_+ - m\zeta_-\zeta_+^2 + \zeta_-^2\gamma + \zeta_-\zeta_+\gamma + \zeta_+^2\gamma)}{mM\zeta_-^3\zeta_+^3}, \tag{2.14}$$

The linewidth Δf follows the power law:

$$\Delta f \sim \begin{cases} T^{-7/2}, & T < C \\ T^{-1/2}, & T > C \end{cases}, \tag{2.15}$$

which predicts a temperature dependence that is opposite (i.e., line narrowing with increasing temperature) to that based on self-diffusion in the Einstein-Fick limit (Eq. 2.1). An analogous expression in the case of liquids can be derived using a suitable model for the temperature dependence of the viscosity in a liquid. However, this will not be needed here, because we shall see that the linewidth is essentially independent of temperature.

2.1 Experimental Results and Discussion

Measurements of Δf were carried out as a function of T for three gases in the high temperature regime ($T > C$, as determined by the Sutherland's constant for each gas [112,129,130]). The results are shown in Figure 2.2. The average exponent was found to be -0.47 ± 0.04, in agreement with the theoretically predicted value of $-1/2$ in Eq. 2.15. The low temperature regime ($T < C$) could not be investigated due to experimental limitations of our instrument. A temperature dependence of linewidth could not be detected within experimental error for liquids, as shown in Figure 2.3, where we investigated nine different liquids over the range 180-450 K. We note that the Sutherland's formula (and therefore, Equation 2.13) is applicable to gases only, so a lower limit on temperature for the liquids is imposed by the freezing points.

We now turn out attention to the gradient dependence of the line broadening, which, according to Eq. 2.13, should be proportional to g^2. In experiments, however, we found two regimes: in the limit of weak gradients, $\Delta f \propto g^2$, whereas for strong gradients, $\Delta f \propto g^1$ (see

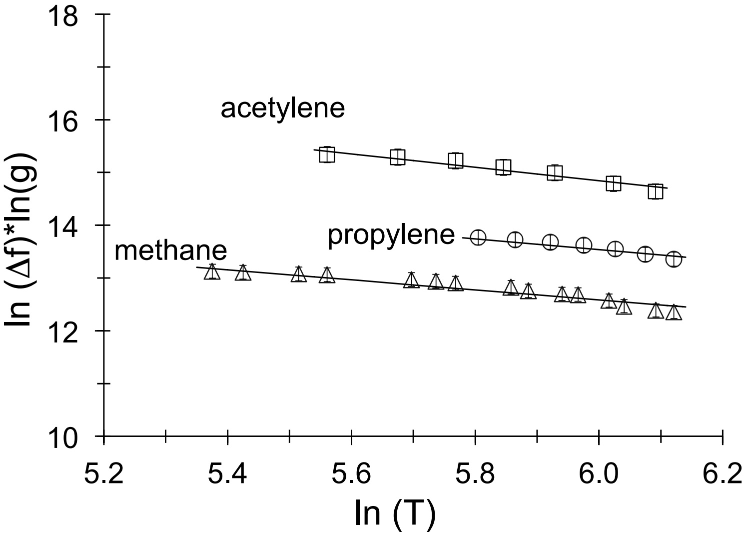

Figure 2.2: Validation of the $T^{-1/2}$ law in the high-temperature regime ($T > C$) for gases. The values of $\ln T$ shown correspond to the temperature range $T = 180 - 490$ K. Three different gases were investigated: methane, acetylene, and propylene. The temperature dependence on linewidth (scaled to gradient strength) was found to be $\Delta f \propto T^{-0.47\pm0.04}$ (averaged over the three gases). Although different values of the applied gradient g are shown here to avoid overlapping of the curves (methane, g=0.15 G/cm; acetylene, g=0.07 G/cm; propylene, g=0.1 G/cm), the scaled linewidth is independent of g.

Figs. 2.4 and 2.5). The g^2 gradient dependence is predicted according to Eq. 2.13; however, the $\Delta f \propto g^1$ is not. Moreover, these two regimes apply to both liquids and gases, according to the results of Figs. 2.4 and 2.5. The emergence of the g^1 regime is likely due to the convolution of the line shape with the sample shape that arises under an applied gradient and forms the basis for frequency encoding in magnetic resonance imaging. The full signal equation integrated over the sample shape is:

$$S(t) = \int \exp(i\gamma_n gxt)\exp(-\alpha g^2 t)\rho(x)dx, \tag{2.16}$$

where $\rho(x)$ describes the spin density profile along the x direction (sample shape), $\exp(i\gamma_n gxt)$ is the frequency encoding and $\exp(-\alpha g^2 t)$ is the line broadening according to Eq. 2.13. For the particular case where the sample shape $\rho(x)$ is Gaussian (a reasonable approximation for the sensitivity profile of a saddle coil, such as the one used in these experiments), the

Fourier transform of Eq. 2.16 with respect to time is a convolution:

$$\tilde{S}(\omega) = \text{Gauss} \otimes \text{Lorentz} = \text{Voigt}, \tag{2.17}$$

in which the Gaussian is $\sim \exp(-x^2/2\sigma^2)$, and the Lorentzian is $\sim \Gamma^2/(x^2+\Gamma^2)$. In terms of the full width at half maximum of the Gaussian ($f_G = 2\sigma\gamma g\sqrt{2\ln 2}$) and Lorentzian ($f_L = 2\Gamma = 2\alpha g^2$) profiles, the width of the Voigt profile can be expressed as $f_v \approx 0.5 f_L + \sqrt{0.2 f_L^2 + f_G^2}$. Thus, in the frequency encoding regime, where sample shape effects dominate, the line broadening behaves as g^1 regardless of whether Eq. 2.1 or Eq. 2.13 are used to describe diffusion effects. The frequency encoding regime is reached when the field of view FOV=$f_s/\gamma_n g$ (f_s, sampling rate; g, gradient amplitude), becomes comparable to the size of the rf-sensitive region ($\sim$ 1 cm in our experiments). Depending on the applied gradient strength, the experimental FOV ranges from 0.6 to 1460 cm. The FOV values corresponding to applied gradient (g) are indicated in the upper horizontal axes of Figs. 2.4 and 2.5, where the two regimes, g^1 and g^2, are indicated.

We have presented a revised expression for line broadening (Eq. 2.13) that not only takes into account the autocorrelation effects in the diffusion process, but also suggests that self-diffusion processes in the NMR experiment may be described using a stochastic GLE; at least, as far as its temperature dependence is concerned. The GLE (Eq. 2.13) enables a convenient description of the memory effects arising from the viscous drag effects, which were essentially missing from the traditional description (Eq. 2.1). Such drag effects yielded the correct temperature dependence for gases and have been used in a recent publication to non-invasively map temperatures of gases during catalytic reactions [5]. The method could also be useful in the validation of heat-transfer models for gas-phase thermal exchange systems, which currently rely on numerical results from computational fluid dynamics models. Finally, we note that since the decay function (Eq. 2.13) involves the first power of time instead of its third power (Eq. 2.1), Eq. (2.13) could have implications for the design of dynamic decoupling schemes for coherent quantum control [131].

2.2 Supplementary Data Analysis and Sample Data

2.2.1 Linewidth vs. temperature data

For gases, linewidth vs. temperature data for each gas was fit to a linear regression. Only the high-temperature regime (i.e. above the Sutherland's constant C) could be studied due to limitations in the VT control. In Ref. [128] the Sutherland's constant was calculated for each gas according to its viscosity [128, 129] and Sutherland's model [128, 130]:

$$\mu = \mu' \left(\frac{T}{T'}\right)^{3/2} \left(\frac{T'+C}{T+C}\right), \tag{2.18}$$

in which μ is the viscosity of a gas at temperature T, μ' is the viscosity of that same gas at another temperature T', and C is the Sutherland's constant for that gas. The values of S were calculated to be 198 K, 237 K, and 292 K for methane, acetylene, and propylene respectively. For liquids, the lower bound of temperature was determined by the freezing point of the substance; all data above this temperature was fit to a linear regression.

Figure 2.6 (A) is the raw data from a methane linewidth vs. temperature experiment. The gradient strength is $g = 0.15$ G/cm, yielding a FOV of 78 cm. Figure 2.6(B) is the raw data from a dichloromethane linewidth vs. temperature experiment. The applied gradient strength was $g = 0.3$ G/cm, yielding a FOV of 94 cm. Linewidth for the gas-phase data follows a monotonic decrease as a function of temperature, whereas linewidth for liquid-phase data does not follow a clear trend.

2.2.2 Linewidth vs. gradient data

For linewidth vs. gradient data, the two regimes were determined based on the field of view (FOV), as calculated according to the following equation: FOV= $f_s/\gamma_n g$ (f_s, sampling rate; g, gradient amplitude). When the FOV becomes comparable to the size of the rf-sensitive region ($\sim$ 1 cm in our experiments), we are in the frequency-encoding (g^1) regime; when FOV $\gg$ 1 cm, we are in the non-frequency encoding, g^2 regime. The coefficient of the g^1 and g^2 slopes were determined by fitting data in the frequency-encoding regime and non-frequency encoding regimes respectively to a weighted quadratic function.

Figure 2.7(A) is the raw data from a methane linewidth vs. gradient experiment. The data was acquired at T = 220 K. Figure 2.7(B) is the raw data from a dichloromethane linewidth vs. gradient experiment. The data was acquired at T = 300 K. Although the quadratic curves are drawn as a guide to the eye, the data illustrate that linewidth monotonically increases as a function of gradient strength.

2.2.3 Determination of error bars

At each temperature point, five scans were separately acquired and averaged to reduce the effects of temperature fluctuations over the time course of the experiment. For each substance studied, multiple experiments were performed on different days to eliminate the random fluctuations in field homogeneity day to day resulting from magnetic field drift.

2.3 Experimental Methods

2.3.1 Sample preparation

Methane gas ($>$ 99% purity) was purchased from Airgas, Inc. and used as provided. Acetylene($>$ 98% purity) and propylene gases ($>$ 95% purity) were purchased from Praxair, Inc. and used as provided. For the gas-phase experiments, a sealable J. Young NMR tube was evacuated to remove excess air, and filled with pure gas to 15 PSIA. Liquids were purchased from Sigma-Aldrich. For liquid-phase experiments, samples were degassed and flame-sealed in NMR tubes.

2.3.2 NMR methods

Measurements were performed on a 14.1 T vertical bore Bruker AV 600 MHz NMR spectrometer equipped with a 5 mm broadband probe with a z-direction gradient. The sample was placed in the center of the NMR magnet, and the pulse sequence (Fig. 2.1) was applied. The receiver was placed in DQD mode (forward Fourier transform, quadrature detection of complex data). During acquisition, a linewidth-broadening magnetic field gradient of amplitude g was applied.

2.3.3 Temperature control

Temperature is altered by the variable temperature (VT) unit, which controls the temperature of the sample by heating or cooling the surrounding air. Temperatures above ambient temperatures (298 K $<$ T $<$ 460 K) are achieved by the probe's internal heater. Temperatures below ambient temperatures (200K $<$T $<$ 298 K) are achieved with a heat-exchange coil, by pre-cooling the gas in a liquid nitrogen bath. Due to experimental limitations in the VT-system, we were unable to achieve temperatures lower than 200 K or above 460 K. In order to determine the real sample temperature, each VT-temperature value was calibrated against a neat methanol standard for temperatures 200 K $<$ T $<$ 300 K (Eq. 2.19) and a neat ethylene glycol standard for temperatures 301 K $<$ T $<$ 460 K (Eq. 2.20):

$$T[K] = 409.0 - 36.54(\Delta d) - 21.85(\Delta d)^2 \tag{2.19}$$

and

$$T[K] = 466.5 - 102.00(\Delta d), \tag{2.20}$$

in which (Δd) is the chemical shift difference between the two peaks of neat methanol or two peaks of neat ethylene glycol [112]. We note that at colder temperatures ($<$ 290K), temperatures tended to fluctuate more than at ambient and above ambient conditions.

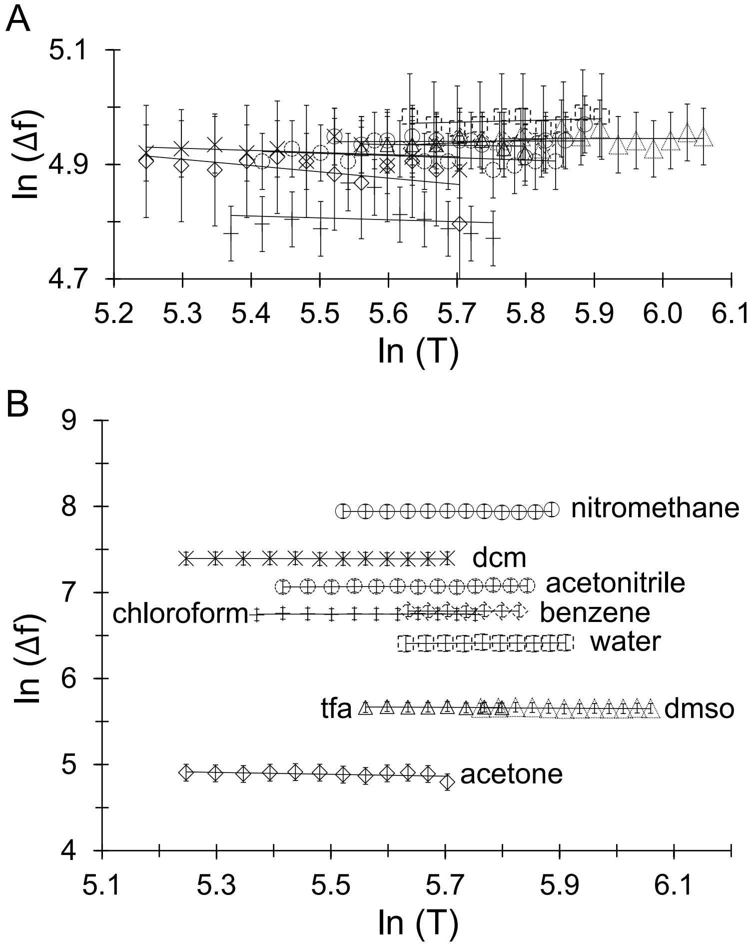

Figure 2.3: Temperature dependence of linewidth (Δf) in liquids. Nine different liquids were investigated, as shown by the different symbols. The values of $\ln(T)$ shown span the temperature range $T = 180 - 450$ K. A) For a fixed gradient strength of g=0.05 G/cm, all linewidths were broadened by a similar amount, hence the overlap in the data. At fixed g, the linewidth did not exhibit any detectable dependence on temperature. B) Increasing applied gradient strength did not alter the independence of linewidth on temperature. Applied gradient strengths were: nitromethane (1 G/cm), dichloromethane (dcm, 0.5 G/cm), acetonitrile (0.4 G/cm), chloroform (0.3 G/cm), benzene (0.3 G/cm), water (0.2 G/cm), trifluoroacetic acid (tfa, 0.1 G/cm), dimethyl sulfoxide (dmso, 0.1 G/cm), acetone (0.05 G/cm). Symbol in A refers to the same liquid as in B.

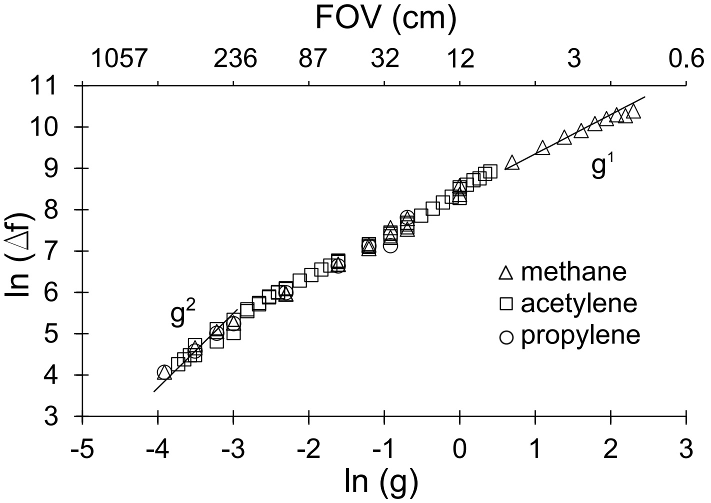

Figure 2.4: Dependence of linewidth (Δf) on applied gradient strength (g) for gases. Three different gases were investigated. Two different regimes are found: in the limit of strong applied gradients, Δf scales as $g^{1.0\pm0.1}$ whereas for weak gradients Δf scales as $g^{1.8\pm0.2}$. All data was acquired at ambient temperature.

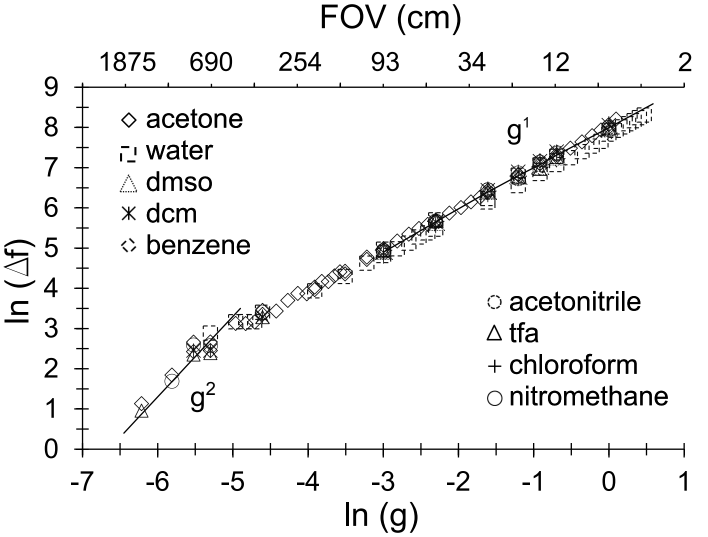

Figure 2.5: Dependence of linewidth (Δf) on gradient strength (g) for liquids. Nine different liquids were investigated. Two different regimes are found: in the limit of strong applied gradients, Δf scales as $g^{1.1\pm0.1}$ whereas for weak gradients Δf scales as $g^{2.0\pm0.2}$. All data was acquired at ambient temperature.

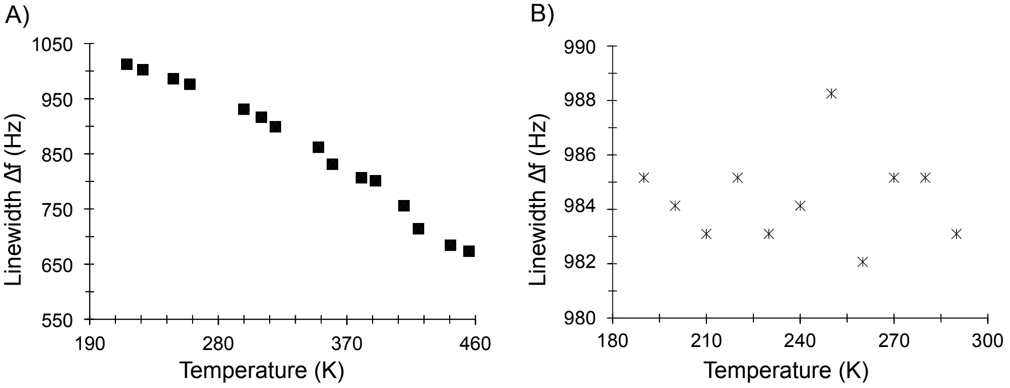

Figure 2.6: A) Raw linewidth vs. temperature data for methane gas. The applied gradient strength was $g = 0.15$ G/cm, with FOV = 78 cm. B) Raw linewidth vs. temperature data for liquid dichloromethane. The applied gradient strength was $g = 0.3$ G/cm, with FOV = 94 cm.

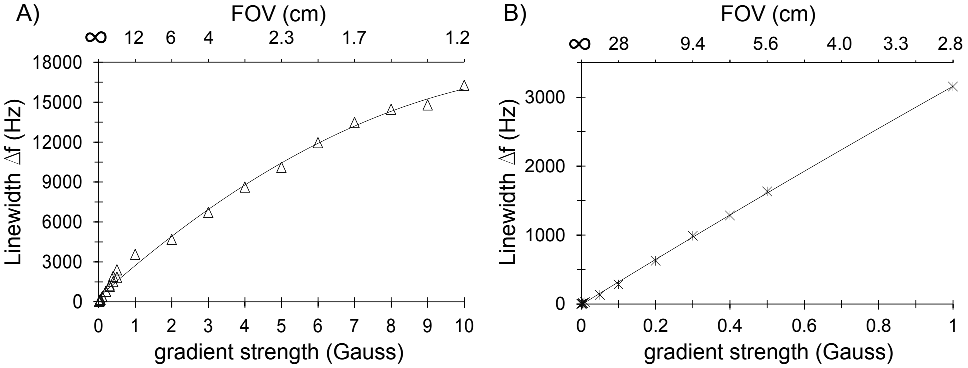

Figure 2.7: A) Raw linewidth vs. gradient data for methane gas, acquired at 220 K. B) Raw linewidth vs. gradient data for liquid dichloromethane, acquired at 300 K. The continuous curves drawn through the data points are guides to the eye, and are not actual fits.

CHAPTER 3

Breakdown of CPMG Spin Echoes in Inhomogeneous Fields

Previously, we found that the decay of nuclear induction signal in a magnetic field gradient differs fundamentally in gases compared to liquids, as manifested in the temperature dependence of the nuclear magnetic resonance (NMR) linewidth [4, 7]. In the conventional description of NMR, spectral lines should broaden in a gradient of the magnetic field as temperature increases [25], which results in a larger diffusion coefficient. However, we found experimentally that in gases, the NMR linewidth instead *decreases* with temperature, which is consistent with a motional narrowing effect. The importance of this motional narrowing effect was not predicted by the conventional theory. In this chapter, we demonstrate that this difference in motional averaging between gases and liquids also manifests itself in the signal decay of CPMG spin echoes. In liquids, a series of spin echoes in the limit of short interpulse spacings minimizes signal decay effects due to diffusion in a gradient (as expected from the conventional theory [25]). For gases, however, we find that CPMG is unable to eliminate this signal decay in the limit of short interpulse spacings. This result implies that any T_2- or diffusion-weighted NMR measurements of gases made in the presence of magnetic susceptibility gradients or applied field-gradients are potentially compromised.

In a $90^\circ - \tau - 180^\circ - \tau$ spin-echo experiment the free induction signal in the presence of a magnetic field gradient is given by Hahn's famous result [25, 40]:

$$S(\tau) = \exp\left(-2\tau/T_2\right)\exp\left(-\frac{2}{3}\gamma^2 g^2 D\tau^3\right), \tag{3.1}$$

in which 2τ is the evolution time (total length of the spin-echo experiment), T_2 is the intrinsic spin-spin relaxation time, γ is the nuclear gyromagnetic ratio, D is the self-diffusion coefficient, and g is the magnetic field gradient ($g = \partial H_z/\partial r$, where r is a spatial direction). In the absence of a large magnetic field inhomogeneity and large diffusivity the expres-

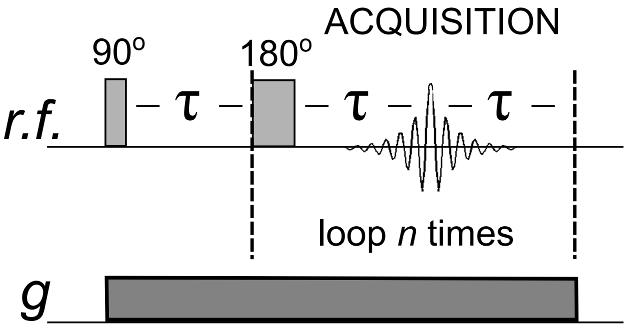

Figure 3.1: Measurement of T_2 in an inhomogeneous field (gradient, g) using a CPMG sequence. A 90° radio-frequency (r.f.) pulse tips the magnetization, which is refocussed by a series of n 180° pulses at intervals of 2τ.

sion collapses to $\exp(-2\tau/T_2)$. This result (Eq. 3.1) assumes that the Einstein-Fick limit holds, implying that we can make the approximation to the position autocorrelation function (PAF), $\langle x(t)x(0)\rangle \approx \langle x(t)x(t)\rangle = 2Dt$, i.e., the PAF is approximated by the mean-square displacement.

According to the same conventional theory, the signal in the CPMG experiment, which features a train of n echoes (Fig. 3.1), decays according to [25,41,42]:

$$S(\tau) = \exp(-n2\tau/T_2)\exp\Bigg(-\frac{1}{3}\gamma^2 g^2 D\tau^2(n2\tau)\Bigg), \tag{3.2}$$

where $n2\tau$ is the total duration of the sequence, which is held fixed. In practice, an upper bound on $2n\tau$ is imposed by the relaxation time of the sample. In the limit of short echo spacing ($\tau \to 0$, holding $n2\tau$ constant) CPMG minimizes the effect of molecular self-diffusion on nuclear spin decoherence in inhomogeneous magnetic fields. Under these conditions, the contribution of the inhomogeneous term becomes negligible, recovering $\exp(-n2\tau/T_2)$.

However, the expression in Eq. 3.2 only holds for substances whose diffusional properties obey the Einstein-Fick limit, which mainly applies to liquids. Gases typically lie outside the Einstein-Fick limit. We have derived in prior work an expression for signal decay in gases [4,7]:

$$S(\tau) = \exp(-2\tau/T_2)\exp\Bigg(-\gamma^2 g^2\kappa\tau\Bigg), \tag{3.3}$$

where κ is a term that depends on the PAF of diffusing molecules. It depends, among other things, on temperature and viscosity. We note that the time dependence is τ, not τ^3. This difference in exponents has important consequences. Namely, the application of a CPMG sequence with n echoes,

$$S(\tau) = \exp\left(-2n\tau/T_2\right) \exp\Bigg(-\gamma^2 g^2 \kappa (2n\tau)\Bigg). \tag{3.4}$$

no longer eliminates the second term describing inhomogeneous-field decay in the limit of short interpulse spacing $\tau \to 0$ ($2n\tau$ is fixed). Thus, any measurement of T_2 in a gas using a CPMG sequence will yield an *apparent* T_2 value that is affected by diffusivity effects in the inhomogeneous magnetic field. This could include, for example, unwanted weightings due to temperature, viscosity, external hardware, pulse sequence design, magnetic susceptibility and pore geometry. This is in contrast to the case of liquids, where diffusion effects can be mitigated by extrapolation to extract the true (intrinsic) T_2 time.

Consider the CPMG experiment (Fig. 3.1) with a 90° broadband pulse and a series of 180° pulses to refocus the magnetization at intervals of 2τ. The following phases were applied in the CPMG sequence: $90°_x - \tau - (180°_y - \tau - \tau)^n$, where the 180° pulse is repeated n times. For each τ value, the echo envelope was acquired in a single-shot experiment. An external magnetic field gradient during the course of the experiment creates an inhomogeneous magnetic field. For gas-phase experiments, a sealable 5-mm diameter J. Young NMR tube was filled with liquid and freeze-pump-thawed to evacuate excess air. The NMR tube was heated by the NMR spectrometer's variable temperature unit until the tube was vaporized. For liquid-phase experiments, a solution of 0.5% weight/volume tetramethylsilane (TMS) in acetone-d_6 was degassed and flame-sealed in an NMR tube. Measurements were performed on a 14.1 T vertical bore Bruker AV 600 MHz NMR spectrometer equipped with a 5 mm broadband probe with a z-gradient. The receiver was operated in qsim mode (forward Fourier transform, quadrature detection). The pulses were hard pulses whose lengths were 16 μs and 32 μs for the 90° and 180° pulses, respectively. The size of the sensitive RF region is less than 1 cm. All NMR signals were analyzed in magnitude mode and decay functions included baseline subtraction.

3.1 Experimental Results and Discussion

We take an explicit look at the time-decay of the CPMG echo train, which the theory (c.f. Eq. 3.1 and 3.3) predicts should exhibit fundamentally different behavior (t^3 vs t^1, respectively). A direct verification is obtained by plotting the NMR signal in the CPMG experiment versus time along the echo train (see Fig. 3.2). The normalized NMR signal decay of the CPMG spin echo (with an interpulse spacing of 5 ms) for liquid-phase TMS is plotted in Fig. 3.2a. The normalized NMR signal decay of the CPMG spin echo (with an interpulse spacing of 5 ms) is plotted in Fig. 3.2b for gas-phase TMS. For gas, the normalized NMR signal decays exponentially, according to $\exp(-t/T_2)\exp(-t/b)$, in agreement with our revised theory of the NMR linewidth. We note that neither alteration of the phase cycling scheme to $90°_x - (180°_y - 180°_{-y})_n$ nor replacement of the 180° pulse with a $90^\circ_x/180^\circ_y/90^\circ_x$ composite pulse affected the results.

Measurements of the CPMG echo train signal decay as a function of interpulse spacing τ for TMS in the liquid phase are shown in Fig. 3.3a. Figure 3.3b shows the corresponding experiment in the gas phase. TMS is a liquid at room temperature but a gas at 26° C; thus, a modest temperature increase enables comparison of the same substance in two different phases. TMS was also chosen due to its long relaxation times in both liquid and gas phases, enabling us to apply a large number of refocusing pulses even at long τ values. For liquids, as the interpulse spacing decreases the measured T_2 value approaches a single value irrespective of the applied gradient strength g, as if there were no external gradient (Fig. 3.3a,c). This corresponds to the limit $\tau \to 0$ in Eq. 3.2. Extrapolation of T_2 to the limit $\tau \to 0$ is the most commonly used method to extract true T_2 times in the presence of magnetic-field inhomogeneities (from external or internal fields). For gases, however, the T_2 values in the limit $\tau \to 0$ do not approach a single value (Fig. 3.3b,d), but instead converge to different values depending on the applied gradient strength g. This fundamentally different behavior implies that the inhomogeneous-field decay term is still present, as predicted by Eq. 3.4.

In this study we have confirmed the t^1 dependence in the NMR signal decay function of gases in the presence of an external gradient (Eq. 3.3 and 3.4). In our prior work we

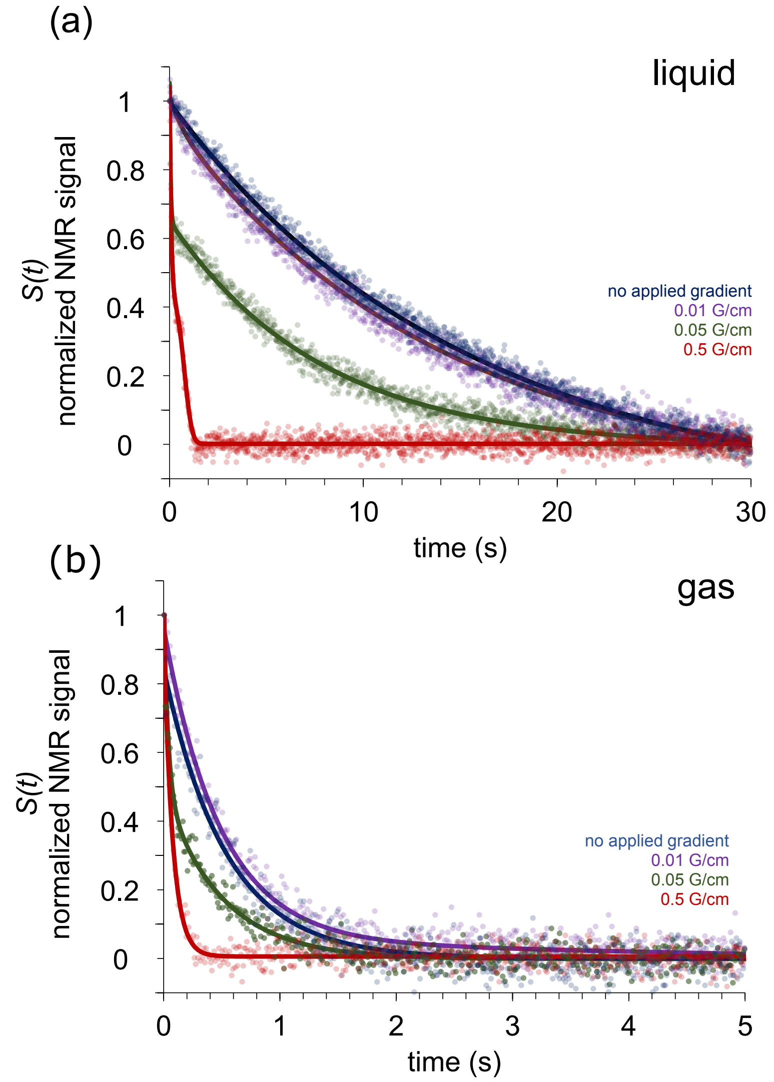

Figure 3.2: Direct verification that signal decay in the presence of a magnetic-field gradient follows a time dependence of the form $\exp(-t/T_2)\exp(-t/b)$ for the gas and $\exp(-t/T_2)\exp(-(t/b_2)^3)$ for the liquid (solid lines, fit; dots, data). Here we show sample CPMG decay curves for τ=5 ms and g=0, 0.01, 0.05 and 0.5 G/cm. (a) Liquid-phase TMS (t^1). Number of scans (ns) = 1. (b) Gas-phase TMS (t^3). ns = 8. In both liquid and gas cases, we scanned multiple acquisitions (of ns = 1 and 8 for liquid and gas respectively) and a T_2 value with experimental error bars was derived for Figure 3. The fits to the respective models are excellent. Fits to the converse equation ($t^1 \leftrightarrow t^3$) do not yield acceptable fits (not shown here).

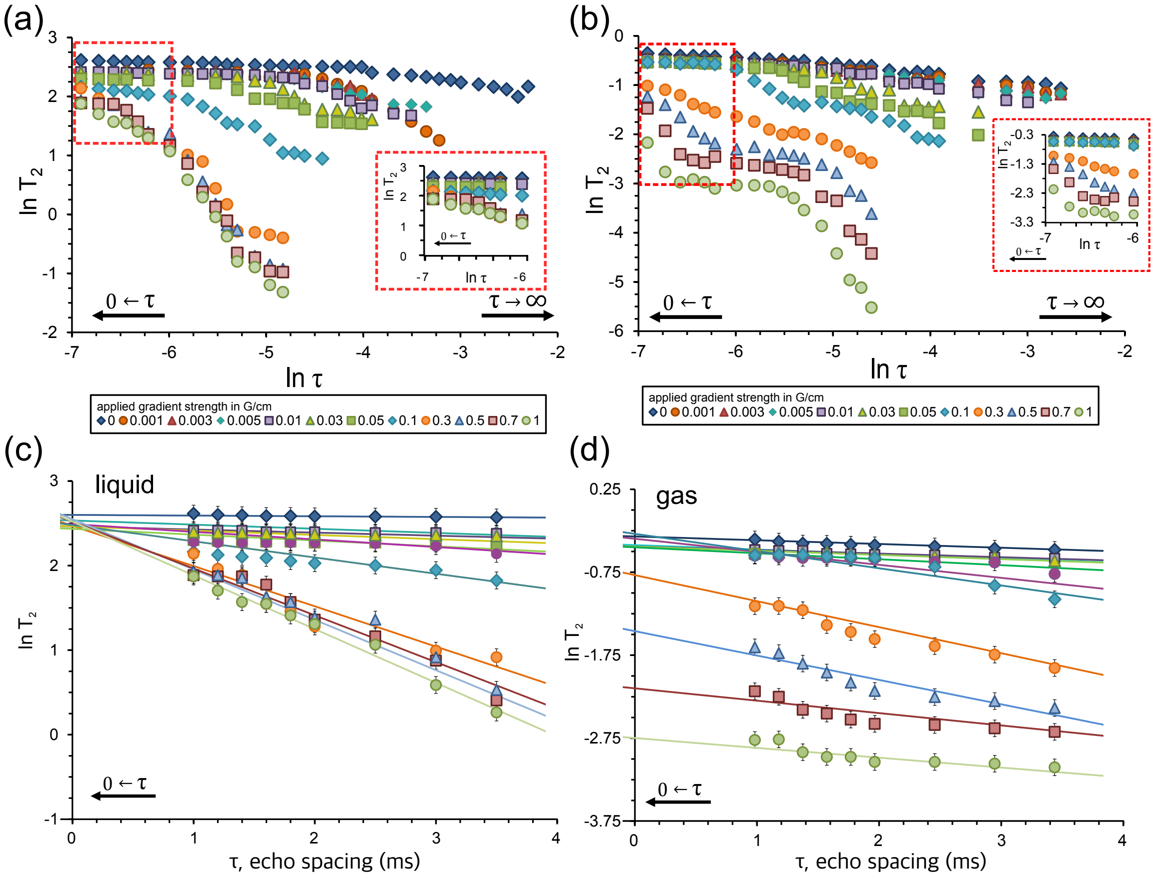

Figure 3.3: T_2 relaxation time of tetramethylsilane (TMS) vs interpulse spacing τ under conditions of magnetic field inhomogeneity (field gradient g, in G/cm). (a) Liquid-phase T_2 values approach the limit of no applied gradient as $\tau \to 0$. T_2 values shown range from 50 ms to 20 s. τ values shown range from 1 ms to 100 ms. Inset: Expansion of red boxed region. (b) Gas-phase T_2 values do not converge to a single value as $\tau \to 0$. T_2 values shown range from 18 ms to 1 s. τ values shown range from 1 ms to 100 ms. Inset: Expansion of red boxed region in A. (c) Data from (a) plotted on a linear scale. The straight lines are linear extrapolations as $\tau \to 0$. The g values are the same as in (a). (d) Data from (b) plotted on a linear scale. The straight lines are linear extrapolations as $\tau \to 0$. The g values are the same as in (b).

had verified the temperature dependence of the linewidth [4]. The verification of the t^1 time dependence can be considered the missing part of the puzzle which now unambiguously confirms the validity of the revised linewidth theory presented in Ref. [4]. The g^2 dependence has already been verified in our previous paper [4].

The fundamentally different motional averaging behavior of the NMR experiment in gases has important implications for several experiments. This behavior has previously led to the development of a novel non-invasive method for mapping temperatures of gases [5]. Gas-phase MRI experiments that utilize frequency-encoding gradients could be affected; gradients during readout affect measurements of T_2 or diffusion, introducing an apparent coupling between them. This means that a quantitative interpretation of these parameters would need to account for the non-Fickian nature of the diffusion. Dynamic decoupling schemes such as the Uhrig sequence [131], which aim at generating the longest possible coherence times, are also expected to break down in the case of gases because short τ values no longer guarantee the elimination of environmental factors. Finally, the interpretation of restricted diffusion results [3, 132–139] in porous media and other confined geometries may require new theoretical developments that model the signal decay in restricted environments in light of the new theory of signal decay.

3.2 Control Experiments

3.2.1 Phase cycling and RF homogeneity

We have carried out experiments to verify that different phase cycling schemes or better quality RF pulses do not affect the results. Namely, we have found no difference between 90_x–$(180^\circ_y$–$180^\circ_{-y})_n$ and the Meiboom-Gill modification of the Carr-Purcell experiment [90_x–$(180^\circ_y$– $180^\circ_y)_n$]. The T_2 values were the same, as demonstrated by the overlapping traces in Figure 3.2.1 below.

To rule out problems from imperfect RF pulses, experiments were done using composite refocusing pulses (90°_x / 180°_y / 90°_x). The results from the composite refocusing pulses are shown in Figure 3.2.1 and compared to the case of single, hard refocusing pulses. No

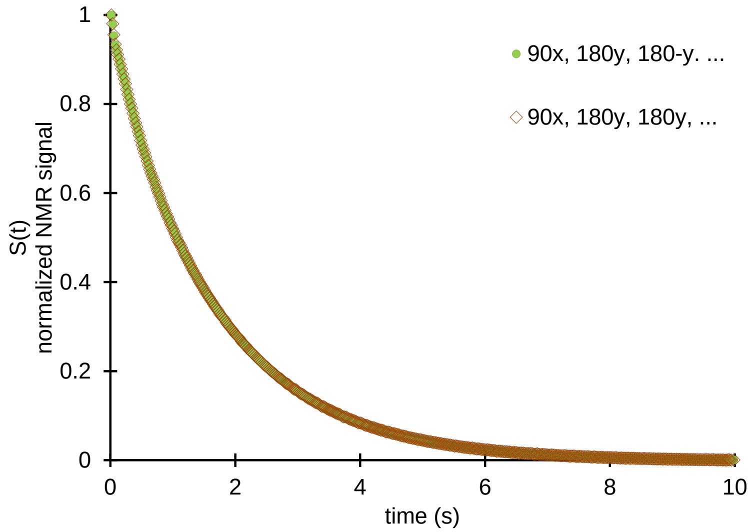

Figure 3.4: Signal decay of echo envelopes from multiple-spin-echo experiment in liquid water. $\tau = 10$ ms. The trace was acquired in a single-shot; the points shown are the sum of signal for each echo, integrated over the time window between two consecutive RF pulses. The green trace is the phase cycling 90°_x–$(180^\circ_y$–$180^\circ_{-y})_n$ (green trace), and the "CPMG" phase cycling used in the paper 90°_x–$(180^\circ_y$–$180^\circ_y)_n$ (red squares) overlap almost perfectly.

significant difference in the decay rate was observed.

We found no difference in the multiple-spin-echo experiment's inability to eliminate the inhomogeneous broadening in gases (i.e., T_2 values for gas still did not converge to a single value in the limit of short τ).

3.2.2 Convection currents

We have carried out experiments to rule out the possible contribution from convection currents. We have approached this problem from three different angles:

1. We can measure the temperature gradients directly in the NMR tube by imaging the temperature of the gas. In [4, 7] we found that the linewidth for a gas is linearly dependent on temperature; the slope from a plot of linewidth vs temperature yields a

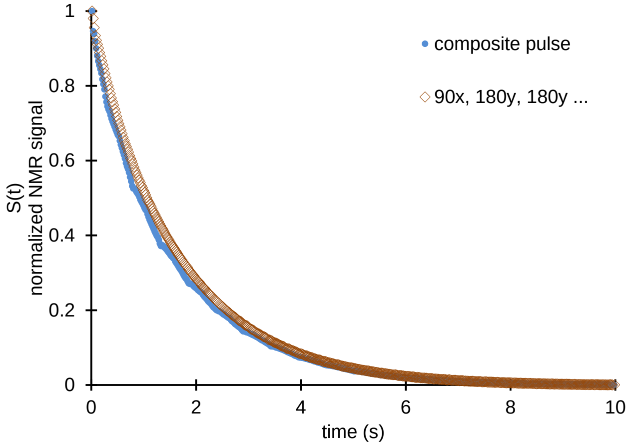

Figure 3.5: Comparison of composite pulses vs regular hard pulses in a multiple-spin echo experiment. The decay rates are seen to be nearly identical. $\tau = 10$ ms

"temperature coefficient."

The absence of significant temperature gradients would mean that convection currents are not of concern. Temperature maps are shown in Figure 1 in the case of the NMR tube held at different temperatures. The temperature mapping method is described in [5]. As can be seen, no significant temperature gradients exist within the NMR tube.

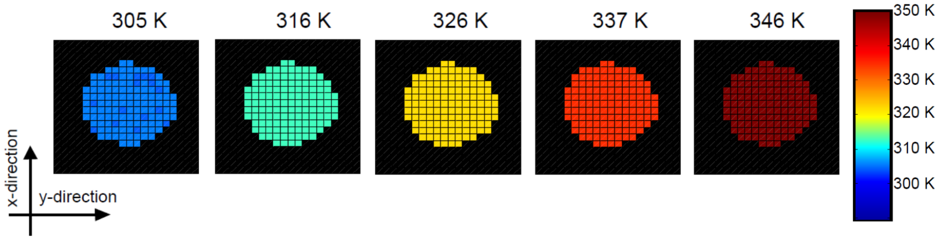

Figure 3.6: Temperature maps (axial images) of propylene gas in the NMR tube. The temperatures are derived from the "temperature coefficient" that relates NMR linewidth to temperature. The temperature dependence is described in [4]. The temperature mapping method is described in [5].

2. We can pack the NMR tube with powders to restrict the transport of gas molecules. If a driving force for convection exists, it should be significantly reduced in the presence of powder. In Figure 3.7, the NMR tube was packed using different powders to create porous media: metal organic framework MOF-5, zeolitic imidazolate framework ZIF-8, silica gel, and a comparison with pure gas (no powder). (These are all fine powders, ∼ 1-10 μm grain size.)

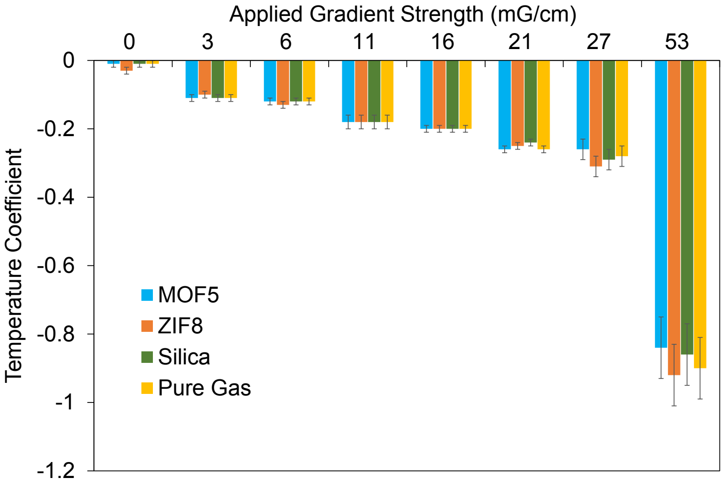

Figure 3.7: Gas inside a porous media also displays temperature dependence of NMR linewidth as a function of applied gradient strength.

In [4], we found that the linewidth for a gas is linearly dependent on temperature; the slope from a plot of linewidth vs temperature yields a "temperature coefficient" that should only depend on the applied gradient strength. If convection plays a role, the convection currents will be stronger at higher temperatures (where the temperature gradients are expected to be stronger). Convection would result in a different temperature coefficient because heat is transported elsewhere. In all 4 cases shown in Fig. 3.7, the obtained temperature coefficient only depends on the applied gradient, and does not depend on the packing. Since adding a packing does not alter the temperature coefficient, convection does not likely play an important role here.

3. One final check we can do is measure the dependence of the temperature coefficient on pressure. Since convection depends on pressure (through the pressure dependence of the fluid viscosity), such experiments as function of pressure would tell us if the results are possibly affected by convection. The results shown in Figure 3.8 demonstrate that the temperature coefficient is independent of the gas pressures (figure shows propylene gas at 1, 3 and 5 atm pressures). Thus, convection currents do not likely play a significant role.

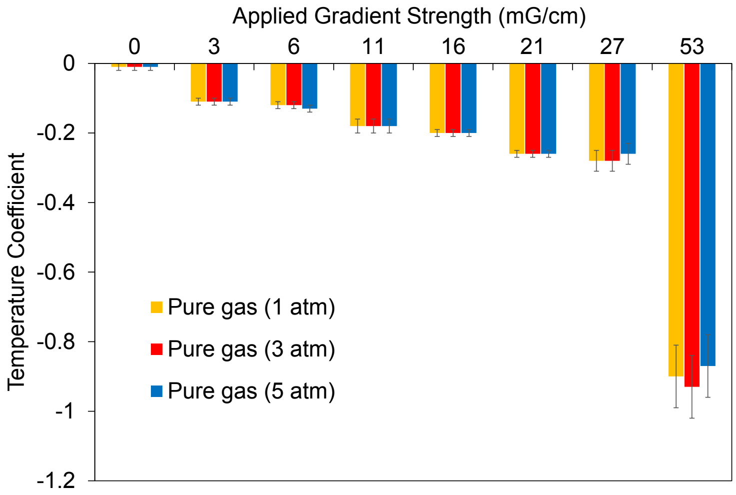

Figure 3.8: Pure gas displays temperature dependence of NMR linewidth as a function of applied gradient strength.

3.2.3 The free diffusion regime

Our experiments probe the NMR signal in the free diffusion regime because the NMR tube size is much larger than the diffusion length. The rms diffusion length l_D is the shortest length scale (for $\tau = 5$ ms, $l_D = 44$ μm for gas and $l_D = 7$ μm for liquid). According to [3], we are in the free diffusion regime, in which both the distance between boundaries l_s is much longer than the diffusion length, i.e., $l_D/l_s \ll 1$. Our NMR tube, $l_s = 3$ mm, is much larger than the rms diffusion length l_D. Additionally, the regime we probe can be distinguished from so-called "motional averaging" and "localization" regimes because our diffusion length

l_D is much greater than our dephasing length l_g, i.e., $l_D/l_g \ll 1$. For our gradient regime (no applied gradient to 1 G/cm), the dephasing lengths ranged from 400 μm to 4 mm, which is at least one order of magnitude larger than our diffusion length. In this regime, only a negligible fraction of molecules collide with the walls.

3.2.4 Supplementary Equations

3.2.4.1 Mean square displacement

It is customary to assume $x(0) = 0$ in such derivations of the ms-displacement and 2) the formula was obtained in the limit $t \gg 1/\gamma$ (Fick limit) and we cannot simply set $t = 0$ afterwards. (See below.) The starting point is the Itô SDE for the velocity process:

$$dv(t) = -\gamma v dt + (\Gamma/M) dw(t),$$

where $dw(t)$ is the increment of the Wiener process. The solution is

$$v(t) = v_0 e^{-\gamma t} + (\Gamma/M) e^{-\gamma t} \int_0^t e^{\gamma t'} dw(t'),$$

where $\Gamma^2 = 2\gamma M k_B T$ by the fluctuation-dissipation theorem. Since $dx(t) = v(t)dt$, integration gives, assuming $x(0) = 0$:

$$x(t) = \frac{v_0}{\gamma}(1 - e^{-\gamma t}) + \sqrt{\frac{2\gamma k_B T}{M}} \int_0^t dt' e^{-\gamma t'} \int_0^{t'} dw(t'') e^{\gamma t''},$$

where $v_0 = \sqrt{k_B T/M}$. Squaring and averaging, we get the mean-square displacement:

$$\langle x^2(t) \rangle = \frac{2k_B T}{M\gamma} t + \frac{v_0^2}{\gamma^2}(1 - e^{-\gamma t})^2 - \frac{k_B T}{M\gamma^2}(3 - 4e^{-\gamma t} + e^{-2\gamma t}),$$

which goes to zero, $\langle x^2(t) \rangle \to 0$, when $t \to 0$, but only because it was assumed that $x(0) = 0$. The Einstein-Fick limit ($t \to \infty$) is:

$$\lim_{t \to \infty} \langle x^2(t) \rangle = 2Dt, \quad D = \frac{k_B T}{M\gamma},$$

which goes to zero, $\langle x^2(t) \rangle \to 0$, when $t \to 0$. After all, we have assumed that $x(0) = 0$. However, we did take the Fick limit $t \to \infty$, so it is not quite right to set $t = 0$. If we had not assumed that $x(0) \equiv x_0 = 0$, the ms-displacement would have been

$$\langle x^2(t) \rangle = x_0^2 + \frac{2x_0 v_0}{\gamma}(1 - e^{-\gamma t}) + \frac{2k_B T}{M\gamma} t + \frac{v_0^2}{\gamma^2}(1 - e^{-\gamma t})^2 - \frac{k_B T}{M\gamma^2}(3 - 4e^{-\gamma t} + e^{-2\gamma t}).$$

This is the appropriate formulate to use for $t = 0$, with nonzero initial condition. Taking the limit $t \to 0$ gives the correct result $\langle x^2(t)\rangle = x_0^2$ cited by the referee. In the Fick limit ($t \to \infty$), the exponential factors rapidly vanish, and we are left with the same result as when we assumed $x(0) = 0$:

$$\lim_{t\to\infty}\langle x^2(t)\rangle = x_0^2 + \frac{2x_0 v_0}{\gamma} + \frac{2k_B T}{M\gamma}t + \frac{v_0^2}{\gamma^2} - \frac{3k_B T}{M\gamma^2} \to \frac{2k_B T}{M\gamma}t \text{ as } t \to \infty,$$

since the term $\frac{2k_BT}{M\gamma}t$ is much larger than any of the constant terms in that limit, including x_0^2. But for the same reason as cited previously, we are not allowed to simply set $t = 0$, even with this expression, since we have already taken the limit $t \to \infty$. This would yield $\langle x(0)^2\rangle = 0 \neq x_0^2$, which is clearly incorrect, as we did not assume that $x_0 = 0$. The explicit reference to the Fick limit makes it clear that it is not permissible to simply set $t = 0$ and expect that $\langle x(0)^2\rangle = 0$ when $x(0) \neq 0$.

CHAPTER 4

Thermal Maps of Gases in Heterogeneous Reactions

Figure 4.1 summarizes our technique, which exploits the effect of motional averaging in a weak magnetic field gradient (1 G/cm). Nuclear spins acquire a random phase shift owing to the stochastic trajectories of molecules in the presence of a magnetic field gradient. This dephasing leads to faster signal decay, and spectral peaks are consequently broadened. Higher temperatures accelerate molecular motion [140], leading to more efficient temporal averaging of the applied gradient (Fig. 4.1a). This method is a powerful complement to existing techniques for visualizing catalytic reactions under a range of experimental conditions [33–35, 141–147].

The pulse sequence separates the phase-encoding scheme from the detection period to yield spectroscopic images. We apply a constant magnetic field gradient during the detection period to introduce temperature-dependent line broadening. This gradient differs from a conventional frequency-encoding gradient or pulsed-field-gradient NMR [2] because it is much too weak to provide spatial encoding of the image or signal attenuation, respectively. When imaging gradients are used, Fourier transformation of the data set with respect to reciprocal space of the phase-encoding scheme yields an image containing a one-dimensional NMR spectrum in each voxel. The linewidth variations in each voxel are converted into temperatures using the calibration described below.

4.1 Experimental Results and Discussion

We tested this method over a temperature range of 293-443 K using a catalyst-packed, laboratory-scale demonstration reactor in which propylene and hydrogen reacted to form propane. The dependence of linewidth on temperature was calibrated over the entire reactor by omitting phase-encoding gradients and comparing the observed linewidth against

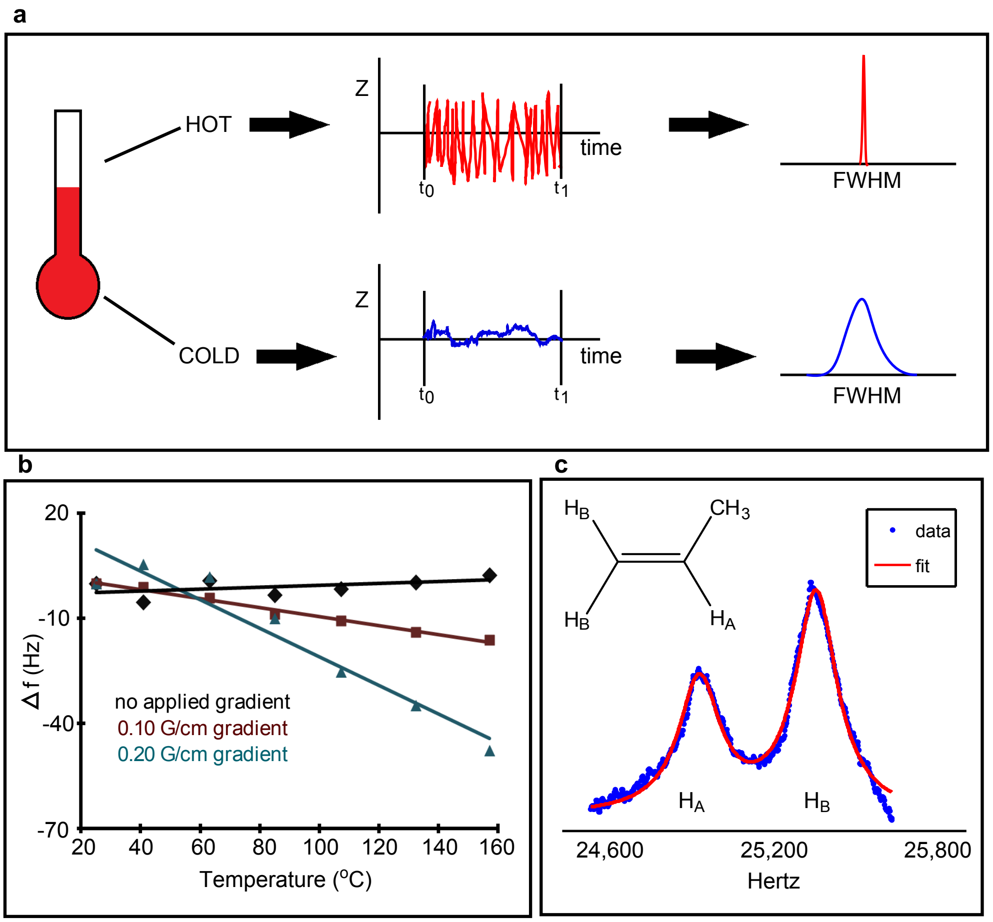

Figure 4.1: a) At higher temperatures, gas molecules move faster and molecular motion averages the effects of the dephasing gradient. Because the spins experience more of the average magnetic field, linewidths are narrower. FWHM, full-width at half-maximum. b) Without a gradient, the linewidth is weakly dependent on temperature. As we turn on the external gradient, the linewidth dependence on temperature grows and becomes independent of the nature of the porous medium. c) In the calibration experiment of b, we fit the propylene spectrum at each temperature to a sum of Lorentzian distributions to extract the linewidth. Temperature calibrations were performed for over 30 different systems. The particular data shown in b is an example of one system.

temperatures measured by fiber-optic temperature sensors. To get absolute temperatures, the temperature scale must be fixed by placing a sensor at a convenient location where perturbation of the flow is minimal (for example, near an inlet or outlet). In the absence of an applied gradient, measured linewidths in the chemical reactor system (Fig. 4.2) show negligible temperature dependence (Fig. 4.1b); internal magnetic field inhomogeneities are thus too weak to produce any significant effects. The situation changes when we apply a gradient to deliberately broaden the lines (Fig. 4.1c), with a modest gradient (0.10 G/cm) yielding a temperature dependence of -0.130 ± 0.006 Hz/K (Fig. 4.1b). Stronger gradients lead to stronger temperature dependence (Fig. 4.1b). The temperature dependence over this temperature range is well modeled by a linear regression.

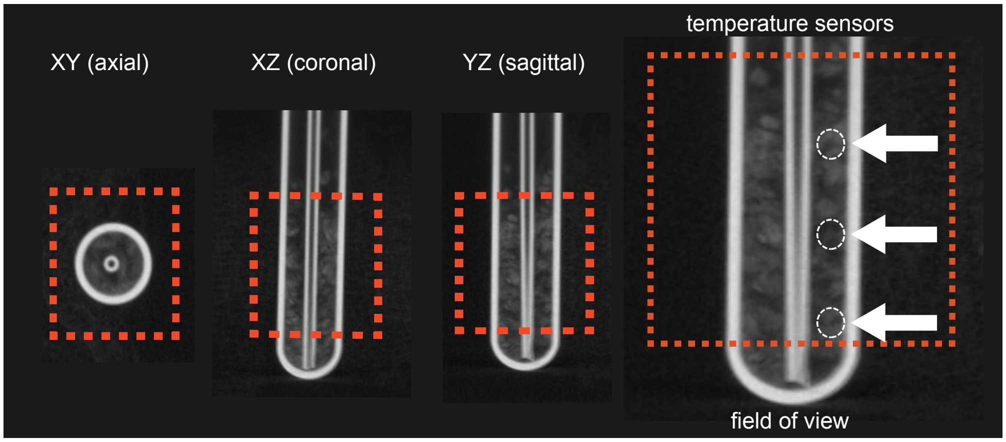

Figure 4.2: Orthogonal slices of the system determined by micro-computed tomography. The reactor shown here consists of a 10-mm Pyrex NMR tube, a gas inlet tube and a heterogeneous catalyst loaded on glass wool. To validate the NMR method, independent temperature measurements were made using fiber-optic probes placed at three different locations (arrows) within the NMR field of view (FOV). The approximate location of the FOV is indicated by the dashed box. The axial, coronal and sagittal planes correspond to those in Fig. 4.3.

Figure 4.3 depicts thermal maps of two reactors, each packed with a different catalyst: Pt nanoparticles (PtNP) or a multivariate metal-organic framework metallated with Pd (Pd-MOF) supported on glass wool. For the PtNP reactor system, a magnetic field gradient of 0.05 G/cm causes the propylene linewidth to have the form:

$$\Delta f(Hz) = [-0.16 \pm 0.01(Hz/K)]T(K) + [151 \pm 1(Hz)], \qquad (4.1)$$

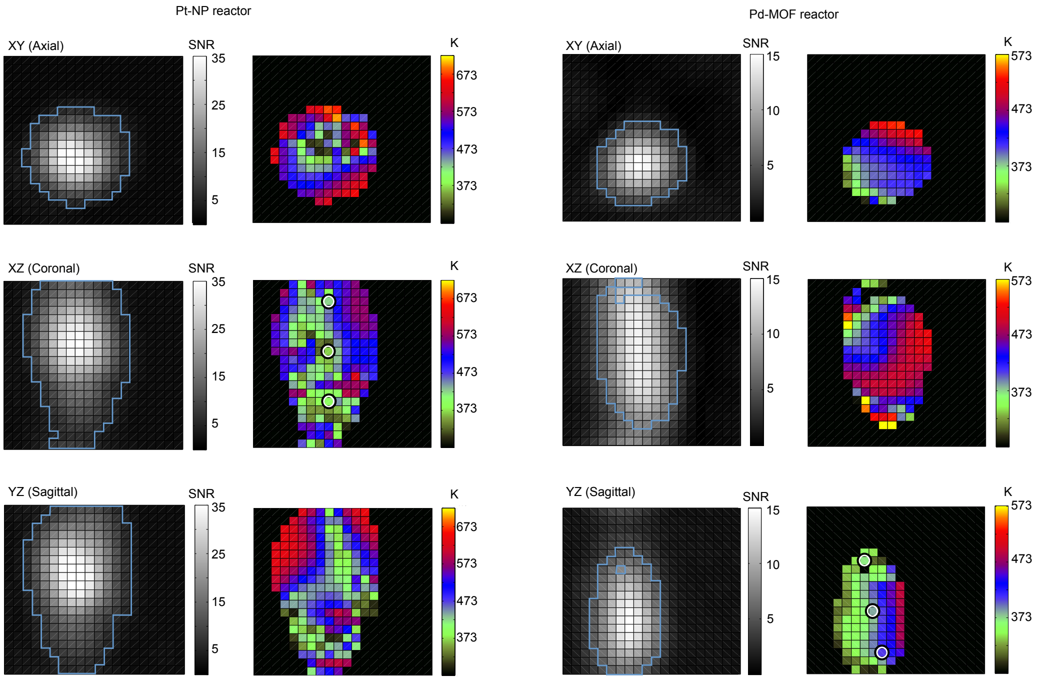

Figure 4.3: a), b) Two-dimensional NMR signal-to-noise ratio (SNR) maps (greyscale) and corresponding gas-phase thermal maps (color) of one reactor packed with 10-mm PtNP (a) and another packed with Pd-MOF (b). SNR maps detail the signal intensity of proton resonances used to derive the temperature. Each pixel corresponds to an in-plane, 0.73 mm × 0.73 mm region and is assigned a linewidth-based temperature. Temperature was calculated only for pixels with SNR> 4 (blue outline). The temperature measurement was confirmed by fiber-optic temperature sensors placed within the FOV, indicated by circles on the thermal maps. Sensor probe alignment relative to the reactor is shown in Fig. 4.2. Thermal maps were generated for more than 15 experiments. The particular thermal maps shown above are two representative examples of those maps.

where T is temperature. the Pd-MOF system and an identical gradient, the linewidth is:

$$\Delta f(Hz) = [-0.10 \pm 0.01(Hz/K)]T(K) + [119 \pm 1(Hz)]. \tag{4.2}$$

The slopes of the lines described by equations 4.1 and 4.2, which encode the temperature dependences of the linewidths, together with the point-sensor readout reference, yield absolute temperature maps for the PtNP and Pd-MOF reactor beds, respectively. Figure 4.3 shows the thermal images for axial, sagittal, and coronal views in which only pixels with a signal-to-noise ratio (SNR) greater than four are displayed. These images show significant temperature variations throughout the catalyst bed, as expected for a heterogeneous reactor. The temperature inhomogeneities correlate with both the packing of the catalyst-impregnated glass wool (Fig. 4.3) and also the placement of the inlet and the outlet of the reactor. Owing to non-uniform catalyst packing, some regions are more active than others, leading to differences in catalytic conversion ("hot spots" and "cold spots"). Another application of such thermal maps, if the heat capacity of the medium is known, would be to map spatial gradients in the internal energy (U) of the reaction through the thermodynamic relationship $\Delta U = C_V \Delta T$. From these, we could derive a fundamental thermodynamic quantity, ΔU, of the reaction, which reveals the flow of energy. The effective heat capacity of the medium (C_V) could potentially be inferred from microcomputed tomography images such as those of Fig. 4.2. The characteristic length scales of $|\Delta T|$ could be compared with those of the microcomputed tomography map in similar reactors to gain insight into the thermal flux of the system.

To validate the NMR-derived temperature measurements, three fiberfiber-optic temperature sensors were placed at the centre of the FOV, and 4 mm below and 4 mm above the FOV centre (Fig. 4.3). The sensors in the PtNP reactor measured temperatures of 398, 412 and 427 K, which correspond well to the NMR-derived temperatures in the coronal map (that is, 400, 417 and 424 K). Similarly, the in situ temperature measurements in the Pd-MOF reactor gave 382, 411 and 425 K, which compare well with the NMR-derived measurements in the sagittal map (that is, 389, 416 and 441 K). The random error in the NMR-derived temperature measurement

$$\frac{\delta T}{T} = \sqrt{\left(\frac{\delta(\Delta f)}{\Delta f}\right)^2 + \left(\frac{\delta(\Delta f/\Delta T)}{\Delta f/\Delta T}\right)^2} \tag{4.3}$$

was calculated to be 4% on the Kelvin scale using the using the relative errors in the linear regression, $\delta(\Delta f)/\Delta f$ and $\delta(\Delta f/\Delta T)/(\Delta f/\Delta T)$ where Δf is the linewidth from the fit of the spectrum and $\Delta f/\Delta T$ is the slope of the temperature calibration curve. The disagreement between NMR-derived temperatures and fiber-optic-sensor measurements was at most 4%, thus, systematic errors for the systems studied were not significant. The correspondence of these results demonstrates the ability to map temperatures of reacting gases inside an operating catalytic reactor with millimetre resolution using the NMR signal from thermally polarized protons.

The above proof-of-principle experiments used a 10-mm reactor; so 1-mm outer diameter point sensors are much smaller than the reactor and thus cause minimal perturbation of the flow. Once validated, the method can be used on smaller reactors with only a single reference temperature measured at a convenient location outside the reactor bed to avoid perturbing the flow. Thermal maps of a microreactor are shown in Fig. 4.4, where para-state-enriched hydrogen [143–147] was used as reactant to overcome the loss of signal associated with the smaller image voxels. This reactor was packed without glass wool support.

NMR thermometry based on the nuclear spin-lattice relaxation time (T_1) or spin-spin relaxation time (T_2) is widely applicable in liquids, but either impractical or insensitive when applied to gas-phase reactions: T_2 measured over the temperature range 303-413 K lacked a statistically significant temperature dependence, and inversion-recovery measurements showed that T_1 is temperature dependent (-2.3 ± 0.2 ms/K) but required a minimum of 51 inversion times to yield temperature measurements with comparable precision (equating to a scan time of 1,000 h to create thermal maps). If the number of inversion-recovery steps is reduced to four, the error in temperature would be a factor of forty greater than with our motional-averaging technique and the scan time would still be a factor of five times longer ($\approx$ 2.5 h) than our technique ($\approx$ 30 min).

We expect our motional-averaging NMR method, which outperforms existing thermometry techniques in the gas phase, to open the way to studies of in situ thermodynamics and optimization of gas-solid reactors. The method is robust relative to factors such as pressure, gas composition, reactor type, catalyst type, reaction rate and steady-state conversion. Moreover, its temperature sensitivity is tunable: the stronger the applied gradient, the stronger the dependence on temperature and the higher the sensitivity of the method.

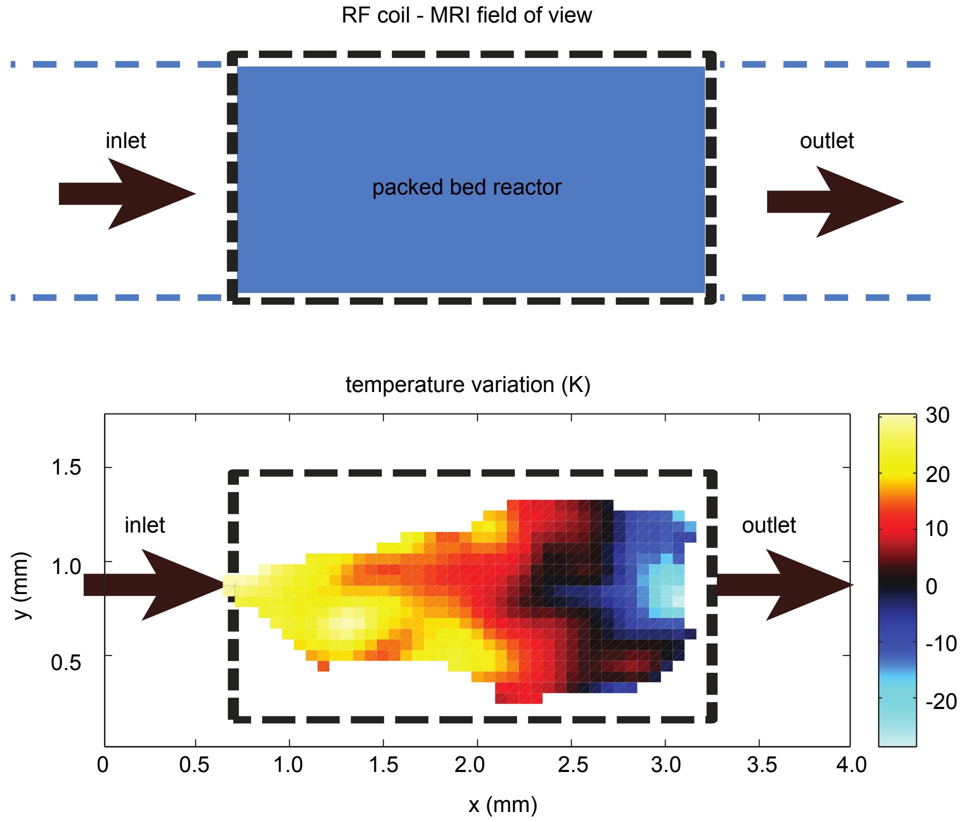

Figure 4.4: Signal enhancement from para-state hydrogen was used to provide detailed views inside the microreactor, which was held at approximately 418 K by using a variable temperature controller to preheat the gas flowing through a heat exchange radio-frequency (RF) coil. a) Schematic view; b) thermal map. The temperature calibration coefficient was 0.200 ± 0.006 Hz/K. The thermal map depicts temperature changes relative to the incoming gas. Spatial distributions of linewidths were mapped on five different reactors prepared similarly. Each reactor exhibited comparable heterogeneity in the temperature distributions.

In practice, the gradient should be significantly stronger than the internal magnetic field inhomogeneities to ensure that the temperature calibration coefficient is essentially sample independent, but it should be weak enough to avoid broadening the lines beyond detection. And because the primary requirement is the presence of NMR-active nuclei in a gas-phase component, the technique will be applicable to most industrially relevant reactions (including those involving mixed gas-liquid-solid phases).

4.2 Supplemental Equations

Random molecular motion has the effect of causing nuclear spins to experience the "average field" more effectively, leading to line narrowing. Motional narrowing effects on the NMR lineshape in inhomogeneous fields were first studied by Bloembergen, Purcell and Pound [117] and later by Kubo [119]. However, the use of motional narrowing effects in an external gradient for thermometry, as is done here, is a novel concept. Here, we present a simple theoretical analysis of the observed effects.

4.2.1 Single component gases

The first case of interest is that of a single molecular species. The NMR signal $s(t)$ from an ensemble of spins initially located at $x(0)$ is proportional to the expectation value [148]:

$$\left\langle \exp\left(i\int_0^t \omega(t')dt'\right)\right\rangle = \exp\left(i\gamma_n g\int_0^t \langle x(t')\rangle dt' - \gamma_n^2 g^2\int_0^t \langle \delta x(t')\delta x(0)\rangle (t-t')dt'\right) \quad (4.4)$$

where $\omega(t) = \gamma_n g\cdot x(t)$ with g the applied gradient, γ_n is the nuclear gyromagnetic ratio and $x(t)$ is the particle position at time t. The equality follows by assuming that $x(t)$ is a wide-sense stationary Gaussian random process. The first term, $i\gamma_n g\int_0^t \langle x(t')\rangle dt'$, is oscillatory and results in a frequency shift similar to the "frequency encoding" step of MRI. Its effect is to report on the morphology of the sample. The second term describes the signal decay, and therefore, the linewidth.

4.2.1.1 Position autocorrelation function

A proper treatment of the position autocorrelation function $\langle x(t)x(0)\rangle$ for self-diffusion of a gas molecule within a fluid of "like molecules" requires kinetic theory, which is beyond the scope of this discussion. In order to keep the present discussion simple and mathematics to a minimum, we used a generalized Langevin description, which we detailed in the previous chapter. The position autocorrelation function is given as:

$$\langle x(t)x(0)\rangle = \frac{kT}{M(\zeta_+ - \zeta_-)}\left[\zeta_+^{-1}\left(1-\frac{\gamma}{m\zeta_+}\right)e^{-\zeta_+ t} - \zeta_-^{-1}\left(1-\frac{\gamma}{m\zeta_-}\right)e^{-\zeta_- t},\right] \quad (4.5)$$

in agreement with Nørrelykke [127]. who used a different method.

There are two cases of interest: $4m = M$ is called "critically damped" and $M > 4m$ is the overdamped case. Both cases are shown in Figure 4.5 below. The "underdamped" case which yields damped oscillatory solutions is discussed in Nørrelykke [127].

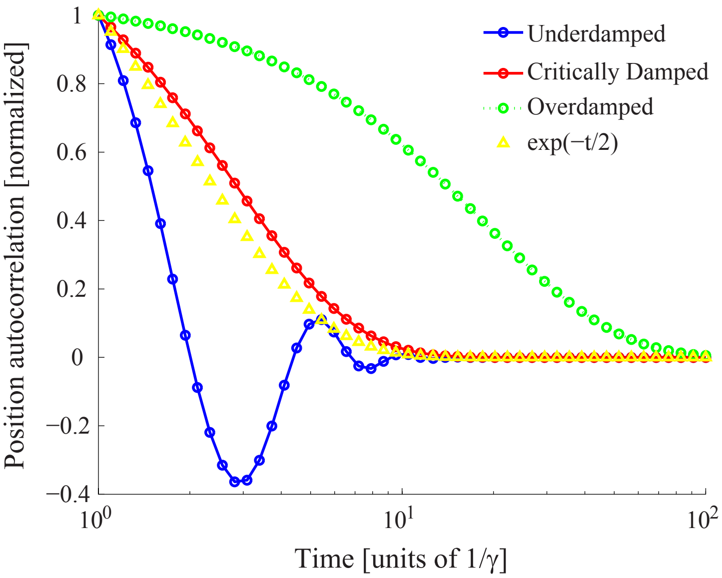

Figure 4.5: Position autocorrelations $\langle x(t)x(0)\rangle/\langle x^2\rangle$ for particle motion driven by viscous thermal noise in the case of overdamped, underdamped and critically damped motion. For reference, the exponential decay $\exp(-t\gamma/2m)$ is shown ($\gamma = 1$, $m = 1$, $kT = 1$).

The Langevin equation is valid in the limit $m/M \to 0$. Standard Brownian motion of large Brownian particles ($M \gg m$) is strongly overdamped. See, for example, the experiment of Huang et al. (2011) [127], who used 1 μm silica particles in water, which corresponds to a mass ratio $M/m \sim 10^{10}$. In our experiments we have $m = M$, which falls outside the range of validity of the Langevin equation. The latter thus provides at best a qualitative description of our experiment — the stochastic force is not likely to be of the correct magnitude if $m = M$. To ensure the validity of the Langevin model we must assume the condition $M \gg m$ ($m/M \to 0$). In [124], the Langevin model with $M/m \sim 10^{10}$ was validated with experimental results at the single particle level.

The temperature dependence of the autocorrelation function is described in the chapter

"Motional averaging of nuclear resonance in a field gradient," and is dependent on the viscosity of the medium. For gases whose viscosity obeys the Sutherland formula, the temperature dependence follows a power law:

$$\Delta f \sim \begin{cases} T^{-7/2}, & T < C \\ T^{-1/2}, & T > C \end{cases} \tag{4.6}$$

in which Δf is the linewidth. Figure 4.2.1.1 shows the temperature dependence of the line broadening for the case of several different gases. In the range 300-600 K, this curve does have some curvature in it. In this study, we chose a linear approximation to this region. Linear approximations are valid over sufficiently small temperature ranges. A polynomial model could also be used for increased accuracy over larger temperature ranges. For thermometry, the only requirement is a monotonic dependence, which is seen from Figure 4.2.1.1 to be the case across all temperatures and pressures of interest (the Sutherland formula is independent of pressure — with errors less than ∼10% up to 3.5 MPa).

4.2.2 Multiple component gas mixtures

Mixture composition enters the picture through the viscosity, which is an average of the two gas mixtures. The viscosity of a mixture comprising n components, η_m, is the summation of partial viscosities of each of the components [6]:

$$\eta_m = \sum_{i=1}^{n} \frac{\eta_i}{1 + \frac{1}{X_i}\sum_{j=1,j\neq i}^{n} X_j \phi_{ij}}, \qquad \phi_{ij} = \frac{\left[1 + \left(\frac{\eta_i}{\eta_j}\right)^{1/2} \left(\frac{M_j}{M_i}\right)^{1/4}\right]^2}{\frac{4}{\sqrt{2}}\left[1 + \frac{M_i}{M_j}\right]^{1/2}}, \tag{4.7}$$

where η_i is the viscosity of the component i, X_i is the mole fraction of component i and M_i is the molecular weight of the i-th component at temperature and pressure of the mixture.

In the limit of low and high T, the denominators in equation 4.7 become independent of temperature. Thus, $\eta_m \sim T^{3/2}$ at low temperatures ($T < C_{min}$) and $\eta_m \sim \sqrt{T}$ at high temperatures ($T < C_{max}$), where C_{min} and C_{max} are the smallest and largest Sutherland

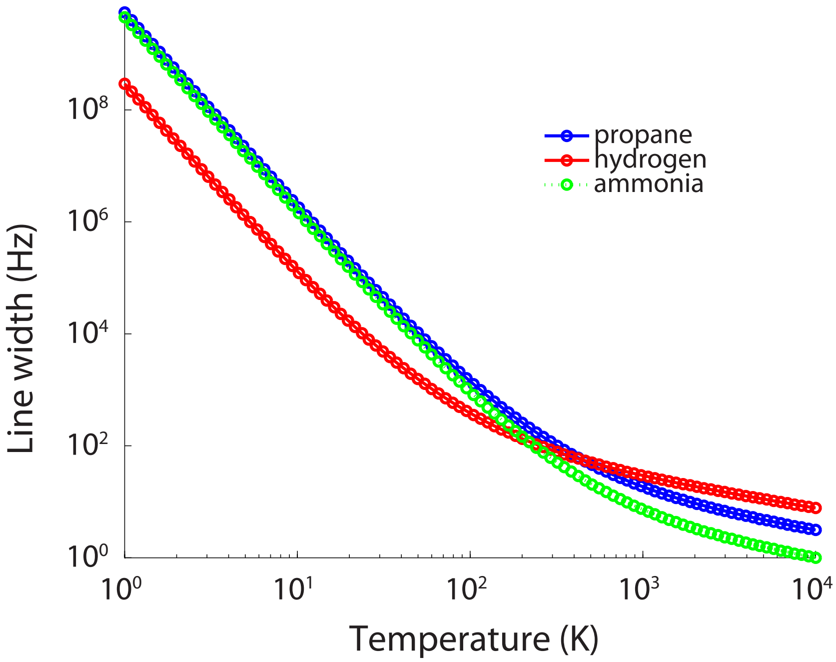

Figure 4.6: Temperature dependence of the NMR line broadening for several different values of the Sutherland constant C. The Sutherland constant separates the two temperature regions $\Delta f \sim T^{-7/2}$ $(T < C)$ and $\Delta f \sim T^{-1/2}$ $(T > C)$. For this calculation, we used $M/m = 10^{10}$, $g = 0.1$ G/cm and $\gamma_n = 2\pi \cdot 42.2 \times 10^6$ rad/s/T.

constants of the mixture components, respectively. This asymptotic behavior for mixtures is identical to the case of single component gases.

In the transition region, the exponent will be a number between 3/2 and 1/2. Thus, the temperature dependence is again monotonic, making it possible to use it as a thermometer. For example, a two-component mixture of, say, (1) propane and (2) ammonia in equal mole proportion would yield $\eta = \frac{\eta_1}{1+\phi_{12}} + \frac{\eta_2}{1+\phi_{21}}$ together with the parameters for propane and ammonia: M_1=17.0 g/mol (ammonia) and M_2=44.1 g/mol (propane), the Sutherland's constant is C=370 K (ammonia) and C=267 K (propane). The resulting line broadening for this mixture is shown in Figure 4.7 and compared to that of the individual components. As can be seen, the curves are all monotonically decreasing functions of temperature and therefore enable temperature measurements with sensitivity which depends on the two components involved.

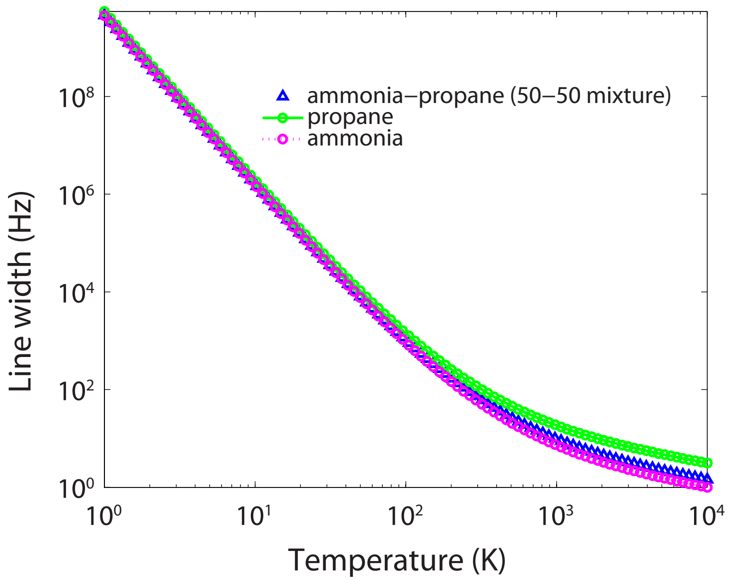

Figure 4.7: Temperature dependence of the NMR linewidth for a gas mixture (50-50) of propane and ammonia. Line broadening for the pure gases of individual components is shown for comparison. For this calculation, we used $M/m = 10^{10}$, $g = 0.1$ G/cm and $\gamma_n = 2\pi \cdot 42.2 \times 10^6$ rad/s/T.

4.2.3 Temperature in heterogeneous media

Our thermometry technique is designed to measure temperature of the gas rather than that of the solid phase because NMR signal from solid materials is generally difficult to observe in this type of experiment. However, in a two-phase medium there is a (potentially) complex interaction between the gas and solid phase. In this section, we examine the effect of the solid phase on gas temperature in a heterogeneous medium. An important question is to what extent the gas phase temperature reflects that of the solid phase as a result of heat transfer processes in some "homogenized limit."

Two examples of porous media are shown in Figure 4.8 below: (a) glass wool and (b) mesoporous aluminum oxide. Glass wool has very high porosity compared to many porous media, meaning that fluid molecules must travel farther to sample the temperature of solid surfaces. In our NMR experiment, the image voxel is typically much larger than the pores themselves. An example is shown by the dotted region in Figure 4.8(c) which comprises a mixture of pore space and solid catalyst. Thus, a proper description of the NMR experiment calls for the use of "volume-averaged" physical quantities. The catalyst medium used in this study resembles the pore space shown in Figure 4.8(a). Analysis of the μ-CT images (Fig. 4.2) yielded the volume fraction of pore space in our experiments in the range of 87-89%. The volume fraction of glass wool is calculated as the ratio of the average intensity of the x-ray image in a region of interest (ROI) over the glass wool divided by the intensity of the glass wall of the NMR tube. The latter corresponds to 100% glass.

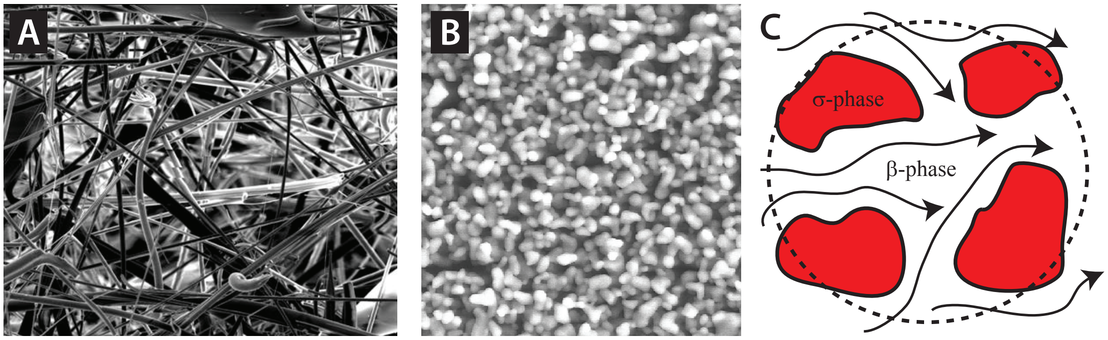

Figure 4.8: Examples of porous media. (a) Glass wool. (b) Metal nanoparticles. (c) Two-phase random medium with σ-phase (solid) and β-phase (fluid). Flow/transport is indicated by the arrows. The dotted circle denotes the averaging volume V.

In two-phase media, the heat transfer process is described in terms of the following equations and boundary conditions [149]:

$$\begin{aligned}
(\rho c_p)_\beta \left[\frac{\partial T_\beta}{\partial t} + \mathbf{v}_\beta \cdot \nabla T_\beta\right] &= \nabla \cdot (k_\beta \nabla T_\beta) && \text{in } \beta\text{-phase} \\
(\rho c_p)_\sigma \frac{\partial T_\sigma}{\partial t} &= \nabla \cdot (k_\sigma \nabla T_\sigma) && \text{in } \sigma\text{-phase} \\
T_\beta &= T_\sigma && \text{at the } \beta - \sigma \text{ interface} \\
\mathbf{n}_{\beta\sigma} \cdot k_\beta \nabla T_\beta &= \mathbf{n}_{\beta\sigma} \cdot k_\sigma \nabla T_\sigma + \Omega && \text{at the } \beta - \sigma \text{ interface.}
\end{aligned} \tag{4.8}$$

$\mathbf{v}_\beta$ is the velocity of the fluid in the β phase. T_i is the temperature of phase $i = \beta, \sigma$. Ω is the thermal energy source or sink due to heterogeneous reactions at the $\beta - \sigma$ interface. $\mathbf{n}_{\beta\sigma}$ is the unit normal to the surface. k_i is the heat conductivity of phase i. $(\rho c_p)_i$ is the volumetric heat capacity of phase i. These equations are of little practical use because of the presence of complex microscopic boundary conditions making the problem intractable. This is often treated with the use of effective-medium theories to upscale the partial differential equations. Two popular methods are "homogenization theory" [150] and "volume averaging" [151].

The method of volume averaging [151], for example, yields the following effective-medium description of the heat transfer process:

$$\langle\rho\rangle C_p \frac{\partial\langle T\rangle}{\partial t} + (\rho c_p)_\beta \nabla\cdot(\phi\langle\mathbf{v}_\beta\rangle^\beta\langle T\rangle) = \nabla\cdot[(\mathbf{K}_{eff}+\mathbf{K}_D)\cdot\nabla\langle T\rangle] + (a_{\beta\sigma}/V)\langle\Omega\rangle_{\beta\sigma}, \qquad (4.9)$$

where ϕ is the volume fraction of the fluid phase, $A_{\beta\sigma}$ is the area per unit volume of the interface, $\langle\Omega\rangle_{\beta\sigma}$ is the area-averaged value of Ω, $\langle\rho\rangle$ represents the spatially averaged density, C_p is the mass fraction weighted heat capacity

$$C_p = \frac{\phi(\rho c_p)_\beta + (1-\phi)(\rho c_p)_\sigma}{\langle\rho\rangle}. \qquad (4.10)$$

$\langle T\rangle$ represents the spatially averaged temperature:

$$\langle T\rangle = \frac{1}{V}\int_V T dV = \phi\langle T_\beta\rangle^\beta + (1-\phi)\langle T_\sigma\rangle^\sigma \qquad (4.11)$$

with

$$\langle T_\beta\rangle = \frac{1}{V}\int_{V_\beta} T_\beta dV, \qquad \text{and} \qquad \langle T_\beta\rangle^\beta = \frac{1}{V_\beta}\int_{V_\beta} T_\beta dV = \phi^{-1}\langle T_\beta\rangle. \qquad (4.12)$$

$\langle T_\beta\rangle^\beta$ is called the phase-averaged temperature. $\mathbf{K}_{eff}$ is the effective thermal conductivity tensor defined by

$$\mathbf{K}_{eff}\cdot\nabla\langle T\rangle = [\phi k_\beta + (1-\phi)k_\sigma]\nabla\langle T\rangle + \frac{k_\beta}{V}\int_{A_{\beta\sigma}} \mathbf{n}_{\beta\sigma}\tilde{T}_\beta dA + \frac{k_\sigma}{V}\int_{A_{\beta\sigma}} \mathbf{n}_{\beta\sigma}\tilde{T}_\sigma dA \qquad (4.13)$$

and $\mathbf{K}_D$ is the thermal dispersion tensor

$$\mathbf{K}_D\cdot\nabla\langle T\rangle = -(\rho c_p)_\beta\langle\tilde{\mathbf{v}}_\beta\hat{T}_\beta\rangle, \qquad (4.14)$$

where

$$\langle T_\beta \rangle^\beta = \langle T \rangle + \hat{T}_\beta, \qquad \mathbf{v} = \langle \mathbf{v}_\beta \rangle^\beta + \tilde{\mathbf{v}}_\beta, \qquad \text{and} \qquad T_\beta = \langle T_\beta \rangle^\beta + \tilde{T}_\beta. \tag{4.15}$$

This model yields a reasonable description of heat transport in a packed bed catalytic reactor. It relies on the assumption of "local thermal equilibrium" [149]. The conditions for validity of the model in relation to the physical length scales are discussed by Whitaker [149]. For steady-state flows, equation 4.9 describes a unique temperature $\langle T \rangle = \langle T_\beta \rangle^\beta = \langle T_\sigma \rangle^\sigma$ whose value is determined by convective, dispersive and diffusive transport relative to the heterogeneous reaction rate at the surface.

In cases where the condition of local thermal equilibrium is not satisfied, a set of two coupled partial differential equations (see Quintard and Whitaker, [152] describes the behavior of the two phase-averaged temperatures $\langle T_\beta \rangle^\beta$ and $\langle T_\sigma \rangle^\sigma$. Only $\langle T_\beta \rangle^\beta$ is reported directly in the NMR experiment. The degree to which the fluid phase temperature, $\langle T_\beta \rangle^\beta$, reflects the value of the solid phase temperature, $\langle T_\sigma \rangle^\sigma$ is determined from equations 7.29 and 7.30 of [152] and the conductive cross-coefficients.

4.3 Control Experiments and Experimental Methods

4.3.1 NMR pulse sequence

The timing for the NMR experiment is illustrated in Figure 4.9. A spin echo with echo time 2τ is followed by acquisition of a free induction decay in the presence of a "temperature-encoding gradient" G_T. The temperature calibration experiment only uses the magnetic field gradient during the acquisition of the echo (G_T). To generate images, pure phase encoding was perfomed using a velocity-compensated phase-encoding gradient G_P. The gradient G_T has a constant amplitude and is independent of G_P. The direction of G_T can be along x, y or z (in which case we denote it as $G_{T,X}$, etc. in Section 4.3.7 below). The sequence is repeated for each phase-encoding step. In this study, we used a two-dimensional 21×21

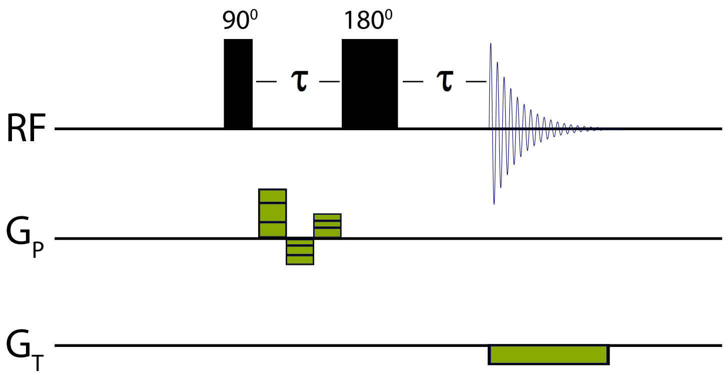

Figure 4.9: NMR pulse sequence for acquisition of thermal maps. Only a single shot (no repetition) is shown. To get a 2D image, this sequence is repeated $n_1 \times n_2$ times while stepping the G_P gradient through the 2D phase encode scheme, where $n_1 \times n_2$ is the number of phase encode steps.

($n_1 \times n_2$) phase-encoding scheme. The G_P gradient shown stands for a two-dimensional phase encode, e.g. G_X and G_Y for an axial image or G_Y and G_Z for a coronal image. In the example shown in Fig. 4.9, RF pulses are hard (non-selective) pulses, the images obtained are parallel projections along the third dimension. Slice-selective pulses could also be used in different embodiments of this experiment. The delay between repetitions ("repetition time" or "recycle time") is 3 s. The total duration of the phase-encode gradient was 3 ms and its maximum amplitude was 5 G/cm. Although not used in this study, the extension to 3D is straightforward and involves using a 3D phase encode sheme instead of a 2D scheme.

4.3.2 Experimental set-up

A schematic of the investigated reactor and experimental setup is depicted in Figure 4.10 below. The reactor, which was placed in the RF sensitive region of the NMR instrument, contains catalyst. The reactor was operated at variable external temperatures between 293 K and 443 K. The internal temperature of the reaction often reached higher temperatures than the external temperature. For the experiments, propylene and hydrogen gases were premixed, and supplied into the reactor at constant flow rate. The tubing is coiled inside the magnet to allow thermal equilibration of the nuclear spins in the magnetic field. The gas mixture enters the reactor at the bottom of the NMR tube, flows through the catalyst-packed region, and leaves through an exhaust line at the top. This down-up flow path is required because of the RF probe design.

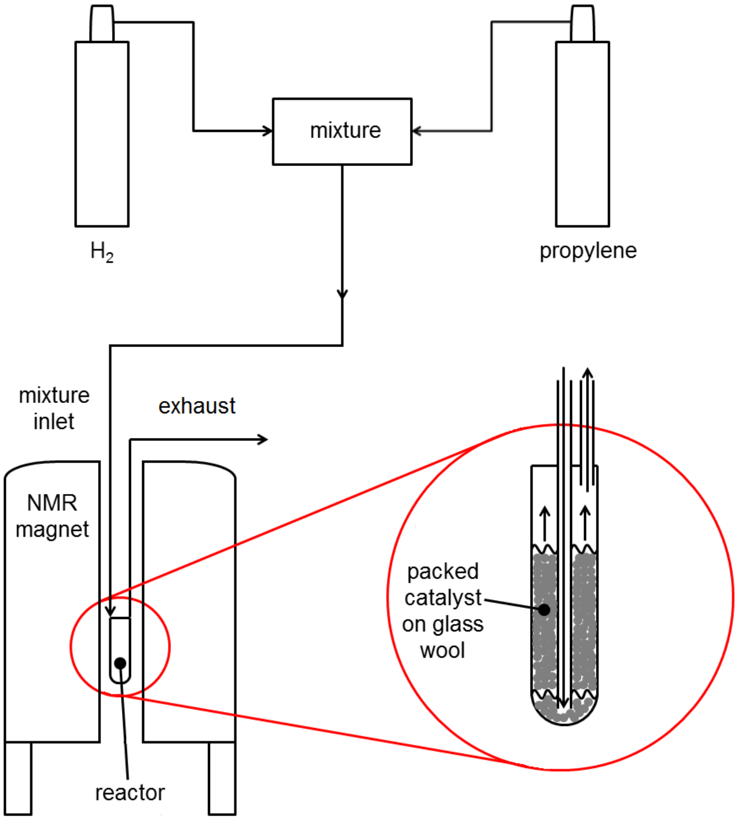

Figure 4.10: Experimental setup for acquistion of thermal maps.

4.3.3 Steady conditions

The reactor systems investigated in this chapter were operated under steady-state conditions. During the course of these experiments, the flow rate was monitored using a flowmeter and observed to remain constant within the uncertainty of the flowmeter. Figure 4.11 shows that the ^{1}H NMR spectrum remains constant over a period of more than 5 hours, with constant catalytic conversion. After 5 hours, the reaction shows no sign of reduced yield.

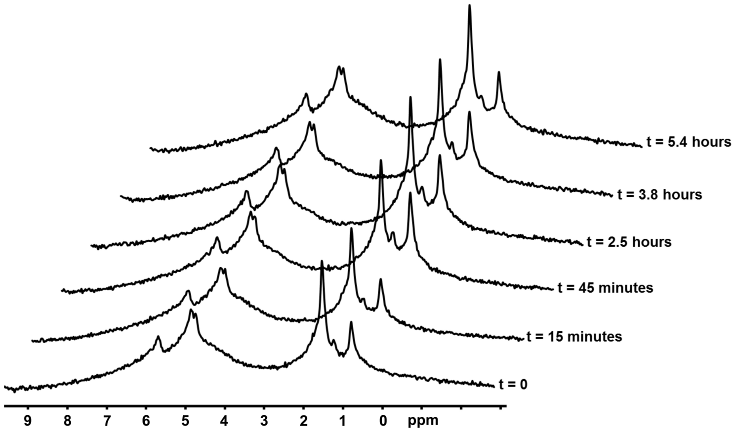

Figure 4.11: NMR spectrum of the hydrogenation reaction catalyzed by Pd-MOF in a 10 mm reactor. The reaction was monitored for several hours and exhibits a constant conversion rate over time.

The temperatures during the reaction can also be shown to be in the steady state. Figure 4.12 depicts thermal maps of the *in situ* hydrogenation reaction acquired immediately after catalyst activation (time $= 0$), after 1 hour, and after 4 hours. While spatial gradients are present (as expected), the temporal fluctuations are small. In Section 4.3.12.2 we discuss the effects of spatial gradients on the lineshape.

4.3.4 Image voxel geometry

Because the phase encoding scheme used in the data acquisition was two dimensional and the pulses are hard pulses (see Figure 4.9), the images produced in this experiment are “parallel projections”, meaning that the geometry of each voxel reflects the shape of the NMR tube. This explains, for example, why the coronal and sagittal images of Figure 4.3 are brighter in the center and weaker at the edges of the NMR tube. On the other hand, the signal drop-off near the top and bottom edges of the field of view is due to the drop in sensitivity of the RF coil, not because of the shape of the NMR tube. The shape of a NMR image voxel in this experiment is shown in Figure 4.13 below.

The RF pulse used is non-selective, which implies that the MRI images are projections

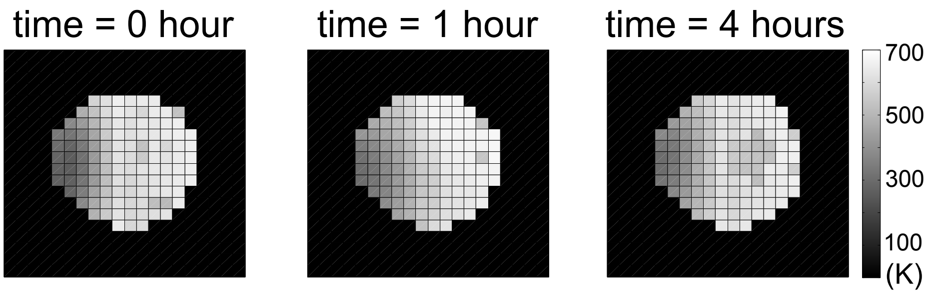

Figure 4.12: Temporal stability of thermal maps during the reaction. The hydrogenation reaction was catalyzed by Pd-MOF in a 5 mm reactor. Over the course of several hours, the reaction demonstrates constant conversion rate over time (Figure 4.11) as well as stable temperatures, as shown here.

across the cylindrical-shaped reactor. The NMR signal in a pixel is therefore averaged across the reactor thickness, which ranges from 0 to 8 mm when going from the reactor's edge to its center. We note that since the NMR signal is a projection across the thickness of the reactor, temperatures cannot easily be compared between the different projections since their respective pixels represent averages performed across different directions.

4.3.5 Field-of-view alignment

In order to know the position of the fiber-optic sensors in the MRI image, the field-of-view (FOV) was aligned relative to the physical coordinates by placing water-filled glass tubes at different positions within the FOV following by the acquisition of MRI scans. The positions of the glass tubes were measured using a caliper, with precision better than 100 μm. When dealing with coronal vs sagittal projections, we used the manufacturer-specified directions for x and y, as marked on the gradient stack, for alignment purposes. We estimate the accuracy of this alignment procedure to be better than 0.5 mm in all directions.

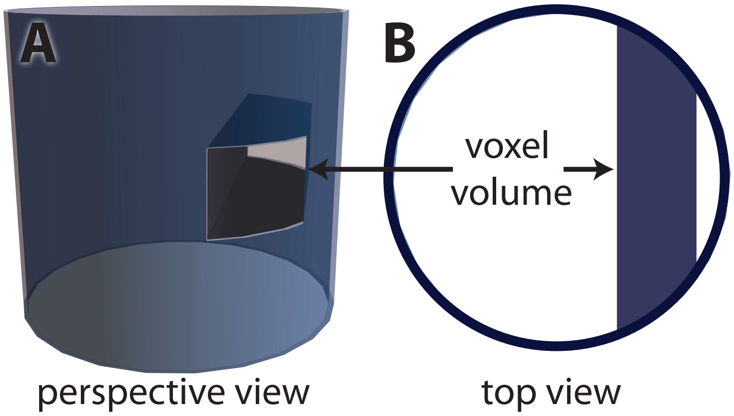

Figure 4.13: Geometry of the image voxel. (a) 3D perspective view of a voxel from a coronal or sagittal projection in relation to the NMR tube. (Only a short section of the NMR tube is shown.) (b) 2D top view. The size of the voxel relative to the NMR tube is exaggerated for illustration purposes. Roughly speaking, the shape of the gas volume giving rise to NMR signal within a voxel is that of a horizontally-aligned parallepiped intersected with a vertical cylinder.

4.3.6 Fiber-optic probe geometry

The tip of the fiber-optic sensor has an external diameter of approximately 1 mm, which is on the order of the size of a voxel (in-plane dimension). However, along the third dimension where the voxel is projected, the ratio of the sensor volume to the voxel depth varies from point to point along the width of the NMR tube (as can be inferred from the diagram of Figure 4.13). When the probes are placed near the wall of the NMR tube, approximately 80% of the voxel volume is occupied by the fiber-optic sensor. When the probes are placed near the center of the tube, this ratio is approximately 40%. The NMR-derived temperature readout in our experiments is an average along the depth of each voxel.

4.3.7 Effect of gradient direction

A simple but important control experiment consists of verifying that the thermal maps are independent of the choice of gradient direction. Otherwise, any discrepancy arising from the choice of gradient direction would be a source of error in the derived temperature measurement. The control experiments were performed on a 14 T Bruker AV 600 MHz system. A 5-mm NMR tube with J. Young valve was filled with 45 PSI propylene and inserted into the magnet. Axial images were acquired at 5 different temperatures (305 K, 316 K, 326 K, 337 K and 346 K) after equilibration to promote spatially uniform temperatures. In total, 441 ($n_1 \times n_2$=21×21) phase encoding steps were performed with gradients in x and y direction of 2 G/cm maximal strength (G_P gradient shown in Fig. 4.9). The gradient time for velocity-compensated phase-encoding was set to 3 ms and the echo time to 26 ms. At each temperature two images were recorded with either a temperature encoding gradient in x- or y-direction (0.1 G/cm) switched on during the data acquisition to introduce a line broadening (G_T gradient shown in Fig. 4.9). The thermal maps are shown in Figure 4.14 and are in good agreement at each target temperature, with variation in a single thermal map within ± 2 K. The discrepancies that result from choice of gradient direction are less than 4%. Each pixel corresponds to a region of approximately 0.27×0.27 mm^2, whereas the depth is determined by the sensitivity of the RF coil region along the z direction and is approximately 5 mm.

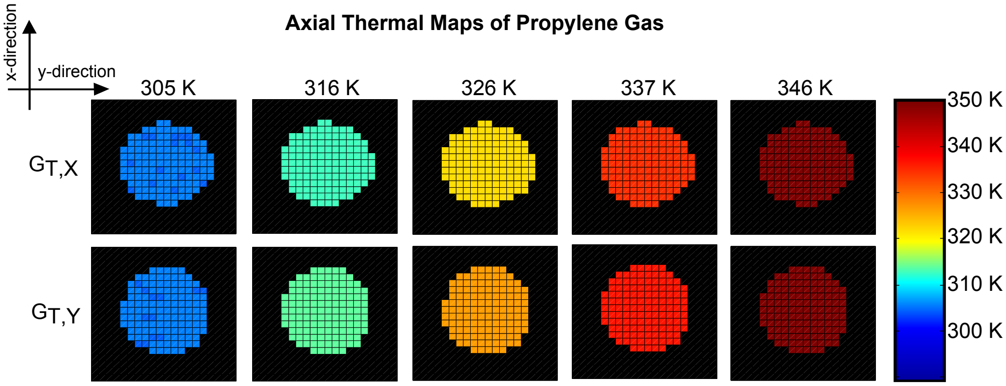

Figure 4.14: Thermal maps acquired using x versus y gradients yield similar results within 4% error. The upper row corresponds to axial images acquired with a temperature gradient along the x-direction, and the lower row corresponds to axial images acquired with a temperature gradient along the y-direction.

4.3.8 Effects of reaction rate

Another possible mechanism for temperature-dependent line broadening is the timescale of the chemical reaction. If the reaction proceeds rapidly, the short lifetime of a chemical species may lead to temperature-dependent broadening because the rates of chemical reactions generally follow an Arrhenius-type law. If the NMR resonance of one of the reactants is used to measure temperature, this resonance may undergo "lifetime-broadening" as the reactants are converted into products.

Here, we show that for the reaction studied in this work, reaction rates do not lead to significant broadening. This can be done by estimating the average time scale of the chemical reaction $aA + bB \rightarrow cC$ in the presence of transport using the advection-diffusion equation (conservation of mass species):

$$\rho \partial_t y_j + \rho v \cdot \nabla y_j + \mathrm{div} \mathcal{F}_j = m_j \dot{\omega}_j, \tag{4.16}$$

where ρ is the gas density, m_j is the molar mass of species j, v is the velocity, $y_j = m_j [J]/\rho$, and $\mathcal{F}_j = -\rho D_j \nabla y_j$. D_j is the diffusion constant of species j, and $[J]$ is the concentration of species j. In the case of first-order rate reactions, $-\dot{\omega}_A = -\dot{\omega}_B = \dot{\omega}_C = k[A][B]$, where k is the rate constant of the reaction. For steady flows, $\partial_t y_j = 0$. Setting $j = C$ yields one such equation

$$k[A][B] = v \cdot \nabla[C] - D_C \nabla^2 [C], \tag{4.17}$$

where $\nabla^2[C]$ denotes the Laplacian of the concentration field $[C]$. The time scale of the reaction is $k[B]$. Estimates of this quantity can be obtained from a concentration map of the species of interest, such as the one shown in Figure 4.15, which was extracted from the NMR data set and normalized using knowledge of the gas mixture composition and measured pressures at the inlet. With this normalization, the area under the curves of spatially-resolved NMR spectra during the reaction then provides a map of concentrations.

The gradient and Laplacian were computed by finite differences using the built-in MAT-

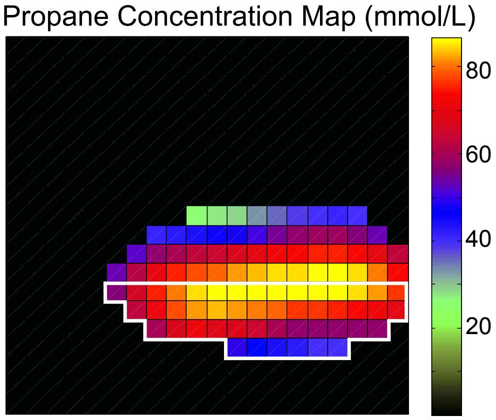

Figure 4.15: Concentration map of propane (reaction product) in the YZ plane of the catalytic reactor using MOF catalyst. Together with knowledge of the flow velocity, this map yields convective and diffusive transport contributions to the conservation of mass species, from which we obtain the reaction rates. The reaction rates are averaged in a region of interest (ROI) over the heterogeneous medium (example ROI shown in white) to yield the average timescale of the reaction.

LAB commands `gradient` and `del2`, respectively. The step size in computing the gradient and the Laplacian of the concentration field was 0.73 mm, which is both the width and height of a single voxel. Using the average flow speed in the reactor as measured by a flowmeter placed in the flow line ($\overline{v} = 0.75$ m/s), the average reaction time constant is found to be (1.4±0.2) Hz.

Thus, line broadening due to the chemical reaction is less than 2 Hz in our experiments, and is therefore negligible compared to the intrinsic linewidth of the gas substances in the absence of a reaction. We note that different reactions and transport conditions may lead to different outcomes.

There are at least two ways to circumvent rate-induced broadening:

1. by applying a stronger gradient,
2. by monitoring the resonance from product molecules instead of a reactant.

In the second case, product molecules are stable and their resonances do not undergo lifetime broadening.

In the event that a reactant molecule (as opposed to a product molecule) must be used for thermometry and stronger gradients are not possible[1], accurate thermal maps in the presence of rate-induced broadening may still be possible if the reactor is sufficiently homogeneous and the overall temperature dependence of the linewidth is monotonic.

4.3.9 Temperature coefficients of single component gases

Here, the main properties of gas-phase thermometry in a single component gas are investigated using propylene gas by performing temperature calibration experiments at 1.0 atm for seven different gradient strengths. As gradient strength is increased, the linewidth dependence on temperature increases. The results are summarized in Table 4.9.

The experimental errors in Table 4.9 were determined from repeated measurements at each gradient strength on newly prepared samples. We note that these error bars (less than 11%) are different from reactor to reactor; this error is unrelated to the 4% error bar previously quoted, which is the uncertainty of localized temperature measurements performed within the same reactor. Many catalytic processes operate at high temperatures and high pressures. While the temperatures sampled in our thermal maps exceed 600 K, the method should also work at higher temperatures, as discussed above. Operation at higher pressures should also be possible based on the same theoretical arguments. Here, we show that the method works at higher pressures, and is independent of pressure up to 5 atm (as high as was allowed by our J. Young valve tubes).

Temperature calibration curves were obtained for propylene gas at two additional pressures: 3.1 and 5.1 atm. For three different applied gradient strengths, the temperature coefficients were similar within experimental error (Table 4.5). At zero applied gradient, linewidth dependence on temperature was negligible. For nonzero applied gradients, the

---

[1] While gradient amplitudes used in this experiment are rather modest and not limited by the available hardware, sufficiently strong gradients will eventually lead to overlap of the spectral lines and, ultimately, to the complete loss of signal.

Applied gradient strength (mG/cm)	Temperature coefficient (Hz/K)
0.0	-0.01 ± 0.01
2.7	-0.11 ± 0.01
5.3	-0.12 ± 0.01
10.6	-0.18 ± 0.02
15.9	-0.20 ± 0.01
21.2	-0.26 ± 0.01
26.5	-0.28 ± 0.03

Table 4.1: Temperature coefficients for propylene at different applied gradient strengths. Pressure is 1.0 atm.

temperature coefficient increased with increasing gradient strength. In all cases, the results are independent of pressure within ± 11% of each other and exhibit no clear trends. The residual differences are likely due to different shimming conditions between experiments.

	Temperature coefficient (Hz/K) at different applied gradient strengths		
Pressure (atm)	0.0 mG/cm	5.3 mG/cm	26.5 mG/cm
1.0	-0.01	-0.12	-0.28
3.1	-0.01	-0.12	-0.28
5.1	-0.01	-0.13	-0.26

Table 4.2: Temperature coefficients for three pressures of propylene. Typical error associated with these measurements is ± 0.01 Hz/K for the 0.0 mG/cm and 5.3 mG/cm systems, and 0.03 Hz/K for the 26.5 mG/cm system.

4.3.10 Temperature coefficients of gas mixtures

As mentioned earlier in Section 4.2.2, mixture composition enters through the viscosity, which is an average of the two gas mixtures. When the ratio of components is altered, the viscosity shifts toward one or the other. In this section, we show that the effect on the temperature calibration coefficient is small. In practice, if one uses the same NMR resonance and molecular species as the NMR signal to yield thermal maps, the calibration coefficient does not change appreciably across mixture composition.

Consider a mixture of propylene and ethane (Table 4.3). As demonstrated in Table 4.2, the linewidth exhibits negligible temperature dependence in the absence of an external gradient. For propylene and ethane ^{1}H resonances, these linewidths were approximately 14 Hz and 3 Hz, respectively. With the application of an external field gradient, the temperature dependence of linewidth is independent of the component ratio (within experimental error), as seen in Tables 4.3 and 4.2.

Additionally, the temperature coefficients of propylene and ethane gases are identical within experimental error. As gradient strength increases, the linewidth becomes increasingly dependent on temperature, as expected. These results suggest that the temperature coefficient may exhibit considerable independence from gas type and mixture composition. The error bars were derived from repeated measurements on different sample preparations and are likely due to differences in shimming.

4.3.11 Temperature coefficients in heterogeneous media

In order to investigate the possibility of dependence on the reactor composition, we have investigated several different reactor types in addition to the glass wool reactors described in the main text of this chapter. Packed-bed reactors containing the following catalysts were constructed: silica gel, ZIF-8 (Basolite), and Pd-MOF (Table 4.4 and Figure 4.16). In all cases, the reactors were packed with pure catalyst and no glass wool. This type of reactor mimics conditions which are found in a variety of processes. The reactors are shown in Figure 4.16.

Temperature coefficient (Hz/K) at different applied gradient strengths			
propylene/ethane (2/3) mixture			
Gas	0.0 mG/cm	5.3 mG/cm	10.6 mG/cm
Propylene	0.00	-0.15	-0.16
Ethane	0.01	-0.14	-0.16
propylene/ethane (1/14) mixture			
Gas	0.0 mG/cm	5.3 mG/cm	10.6 mG/cm
Propylene	0.00	-0.13	-0.18
Ethane	-0.01	-0.13	-0.15

Table 4.3: Temperature coefficients for propylene/ethane mixtures. Typical error associated with these measurements is ± 0.01 Hz/K for the 0.0 mG/cm and 5.3 mG/cm systems and ± 0.02 Hz/K for the 10.6 mG/cm system. Ratios given (2/3 and 1/14) are ratios of gas pressures. Total pressure of the mixtures in each tube was 2.0 atm.

As each of the calibrations correspond to different experiments, initial shims, and therefore, initial linewidths, were quite varied among the three systems. However, the effect of applied magnetic field gradient becomes clear when the linewidths are sufficiently broadened to overwhelm the heterogeneous nature of the packed bed systems. In Table 4.4 we show the results in the case of strong applied gradients (25.6 and 52.0 mG/cm). As can be seen, the temperature coefficient is independent of the reactor type within experimental error. The errors are consistent with differences in shimming, which are additive to the external gradient.

Temperature coefficient (Hz/K) at different applied gradient strengths			
Media	0.0 mG/cm	26.5 mG/cm	53.0 mG/cm
Silica Gel	-0.01	-0.31	-0.92
ZIF-8 (Basolite)	-0.03	-0.29	-0.86
Pd-MOF	-0.01	-0.26	-0.84

Table 4.4: Temperature coefficients for various types of packed-bed catalytic reactors. The typical error bar associated with these measurements on heterogeneous media is ± 0.01 Hz/K, ± 0.03 Hz/K and ± 0.09 Hz/K for the 0.0 mG/cm, 26.5 mG/cm, and 53.0 mG/cm systems, respectively. Pressures of each system were approximately 2.7 atm.

4.3.12 Origin of the inhomogeneous lineshape in heterogeneous media

Inhomogeneity effects on temperature coefficient

Equations 4.1 and 4.2 give temperature coefficients of -0.16 Hz/K and -0.10 Hz/K (± 0.01 Hz/K) for the PtNP and Pd-MOF systems, respectively. These values differ from one another by at least 26% using the edges of the error bars. The spin-spin relaxation time, T_2, of pure propylene was measured to be (68 ± 11) ms using a Carr-Purcell-Meiboom-Gill (CPMG) echo train sequence of 100 echoes with an echo spacing $\tau = 10$ ms. The final observed linewidth in the presence of the external gradient was approximately 90 Hz. Of

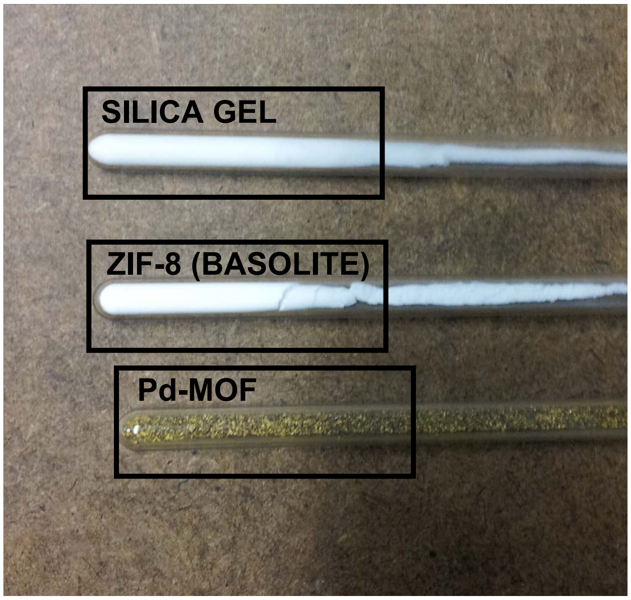

Figure 4.16: Packed bed reactors containing silica gel, ZIF-8, and Pd-MOF. The RF region of each reactor is boxed.

this, 5 Hz are due to contributions from T_2, which is essentially temperature independent over the range studied. This leaves about 85 Hz caused by field gradients, which will give rise to temperature-dependent effects. The gradients are the sum of the applied (external) gradient and shims.

In the absence of an applied gradient (G_T) the NMR linewidth averaged over the entire PtNP reactor volume was 41 Hz for this particular reactor. Under the same conditions, the average NMR linewidth over the entire Pd-MOF system was 31 Hz. The contribution from residual field inhomogeneities, $(\pi T_2^{\dagger})^{-1}$, can be estimated from knowledge of T_2 and the measured linewidth in the absence of a gradient, $(\pi T_2^{*})^{-1}$ using Eq. (4.18),

$$\frac{1}{\pi {T_2}^{*}}[Hz] = \frac{1}{\pi T_2}[Hz] + \frac{1}{\pi {T_2}^{\dagger}}[Hz]. \tag{4.18}$$

This yields $(\pi T_2^{\dagger})^{-1} = 36$ Hz and 26 Hz for the PtNP and Pd-MOF systems, respectively. These figures represent a substantial fraction (nearly one-third to one-half) of the 85 Hz contribution to the linewidth from all field inhomogeneities. Thus, differences in residual shim can likely explain the differences in observed temperature calibration coefficients. A more exact comparison is not available due to the substantial complications associated with measuring T_2 in a gas and the lack of knowledge of the exact nature of the residual shims (spatial pattern and direction).

4.3.12.1 Linewidth over a single voxel

For the method to yield measurements that are independent of the reactor medium, it is important that the external gradient overwhelms the linewidth in the region of interest. Thus, it is instructive to examine the line broadening effect from the external gradient and compare it to the local linewidth in the absence of a gradient. We have seen above that the linewidth over the entire reactor was broadened by a factor of five (5) or greater. At the level of a single voxel, the external gradient must overwhelm the linewidth as well.

The local linewidth can be mapped with an MRI experiment by using spatial encoding, with and without the "temperature-encoding gradient," G_T. Figure 4.17 depicts an axial view of the PtNP reactor's propylene density. When the NMR experiment is performed on the reactor, without the gradient G_T, propylene's methyl resonance yields a voxel linewidth Δf of 17 Hz. However, when the NMR experiment is performed during a catalytic reaction, and with the applied gradient G_T, the linewidth broadens significantly within a voxel. As shown in Figure 4.17(b), the propylene and propane resonances overlap, so it is necessary to fit the data to a sum of Lorentzians. Doing this yields broadened resonances with linewidths up to 90 Hz as compared to 17 Hz without the gradient. Thus, the gradient-induced line broadening at the single-voxel level is approximately five-fold. The line broadening over a single voxel is nearly identical to that over the entire reactor volume.

4.3.12.2 Lineshape over a single voxel

In the general case, the voxel lineshape depends on the magnitude of the temperature gradients contained within a voxel. For exceedingly large gradients the signal is best described by a stretched exponential (Kohlrausch) function, which models sums of exponentials. The effective linewidth is the weighted mean of the individual contributing linewidths, and the

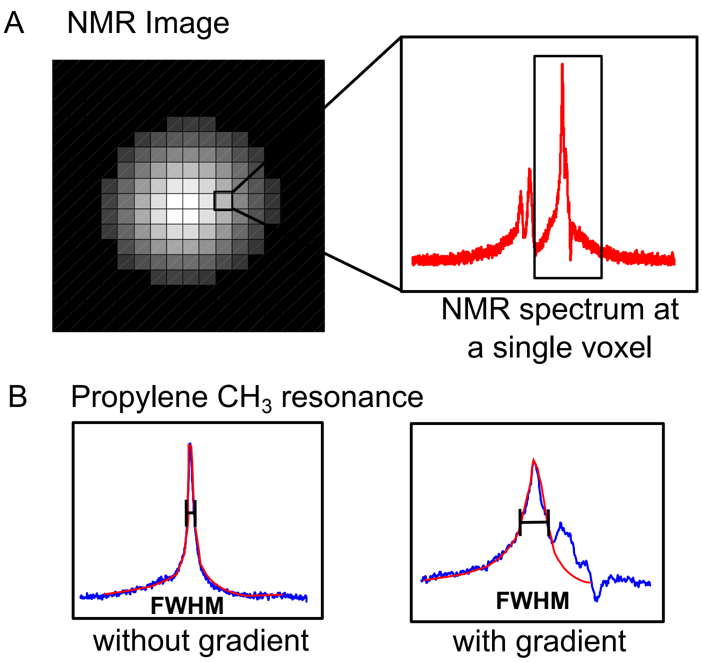

Figure 4.17: (a) Spectroscopic imaging produces a gas density image of the PtNP reactor system, in which each voxel contains its own NMR spectrum. Voxel size is approximately 0.7×0.7 mm^2. (b) At each voxel, linewidth Δf is determined by the full width at half maximum (FWHM) of a resonance. In the presence of applied magnetic field gradient G_T, the FWHM of the methyl resonance is broadened by a factor of 5. Here we compare the linewidth prior to reaction and without gradient G_T to the linewidth during a reaction with an applied gradient G_T.

"width" of the distribution is encoded in the stretched exponent [153].

In our experiments, however, these gradients are quite small on the absolute temperature scale. The maximum "fractional" temperature change from voxel to voxel was found to be less than 4% on average, as shown in Figure 4.18. Furthermore, all spectral data were well described by Lorentzian lines, which is further evidence that the temperature gradients within voxels are not a problem.

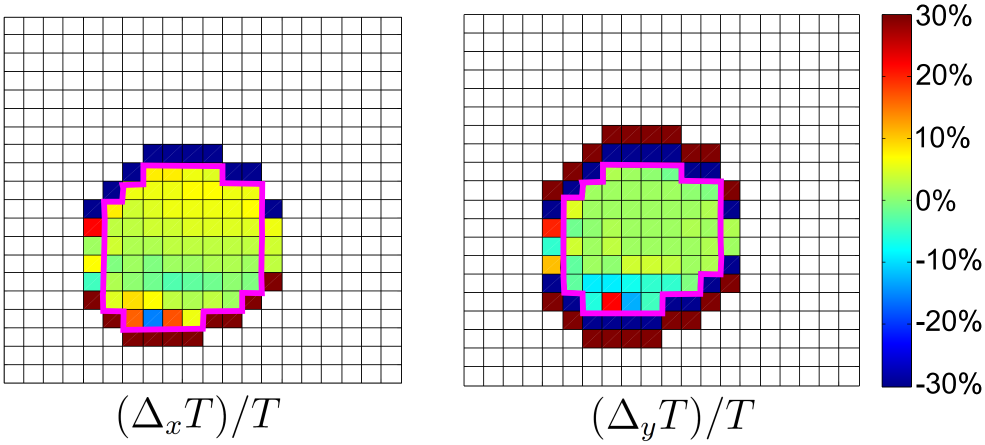

Figure 4.18: Maps of the finite differences in temperatures between nearest-neighbor points relative to the local temperature: $(\Delta_x T)/T$ and $(\Delta_y T)/T$. These maps represent the differences in temperature between neighboring voxels (along x or y). For temperature profiles which are monotonic across a voxel, this finite difference provides an "upper bound" for the magnitude of the temperature gradient within a voxel. As can be seen, these internal gradients over a voxel are fairly small on average ($< 4\%$). Points near or at the edges are unphysical due to the large derivatives at the boundaries.

4.3.12.3 Thermal flux and catalyst packing

In a catalytic reactor the transport of heat is of prime importance. The dynamic quantity of interest is the flux of energy (e.g. internal energy or enthalpy of the system), which is proportional to the local temperature gradient $\|\nabla T\|$. The temperature gradient can be estimated numerically from the thermal maps using finite differences (Figure 4.19). When compared to a μ-CT scan of the microreactor, we notice that the length scales of energy flux are similar to those of the glass wool/catalyst packing. The μ-CT images shown below are of a typical PtNP reactor packed with glass wool. The CT scan represents a 1 mm-thick slice through the middle of the reactor, wheras the MRI images (Figure 4.3) are projections along the thickness of the reactor. We note that, although the reactor construction process is identical, the reactor shown in the μ-CT image is not necessarily the same reactor as that shown in the MRI image and the images are not co-registered. Our statement only refers to the typical length scales found in such reactors.

4.3.13 PtNP catalyst preparation

The synthesis of PtNP follows the reported protocols [147]. The supported heterogeneous catalyst used in reaction imaging was made by soaking a piece of glass wool (SiO_2) in an aqueous dispersion of p-mercaptobenzoic-capped, 2.5±0.4 nm PtNP to yield 1-wt% Pt/SiO_2.

4.3.14 Pd-MOF catalyst preparation

MTV-MOF-AB was prepared in accordance with reported procedures [154]. The free amine ($-NH_2$) was metallated with palladium by post-modification to give Pd-MOF [155]. The Pd-MOF catalyst was then mixed with TiO_2 nanopowder and packed with glass wool to obtain the supported heterogeneous catalyst used in reaction imaging.

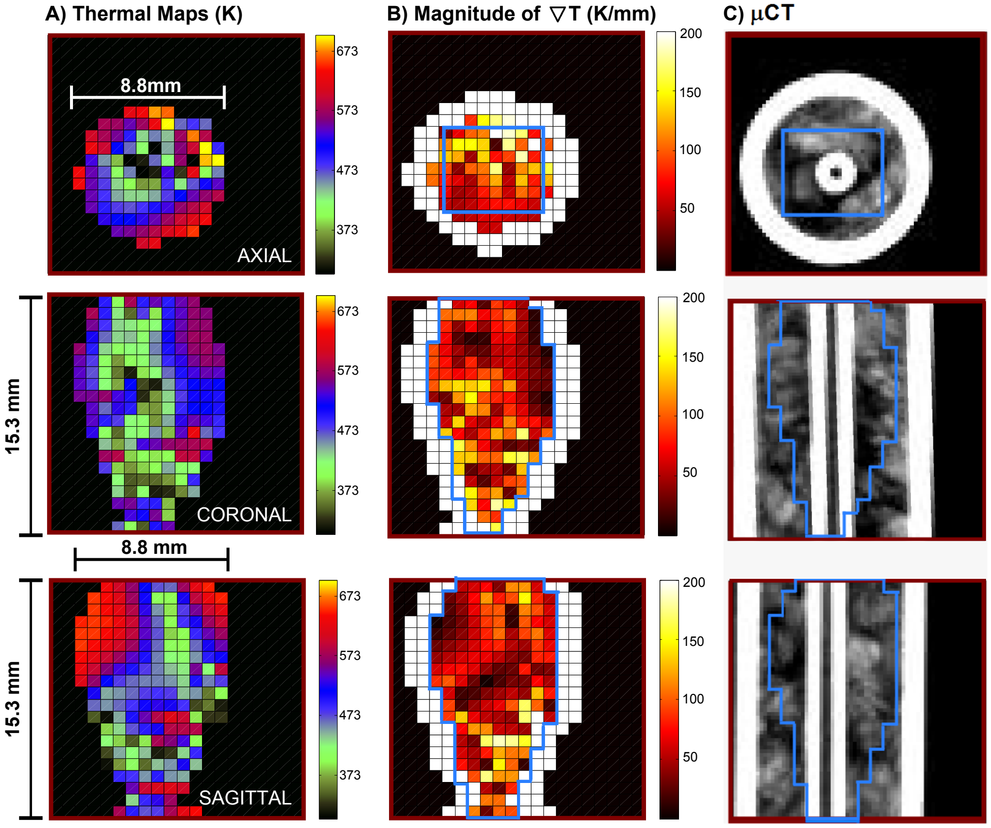

Figure 4.19: Typical length scales in a PtNP reactor system. (a) Thermal maps of of the PtNP reactor system. (b) Magnitude of ∇T, the numerical gradient of temperature across the PtNP reactor. (c) μ-CT images of NMR reactor.

4.3.15 Calibration of motional-averaging technique

A 10-mm NMR tube was packed with catalyst-loaded glass wool. For flowing propylene gas (40 PSI, 15 cc/min), an FID was acquired between 303 and 413 K in steps of 10 K. A spin-echo pulse sequence was used, and a magnetic field gradient was applied during acquisition. Spectral windows were fitted to a sum of Lorentzian curves with MATLAB, using nonlinear least-squares regression. The temperature reported is that of the gaseous component contributing to the NMR signal, which is in local equilibrium with the solid phase.

4.3.16 Temperature mapping

Propylene gas (40 PSI, 15 cc/min) and para-state hydrogen gas (40 PSI, 15 cc/min) were flowed through the system. Each image was acquired using a spin-echo imaging pulse sequence with 441 transients during a continuous flow reaction for a total acquisition time of 33 min. The scan time, during which images are made from a steady-state flow, could be further reduced by compressed sensing. The spectrum of each pixel with SNR > 4 was analyzed in MATLAB, using nonlinear least-squares regression to fit the propane and propylene resonances to a sum of Lorentzian curves. The reactors we investigated featured voxel linewidths in the range 40-300 Hz, depending on the catalyst type and support. The temperature measurement was confirmed using a FISO FOT-L sensor. The spatial resolution of the experiment is limited by the SNR of the image, as in conventional MRI experiments. For higher spatial resolutions (smaller voxels), the applied gradient can be even weaker. This is because the gradient needs to be only about 5-10 times larger than the linewidth over the voxel in the absence of a gradient.

4.3.17 T_1 relaxometry

A 10-mm NMR tube with a J. Young valve adaptor was pressurized to 15 PSI with propylene gas. An inversion-recovery pulse sequence with 51 inversion times was applied, and relaxation time was determined by fitting the data to a nonlinear least-squares exponential recovery curve in MATLAB. T_1 was determined between 303 and 413 K in steps of 10 K.

4.3.18 T_2 relaxometry

A 10-mm NMR tube with a J. Young valve adaptor was pressurized to 15 PSI with propylene gas. A single-shot Carr-Purcell-Meiboom-Gill echo train of 100 echoes was applied for interpulse spacing between 1 and 20 ms. Relaxation time was determined by fitting the amplitude of alternating echoes to a nonlinear least-squares exponential decay curve in MATLAB. T_2 was determined between 303 and 413 K in steps of 10 K.

4.3.19 Microreactor imaging

The catalyst, Wilkinson's catalyst supported on silica gel, and the microreactor were prepared as described in [156]. Polarization induced by para-state hydrogen (mixture contains hydrogen enriched to 50% para-state hydrogen), was used to provide signal enhancement from the microreaction. The calibration and data analysis were similar to that described above.

CHAPTER 5

Concluding Remarks

The research demonstrated in this dissertation investigates the motional averaging behavior of gases in a magnetic field gradient. This motional averaging behavior is exploited to develop a new gas-phase thermometry method, which is utilized to spatially resolve temperatures of gases in a chemically-reacting flow for the first time.

Diffusion NMR methods have been the flagship experiment to measure molecular self-diffusion phenomena in a variety of free or confined geometries. The importance of this experiment cannot be overstated, with its impact ranging from fundamental physics to applications (hyperpolarized gas MRI, study of porous media, diffusion of membrane proteins, diffusion tensor imaging). Surprisingly, an important detail appears to have been overlooked which manifests itself when examining more closely the temperature dependence of the linewidth. In chapter 2 of this dissertation, the difference between gases and liquids is demonstrated in the temperature dependence of the NMR linewidth, which follows different power laws. An additional effect introduced by the non-Fickian motional averaging is the appearance of a t^1 time dependence in the case of gases (as opposed to t^3 for liquids). A natural way to probe this t^1 law is to study the signal decay in a CPMG experiment. CPMG has been utilized since the 1950s to measure nuclear-spin transverse (T_2) relaxation times. In the presence of magnetic-field inhomogeneities, the limit of short interpulse spacings yields the intrinsic T_2 time by mitigating the diffusion-induced inhomogeneous broadening. The intrinsic T_2 time reveals important information about the sample microstructure and composition. This method is widely used in biomedical imaging and porous media studies to characterize various tissues or materials based on the underlying structure or architecture. Even in the gas-phase such experiments are of great value in the study of lung physiology and in fundamental atomic physics studies of spin-exchange optical pumping. However, this t^1 time dependence has never been accounted for so far, and this could potentially compromise such experiments and their interpretation in terms of the underlying physics. In chapter 3, we demonstrate for the first time that this t^1 law holds for gases in experiments, whereas liquids follow t^3. These two puzzle pieces unambiguously prove the validity of our revised theory of NMR motional averaging. In chapter 4, we utilize this phenomena to develop a useful technique for thermal mapping of gases during chemical reactions.

We expect this work to be of broad interest to the community, especially to researchers carrying out fundamental studies in physics, chemistry, chemical engineering, and in biomedicine. We anticipate an impact in medical imaging since MRI makes use of field gradients to encode frequency. In principle, any MRI experiment that attempts to minimize, control or probe diffusion effects could be affected if they involve gases, such as hyperpolarized gas phase lung imaging [157–159] or diffusion tensor imaging experiments [160]. This work also has implications for quantum information; namely, in the design of optimal dynamic decoupling sequences. Uhrig demonstrated that the efficiency of dynamic decoupling sequences could be drastically improved by choosing random time intervals (as opposed to fixed time intervals) between time-reversal pulses [131]. However, in gases the efficiency of such dynamic decoupling sequences is now fundamentally limited by a lower bound arising from non-Fickian diffusion.

APPENDIX A

Pulse Sequences

A.1 Bruker Pulse Sequences

In Bruker pulse sequences, all comments are preceded by a semicolon (;).

A.1.1 Spectroscopy Sequences

A.1.1.1 cpmg_train.nnj

This pulse sequence is a CPMG echotrain experiment that acquires the full echo envelope. Used for measuring T_2 relaxation times. There are multiple versions of the echotrain experiment with different phase cycling, as well as a version with a gradient on, which was used in Chapter 2.

```
; NOW INCLUDES COMPOSITE PULSES FOR 180 with correct timing
#include <Avance.incl>
#include <De.incl>
define delay dwdel1
define delay dtau

"p2=p1*2"
"d11=30m"
"dwdel1=larger(de1,depa)" ;by default 4.50u = de1 = depa, thus dwdel1 = 4.5u
"d12=0.75u" ;based on all the 1,3,5 usec delays in the sequence
"d13=8u" ;assume that p1= 16u, so 1/2*p1=8u
"d14=dw*l1" ;l1=number of points/echo
"dtau=d14+d12-d13-de" ;for the correct timing between 180 pulses
```

```
1 ze
2 30m
d1 pl2:f2
(3u ph0):f2 ;reset the phase of f2 channel back to 0
(p1 ph1:r):f2
dtau
ACQ_START(ph30,ph31)
3 1u REC_BLK
5u
(3u ph0):f2 ;reset the phase of f2 channel back to 0
p1:f2 ph3 ;90 in the composite pulse
p2:f2 ph2 ;180 of the composite pulse
p1:f2 ph4 ;90 in the composite pulse
; (p2 ph2:r):f2 ;we don’t need a phcor2 for this phase to be correct (this statement actually
messes it up!)
dwdel1
5u ph30:r syrec
1u REC_UNBLK
4 dw DWL_CLK_ON
dw DWL_CLK_OFF
lo to 4 times l1
lo to 3 times l4
rcyc=2
30m mc #0 to 2 F0(zd)
exit

ph0=0 ;reset the phase of f2 channel back to 0
ph1=0 ;first pulse is always 90x
```

```
ph2=1 3 ;always alternate 180 pulse (y, -y)
ph3=0 2 ;this is the phase of the 90 pulse in the composite pulse (x, -x)
ph4=0 2;for the other 90 in the composite pulse (x, -x)
ph30=0
ph31=0 0;receiver phase is always x (same as first 90 deg pulse)


;pl2 : f2 channel - power level for pulse
;p1 : f2 channel - 90 degree high power pulse
;p2 : f2 channel - 180 degree high power pulse
;d1 : relaxation delay; 1-5 * T1
;d11: delay for disk I/O [30 msec]
;dtau automatically calculated to give correct tau time
;l1: number of points per echo (npe)
; true tau time is based on tau = (l1*dw)+ (cnst for timing) = l1*dw + 25.75u
;l4: number of echoes (necho)
;;;;;;; MAKE SURE TO SET TD=2*l1*l4 in TopSpin
```

A.1.1.2 zg_grad.nnj

This is a sequence containing a 90° pulse with applied gradient during acquisition. Can be used for linewidth temperature calibration experiments.

```
;zg_grad.nnj
;avance-version (06/11/09)
;1D sequence
;
;$CLASS=HighRes
;$DIM=1D
;$TYPE=
;$SUBTYPE=
;$COMMENT=
```

```
#include <Avance.incl>

"acqt0=-p1*2/3.1416"
1 ze
2 30m
d1
p1 ph1
10u grad(0.2*1)|(0.18574*0)|(0) ;x,y,z
go=2 ph31
groff
30m mc #0 to 2 F0(zd)
exit
ph1=0 2 2 0 1 3 3 1
ph31=0 2 2 0 1 3 3 1

;pl1 : f1 channel - power level for pulse (default)
;p1 : f1 channel - high power pulse
;d1 : relaxation delay; 1-5 * T1
;NS: 1 * n, total number of scans: NS * TD0
;$Id: zg,v 1.9 2006/11/10 10:56:44 ber Exp $
```

A.1.2 Imaging Sequences

A.1.2.1 Pure-Phase Encode Imaging Sequence

A pure-phase encoding imaging sequence. It also contains a temperature-encoding gradient during acquisition. Can be used with both liquids and gases.
MRIS_NNJ

```
#include <Avance.incl>
#include <Grad.incl>
#include <Delay.incl>
#include <De.incl>

"p2 = p1*2"
"d4=d2+d2+d5+d5+d5+d21+d21+d21+d21-d3-400u" ;
"cnst21=4*2"
"cnst31=3.7148*2"
"cnst22=cnst21*-7/11"
"cnst23=cnst21*2/11"
"cnst32=cnst31*-7/11"
"cnst33=cnst31*2/11"

lgrad r1d = td1
lgrad r2d = td2

1 ze
2 200u UNBLKGRAD
200u REC_BLK
d1
p1 ph1 ;90 degree pulse
d2 ; delay to alternate tE2
(d21 grad r1d(1*cnst21) | r2d(1*cnst31) | (0) ) ; ramp up
d5 ;gradient length
(d21 grad r1d(1*cnst22)|r2d(1*cnst32) | (0) ) ; ramp up
d5
(d21 grad r1d(1*cnst23) |r2d(1*cnst33) | (0) ) ; ramp up
d5
```

```
(d21 grad r1d(0*cnst23) | r2d(0*cnst33) | (0) ) ; ramp down
groff
d2 ; delay to alternate tE2
p1 ph3
p1*2 ph2 ; composite pulse
p1 ph3
d4 ; automatic delay tE/2
200u BLKGRAD
200u REC_UNBLK
d3 grad(0.2*1)|(0.18574*0)|(0) ; readout gradient
go=2 ph30; number of scans loop
groff
10m wr #0 if #0 ze
igrad r2d
lo to 2 times td2
10u
igrad r1d
lo to 2 times td1
exit
ph1=0 1 2 3
ph2=1 2 3 0
ph3=0 1 2 3
ph30=0 1 2 3
;ph1=0 0 2 2 1 1 3 3
;ph2=1 3 1 3 0 2 0 2
;ph30=0 0 0 0
;ph31=0 2 1 3
;d2 is tE2
;d21, d22, d23 gradient times for flow compensation
```

A.2 Varian Pulse Sequences

All Varian pulse sequences that I wrote and/or modified are stored on the spectrometer computer (current spectrometer computer is vishnu@chem.ucla.edu). The pulse sequences are stored in the directory /home/vnmr1/vnmrsys/psglib.

A.2.1 Spectroscopy Experiments

A.2.1.1 2pulse.c

This pulse sequence is a standard two pulse experiment.

```c
#include <standard.h>
#include "sgl.c"
#include <math.h>
#include <stdio.h>


#define max(A,B)  ( (A) > (B) ? (A):(B))

static int phs1[16] = {0,2,2,0,1,3,3,1,0,2,2,0,1,3,3,1};
static int phs2[16] = {1,1,3,3,2,2,0,0,0,0,2,2,1,1,3,3};
static int phsrec[16] = {0,2,2,0,1,3,3,1,2,0,0,2,3,1,1,3};

void pulsesequence()
{

 assign(ct,v17);
  assign(zero,v18);
  assign(zero,v19);

  settable(t1,16,phs1);
  settable(t2,16,phs2);
  settable(t4,16,phsrec);

  getelem(t1,v17,v1);
  getelem(t2,v17,v2);
  getelem(t4,v17,v4);

  assign(v4,oph);
  add(oph,v18,oph);
  add(oph,v19,oph);
```

```
   /* equilibrium period */
   status(A);
   hsdelay(d1);

   /* --- tau delay --- */
   status(B);
  shaped_pulse(p1pat,p1,v1,rof1,rof2);
   hsdelay(d2);

   /* --- observe period --- */
   status(C);
  shaped_pulse(p1pat,pw,v2,rof1,rof2);

  delay(d3);

  setreceiver(t4);

 acquire(np,1.0/sw);
}
```

A.2.1.2 90withgrad2.c

This is a sequence containing a 90° pulse with applied gradient during acquisition. Can be used for linewidth temperature calibration experiments.

```
#include <standard.h>
#include "sgl.c"

#define max(A,B)  ( (A) > (B) ? (A):(B))

GENERIC_GRADIENT_T peg;

void pulsesequence()
{
  char slprofile[MAXSTR];
  double gxlvl1;
  double gylvl1;
  double gzlvl1;

  double gpeg, tpeg;
  int rollout;
```

```
  // initialize parameters

  initparms_sis();

  gxlvl1 = getval("gxlvl1");
  gylvl1 = getval("gylvl1");
  gzlvl1 = getval("gzlvl1");

// the gradient
  gpeg=1.0*max(fabs(gxlvl1),max(fabs(gylvl1),fabs(gzlvl1)));
  tpeg=pw+4e-6+(1/sw)*(np/2);

  init_generic(&peg,"peg",gpeg,tpeg);
  rollout = 1;
  peg.rollOut = rollout;

  /* delay(4e-6);*/

  peg.tramp=trise;
  peg.calcFlag = MOMENT_FROM_DURATION_AMPLITUDE_RAMP;
  calc_generic(&peg,WRITE,"gpeg","tpeg");

  /* delay(4e-6);*/

  delay(d1);

  //offset(tof,OBSch);//

  rot_angle(90.0,0.0,0.0); // seems that we need 90,0,0 in order to get x,y,z

 obl_shapedgradient(peg.name,peg.duration,gxlvl1,gylvl1,gzlvl1,NOWAIT);
 shaped_pulse(pwpat,pw,0,rof1,rof2);
 delay(4e-6);

 acquire(np,1.0/sw);

}
```

A.2.1.3 PFG_STE3b.c

Pulsed Field Gradient Stimulated Echo (PFG_STE) for measuring diffusion or velocity when T_2 is very short for the system under study ($T_1 \gg T_2$), like gases in heterogeneous media.

There is also a pulse sequence called PFG_STE3.c, which is the same except with a different phase cycle.

```
#include <standard.h>
#include "sgl.c"

#define max(A,B) ( (A) > (B) ? (A):(B))

//phase cycling
static int phs1[4] = {0,3,2,1}; // first pulse
static int phs2[4] = {0,0,0,0};  //second pulse
static int phs3[4] = {0,0,0,0};  //third pulse
static int phsrec[4] = {0,1,2,3}; //receiver phase

void pulsesequence()
{

GENERIC_GRADIENT_T peg;

// declare internal variables re: gradients //
  double pfgx;
  double pfgy;
  double pfgz;
  double gzlvl1;
  double gpeg; //gpeg and tpeg for pfg gradients
  double tpeg;
  double tramp;
  double d5;

// initialize parameters//
  initparms_sis(); //uses initparms_sis instead of init_mri!!!

// have VnmrJ grab the appropriate values //
  pfgx = getval("pfgx");
  pfgy = getval("pfgy");
  pfgz = getval("pfgz");
  gzlvl1=getval("gzlvl1");
  d5=getval("d5");
  tramp = getval("tramp");
 // tramp = getval("trise");  // should be in seconds

  gpeg=1.5*max(fabs(pfgx),max(fabs(pfgy),fabs(pfgz))); //PFG for diffusion//
  tpeg=d2; //d2 = pfg gradient duration time
```

```
  init_generic(&peg,"peg",gpeg,tpeg);
  printf("␣gpeg=%g␣␣␣tpeg=%g␣\n",gpeg,tpeg);
  peg.tramp=tramp; //tramp = gradient ramp time
  peg.calcFlag = MOMENT_FROM_DURATION_AMPLITUDE_RAMP;
  calc_generic(&peg,WRITE,"gpeg","tpeg");

  printf("Following␣CALC␣we␣have:␣peg.tramp=%g␣␣␣peg.duration=%g␣␣␣peg.amp=%g␣\n",peg.tramp,
      peg.duration,peg.amp);

// for the phase cycling//
  assign(ct,v17);
  assign(zero,v18);
  assign(zero,v19);

  settable(t1,4,phs1);
  settable(t2,4,phs2);
  settable(t3,4,phs3);
  settable(t4,4,phsrec);
  getelem(t1,v17,v1);
  getelem(t2,v17,v2);
  getelem(t3,v17,v3);
  getelem(t4,v17,v4);
  assign(v4,oph);
  add(oph,v18,oph);
  add(oph,v19,oph);

/* the actual pulse sequence
90 -- t -- PFG -- t -- 90 - T -- 90 -- t -- PFG -- t -- ACQUIRE*/

  delay(d1); //d1 = recycle delay, time between scans
  /* THIS LINE GIVES AN ERROR: "warning: implicit declaration of function 'offset'
  offset(tof,OBSch); */
  obsoffset(tof);
  rot_angle(90.0,0.0,0.0); // 90,0,0 gives x,y,z

// 90 degree pulse //
  shaped_pulse(p1pat,p1,v1,rof1,rof2);

// t delay, indicated by d3 //
  delay(d3);

// pulsed-field gradient //
  obl_shapedgradient(peg.name,peg.duration,pfgx,pfgy,pfgz,WAIT);
```

```
// t delay, indicated by d3 //
  delay(d3);

// 90 degree pulse //
  shaped_pulse(p1pat,p1,v2,rof1,rof2);

// T delay with SPOILER gradient//
  delay(d5); //d5 is the big T delay
  zgradpulse(gzlvl1,d4); //d4 is the time for spoiler gradient
  delay(d5);

// 90 degree pulse //
  shaped_pulse(p1pat,p1,v3,rof1,rof2);

// t delay, indicated by d3 //
  delay(d3);

// pulsed-field gradient //
  obl_shapedgradient(peg.name,peg.duration,pfgx,pfgy,pfgz,WAIT);

// t delay, indicated by d3 //
  delay(d3);

// acquire //
  setreceiver(t4);
//  acquire(np,1.0/sw);
}
```

A.2.1.4 Cotts.c

Cotts 9-Interval Sequence [44]. A PFG sequence for improved measurement of fast velocities of fluids with high diffusivity in systems with short T_2^*.

```
#include <standard.h>
#include "sgl.c"

#define max(A,B) ( (A) > (B) ? (A):(B))

//phase cycling
static int phs1[4] = {0,3,2,1}; // first pulse
static int phs2[4] = {0,0,0,0};  //second pulse
static int phs3[4] = {0,0,0,0};  //third pulse
```

```
static int phs4[4] = {1,2,1,2};  //180 pulse
static int phsrec[4] = {0,1,2,3}; //receiver phase

void pulsesequence()
{

GENERIC_GRADIENT_T peg;

// declare internal variables re: gradients //
  double pfgx;
  double pfgy;
  double pfgz;
  double gzlvl1;
  double gpeg; //gpeg and tpeg for pfg gradients
  double tpeg;
  double tramp;
  double d5;

// initialize parameters//
  initparms_sis(); //uses initparms_sis instead of init_mri!!!

// have VnmrJ grab the appropriate values //
  pfgx = getval("pfgx");
  pfgy = getval("pfgy");
  pfgz = getval("pfgz");
  gzlvl1=getval("gzlvl1");
  d5=getval("d5");
  tramp = getval("tramp");
 // tramp = getval("trise");  // should be in seconds

  gpeg=1.5*max(fabs(pfgx),max(fabs(pfgy),fabs(pfgz))); //PFG for diffusion//
  tpeg=d2; //d2 = pfg gradient duration time

  init_generic(&peg,"peg",gpeg,tpeg);
  printf("␣gpeg=%g␣␣␣tpeg=%g␣\n",gpeg,tpeg);
  peg.tramp=tramp; //tramp = gradient ramp time
  peg.calcFlag = MOMENT_FROM_DURATION_AMPLITUDE_RAMP;
  calc_generic(&peg,WRITE,"gpeg","tpeg");

  printf("Following␣CALC␣we␣have:␣peg.tramp=%g␣␣␣peg.duration=%g␣␣␣peg.amp=%g␣\n",peg.tramp,
      peg.duration,peg.amp);

// for the phase cycling//
  assign(ct,v17);
```

```
  assign(zero,v18);
  assign(zero,v19);

  settable(t1,4,phs1);
  settable(t2,4,phs2);
  settable(t3,4,phs3);
settable(t5,4,phs4);
  settable(t4,4,phsrec);
  getelem(t1,v17,v1);
  getelem(t2,v17,v2);
  getelem(t3,v17,v3);
getelem(t5,v17,v5);
  getelem(t4,v17,v4);
  assign(v4,oph);
  add(oph,v18,oph);
  add(oph,v19,oph);

/* the actual pulse sequence
90 -- t -- PFG -- t -- 90 - T -- 90 -- t -- PFG -- t -- ACQUIRE*/

  delay(d1); //d1 = recycle delay, time between scans
  /* THIS LINE GIVES AN ERROR: "warning: implicit declaration of function 'offset'
  offset(tof,OBSch); */
  obsoffset(tof);
  rot_angle(90.0,0.0,0.0); // 90,0,0 gives x,y,z

// 90 degree pulse //
  shaped_pulse(p1pat,p1,v1,rof1,rof2);

// t delay, indicated by d3 //
  delay(d3*2);

// 180 degree pulse //
  shaped_pulse(p1pat,p1*2,v5,rof1,rof2);

// t delay, indicated by d3 //
  delay(d3/2-p1-rof1);

// pulsed-field gradient //
  obl_shapedgradient(peg.name,peg.duration,pfgx,pfgy,pfgz,WAIT);

// t delay, indicated by d3 //
  delay(d3/2-p1-rof1);
```

```
// 90 degree pulse //
  shaped_pulse(p1pat,p1,v2,rof1,rof2);

// T delay with SPOILER gradient//
  delay(d5); //d5 is the big T delay
  zgradpulse(gzlvl1,d4); //d4 is the time for spoiler gradient
  delay(d5);

// 90 degree pulse //
  shaped_pulse(p1pat,p1,v3,rof1,rof2);

// t delay, indicated by d3 //
  delay(d3/2-p1-rof1);

// pulsed-field gradient //
  obl_shapedgradient(peg.name,peg.duration,pfgx,pfgy,pfgz,WAIT);

// t delay, indicated by d3 //
  delay(d3/2-p1-rof1);

// 180 degree pulse //
  shaped_pulse(p1pat,p1*2,v5,rof1,rof2);

// t delay, indicated by d3 //
  delay(d3*2);
// acquire //
  setreceiver(t4);
//  acquire(np,1.0/sw);
}
```

A.2.1.5 CPMG_echotrain4.c

Carr-Purcell-Meiboom-Gill (CPMG) Echo Train. Used for measuring T_2 relaxation times. There are multiple versions of the echotrain experiment with different phase cycling, as well as a version with a gradient on, which was used in Chapter 3.

```
/* to use this sequence do (after doing all the usual things...):
 - seqfil='CPMG_echotrain4'
 - create ('npe','real') -- number of points per echo
 - create('necho','real') -- number of echoes
 - type DPS in VNMRJ so npe is updated (this should automatically get updated)
 - set the number of echoes; set necho = whatever you want, but it has to be a factor of 16
```

```
 - then type np=necho*npe -- total number of points
 - run sequence (at should be automatically adjusted to accommodate the value of np)
 - check the value of at (before and after changing the value of np) - it should be updated
     */

#include <standard.h>
#include "sgl.c"

static int ph2[1] = {0};
static int ph3[2] = {1,1}; //180 in the MLEV
static int ph4[2] = {3,3}; //receiver phase
//ph1 is the very first 90 deg pulse: should be x
//receiver phase should always be -y

void pulsesequence()
{
  double sw, tof, tpwr, d2, npts, cnst1, cnst2;
  double necho;
  int vnp     = v8;
  int vnp_ctr = v5;
  char pulseflag[MAXSTR];



  necho=getval("necho");
          initval(necho,v8);
  getstr("pulseflag",pulseflag);
  sw=getval("sw");
  tof=getval("tof");
  tpwr=getval("tpwr");
  d2=getval("d2"); // tau = d2

  assign(zero,v18); //sets v18 = 0
          settable(t2,16,ph2);
          getelem(t2,v5,v2);
          settable(t3,16,ph3);
          getelem(t3,v5,v3);
          settable(t4,4,ph4); //receiver
          getelem(t4,v5,v4);
  assign(v4,oph); //sets oph to have a value of v4


  /* equilibrium period */
  delay(d1);
```

```
  /* --- tau delay --- */
  rgpulse(p1,0.0,rof1,rof2); //this first 90 is always phase of X (0)
        cnst1=(5/2)*p1+2*(rof1+rof2);
  delay(d2-cnst1-alfa); // {(5/2*p1 + 2*(ROF1 + ROF2)} must be subtacted from d2 to get true tau
        //if we don't subtract alfa, the timing is incorrect

  /* --- observe period --- */
  obsoffset(tof);
  obspower(tpwr);

        cnst2=4*p1+3*(rof1+rof2); //again for the timing of 2*tau
  npts=(int) (2.0*(2.0*d2-cnst2)*sw); //cnst2 is subtracted from 2*d2 to get true 2*tau

  putvalue("npe", npts); // in VNMRJ create('npe','real')
  // then in VNMRJ you type:  np=necho*npe

 startacq(alfa);
 setreceiver(t4);
    loop(vnp,vnp_ctr);
     rgpulse(2.0*p1,v3,rof1,rof2); //180 of composite pulse
        startacq(alfa);
        acquire(npts,1.0/sw);
     endacq();
    endloop(vnp_ctr);
endacq();

}
```

A.2.2 Imaging Experiments

A.2.2.1 nanette8gas.c

A (single-lobe) pure-phase encoding imaging sequence that also has bipolar velocity-encoding gradients. It also contains a temperature-encoding gradient during acquisition. Can be used with both liquids and gases.

```
#include <standard.h>
#include "sgl.c"
#include <math.h>
#include <stdio.h>
```

```
#define max(A,B)  ( (A) > (B) ? (A):(B))

GENERIC_GRADIENT_T veg, peg, tempg;

pulsesequence()
{

 //Internal Variable Declarations first
  double gxlvl1, gylvl1, gzlvl1; //temp grad
  double gtemp, ttemp; //temp grad

  double gxpeg, gypeg, gzpeg; //phase-encode gradients
  double gxveg, gyveg, gzveg; //velocity-encode gradients
  double d2, d3, d4, d5; //delays
  double gveg, tveg, gpeg, tpeg; //gradient variables and timings
  double M0x, M0y, M0z, M1x, M1y, M1z; //zeroth and first moments
  double tplateau, tramp, tramp2, m1, fwamp, gamma, venc;

//Initialize gradient parameters
  initparms_sis(); //uses initparms_sis instead of init_mri!!!
     /* NNJ 6/19/14-- need to use initparms_sis instead of init_mri and initialize with an
         s2pul sequence. otherwise we get an error  "Receiever(s) have failed to complete
         data upload*/
  gxlvl1 = getval("gxlvl1");
  gylvl1 = getval("gylvl1");
  gzlvl1 = getval("gzlvl1");

  gtemp=1.0*max(fabs(gxlvl1),max(fabs(gylvl1),fabs(gzlvl1))); //temp grad
  ttemp=(1/sw)*(np/2); //tempgrad



  gxpeg = getval("gxpeg");
  gypeg = getval("gypeg");
  gzpeg = getval("gzpeg");
         gpeg=max(fabs(gxpeg),max(fabs(gypeg),fabs(gzpeg))); // PE gradient
        // NNJ 6/24/14 note: if we don't have this max(fabs) structure, cannot initialize
            gradient structures
  gxveg = getval("gxveg");
  gyveg = getval("gyveg");
  gzveg = getval("gzveg");
          gveg=max(fabs(gxveg),max(fabs(gyveg),fabs(gzveg))); // VE gradient
        // NNJ 6/24/14 note: if we don't have this max(fabs) structure, cannot compile
            sequence
  d2 = getval("d2");
```

```
        tpeg=d2;
  d3 = getval("d3");
        tveg=d3;
  d4 = getval("d4");
  d5 = getval("d5");
  tramp = getval("tramp"); //tramp is for the phase encode gradient
  tramp2 = getval("tramp2"); //tramp2 is for the velocity encode gradient

//Initialize gradient structures
  init_generic(&peg,"peg",gpeg, tpeg);
  init_generic(&veg,"veg",gveg, tveg);
  init_generic(&tempg,"tempg",gtemp,ttemp);

  tramp=300e-6;
  tramp2=300e-6;
  peg.tramp=tramp; //NNJ
  veg.tramp=tramp2; //NNJ
  tempg.tramp=100e-6; //temp grad
  tempg.calcFlag=MOMENT_FROM_DURATION_AMPLITUDE_RAMP; //temp grad

  peg.calcFlag=MOMENT_FROM_DURATION_AMPLITUDE_RAMP; //NNJ

 // Zeroth moment calculations
  M0x = (11.0/11.0)*peg.duration*gxpeg; //NNJ changed from 6/11 to 11/11
  M0y = (11.0/11.0)*peg.duration*gypeg;
  M0z = (11.0/11.0)*peg.duration*gzpeg;

 // First moment calculations
 // X FW Gradient
  veg.amp=gxveg; // LSB
  fwamp=veg.amp; // LSB
  tplateau=veg.duration-2.0*veg.tramp; // LSB
  m1=fwamp*(tplateau + tramp2)*(tplateau + 2.0*tramp2); // LSB
  M1x=m1; // LSB
  veg.calcFlag=MOMENT_FROM_DURATION_AMPLITUDE_RAMP; //NNJ

  // Y FW Gradient
  veg.amp=gyveg; // LSB
  fwamp=veg.amp; // LSB
  tplateau=veg.duration-2.0*veg.tramp; // LSB
  m1=fwamp*(tplateau + tramp2)*(tplateau + 2.0*tramp2); // LSB
  M1y=m1; // LSB
  veg.calcFlag=MOMENT_FROM_DURATION_AMPLITUDE_RAMP; //NNJ
```

```
  // Z FW Gradient
  veg.amp=gzveg; // LSB
  fwamp=veg.amp; // LSB
  tplateau=veg.duration-2.0*veg.tramp; // LSB
  m1=fwamp*(tplateau + tramp2)*(tplateau + 2.0*tramp2); // LSB
  M1z=m1; //NNJ
  veg.calcFlag=MOMENT_FROM_DURATION_AMPLITUDE_RAMP; //NNJ

//Gradient calculations
  calc_generic(&peg,WRITE,"gpeg","tpeg");
  calc_generic(&veg,WRITE,"gveg","tveg");
  calc_generic(&tempg,WRITE,"gtemp","ttemp");

  //output gradient pulse parameters
  printf("Phase-encoding␣gradient␣pulse:\n");
  printf("PE␣duration:␣%f␣\n",peg.duration);
  printf("PE␣ramp␣time:␣%f␣\n",peg.tramp);
  printf("PE␣amplitude␣(gxpeg):␣%f␣\n",gxpeg);
  printf("PE␣amplitude␣(gypeg):␣%f␣\n",gypeg);
  printf("PE␣amplitude␣(gzpeg):␣%f␣\n",gzpeg);

  printf("Velocity-encoding␣gradient␣pulse:\n");
  printf("VE␣duration:␣%f␣\n",veg.duration);
  printf("VE␣ramp␣time:␣%f␣\n",veg.tramp);
  printf("VE␣amplitude␣(gxveg):␣%f␣\n",gxveg);
  printf("VE␣amplitude␣(gyveg):␣%f␣\n",gyveg);
  printf("VE␣amplitude␣(gzveg):␣%f␣\n",gzveg);

  printf("␣PE␣grad␣-␣M0x:␣%f␣M0y:␣%f␣M0z:␣%f␣[units:␣gauss.s]␣␣␣␣VE␣grad␣-␣M1x:␣%f␣M1y:␣%f␣
      M1z:␣%f␣[units:␣gauss.s2]␣\n", M0x, M0y, M0z, M1x, M1y, M1z);

  printf("␣VELOCITY␣ENCODING␣CORRESPONDING␣TO␣M1:\n"); // LSB
  gamma=2.0*M_PI*42.2e6; // LSB
  venc=100.0*M_PI/gamma/M1x; // 100x factor arises from conversion of T to gauss, and cm to
      m.  // LSB
  printf("␣␣␣m1x␣␣venc=%f␣␣[m/s]␣\n", venc); // LSB

  venc=100.0*M_PI/gamma/M1y; // 100x factor arises from conversion of T to gauss, and cm to
      m.  // LSB
  printf("␣␣␣m1y␣␣venc=%f␣␣[m/s]␣\n", venc); // LSB

  venc=100.0*M_PI/gamma/M1z; // 100x factor arises from conversion of T to gauss, and cm to
      m.  // LSB
  printf("␣␣␣m1z␣␣venc=%f␣␣[m/s]␣\n", venc); // LSB
```

```
  delay(d1);

  rot_angle(90.0,0.0,0.0); //need 90,0,0 to set x,y,z

  shaped_pulse(p1pat,p1,0.0,rof1,rof2);

  /*phase encode gradient is first; otherwise it has 1st moment that is NONzero*/
  /* zeroth moment: 6 D G/11 */
  obl_shapedgradient(peg.name,peg.duration,gxpeg,gypeg,gzpeg,WAIT);

  delay(4.0e-6);

  /* velocity encoding*/
  obl_shapedgradient(veg.name,veg.duration,gxveg,gyveg,gzveg,WAIT);
  obl_shapedgradient(veg.name,veg.duration,-1.0*gxveg,-1.0*gyveg,-1.0*gzveg,WAIT);

  //here is the 180 refocusing pulse
  shaped_pulse(p1pat,p2,1,rof1,rof2);

  /*delay(peg.duration); // spin echo delay TE/2 - 180 - TE/2 - acquire*/
  d5 = peg.duration + 2.0*veg.duration + 4.0e-6 ;
  delay(d5);

  obl_shapedgradient(tempg.name,tempg.duration,gxlvl1,gylvl1,gzlvl1,NOWAIT); //temp gradient
  acquire(np,1.0/sw);

}
```

A.2.2.2 STE_imaging.c

A pure-phase encoding stimulated echo (STE) imaging sequence. It has a pair of velocity encode gradients and a temperature-encoding gradient during acquisition. Can be used with both liquids and gases.

```
#include <standard.h>
#include "sgl.c"

#define max(A,B) ( (A) > (B) ? (A):(B))

//phase cycling
static int phs1[4] = {0,2,0,2}; // first pulse
```

```
static int phs2[4] = {0,0,2,2};  //second pulse
static int phs3[4] = {0,0,0,0};  //third pulse
static int phsrec[4] = {0,2,2,0}; //receiver phase

void pulsesequence()
{

GENERIC_GRADIENT_T peg;
GENERIC_GRADIENT_T pfg;

// declare internal variables re: gradients //
  double pfgx;
  double pfgy;
  double pfgz;
  double gzlvl1;
  double gpeg; //gpeg and tpeg for pfg gradients
  double pegx;
  double pegy;
  double pegz;
  double tpeg;
  double tramp;
  double d5;
  double d6;
  double gpfg;
  double tpfg;
 // double pfg;

// initialize parameters//
  initparms_sis(); //uses initparms_sis instead of init_mri!!!

// have VnmrJ grab the appropriate values //
  pegx = getval("pegx");
  pegy = getval("pegy");
  pegz = getval("pegz");
  pfgx = getval("pfgx");
  pfgy = getval("pfgy");
  pfgz = getval("pfgz");
  gzlvl1=getval("gzlvl1");
  d5=getval("d5");
  d6=getval("d6");
  tramp = getval("tramp");
 // tramp = getval("trise");  // should be in seconds

  gpeg=1.5*max(fabs(pegx),max(fabs(pegy),fabs(pegz))); //for phase encode gradient
```

```
  tpeg=d6; //d6 = phase encode gradient duration time

  gpfg=1.5*max(fabs(pfgx),max(fabs(pfgy),fabs(pfgz))); //PFG for diffusion//
  tpfg=d2; //d2 = pfg gradient duration time

  init_generic(&peg,"peg",gpeg,tpeg);
  printf("␣gpeg=%g␣␣␣tpeg=%g␣\n",gpeg,tpeg);
  peg.tramp=tramp; //tramp = gradient ramp time
  peg.calcFlag = MOMENT_FROM_DURATION_AMPLITUDE_RAMP;
  calc_generic(&peg,WRITE,"gpeg","tpeg");

  init_generic(&pfg,"pfg",gpfg,tpfg);
  printf("␣gpef=%g␣␣␣tpeg=%g␣\n",gpfg,tpfg);
  pfg.tramp=tramp; //tramp = gradient ramp time
  pfg.calcFlag = MOMENT_FROM_DURATION_AMPLITUDE_RAMP;
  calc_generic(&pfg,WRITE,"gpfg","tpfg");

  //printf("Following CALC we have: peg.tramp=%g   peg.duration=%g   peg.amp=%g \n",peg.
      tramp,peg.duration,peg.amp);

// for the phase cycling//
  assign(ct,v17);
  assign(zero,v18);
  assign(zero,v19);

  settable(t1,4,phs1);
  settable(t2,4,phs2);
  settable(t3,4,phs3);
  settable(t4,4,phsrec);
  getelem(t1,v17,v1);
  getelem(t2,v17,v2);
  getelem(t3,v17,v3);
  getelem(t4,v17,v4);
  assign(v4,oph);
  add(oph,v18,oph);
  add(oph,v19,oph);

/* the actual pulse sequence
90 -- t -- PFG -- t -- 90 - T -- 90 -- t -- PFG -- t -- ACQUIRE*/

  delay(d1); //d1 = recycle delay, time between scans
  /* THIS LINE GIVES AN ERROR: "warning: implicit declaration of function 'offset'
  offset(tof,OBSch); */
  obsoffset(tof);
```

```
  rot_angle(90.0,0.0,0.0); // 90,0,0 gives x,y,z

// 90 degree pulse //
  shaped_pulse(p1pat,p1,v1,rof1,rof2);

  delay(4e-6);

// t delay, indicated by d3 //
  delay(d3);

// pulsed-field gradient //
  obl_shapedgradient(pfg.name,pfg.duration,pfgx,pfgy,pfgz,WAIT);

// t delay, indicated by d3 //
  delay(d3);

// 90 degree pulse //
  shaped_pulse(p1pat,p1,v2,rof1,rof2);

// T delay with SPOILER gradient//
  delay(d5); //d5 is the big T delay
  zgradpulse(gzlvl1,d4); //d4 is the time for spoiler gradient
  delay(d5);

// 90 degree pulse //
  shaped_pulse(p1pat,p1,v3,rof1,rof2);

// t delay, indicated by d3 //
  delay(d3);

// pulsed-field gradient //
  obl_shapedgradient(pfg.name,pfg.duration,pfgx,pfgy,pfgz,WAIT);

  delay(4e-6);

// phase-encode gradient//
  obl_shapedgradient(peg.name,peg.duration,pegx,pegy,pegz,WAIT);



// acquire //
  setreceiver(t4);
//  acquire(np,1.0/sw);
}
```

A.2.2.3 semsflow4.c

A spin echo multi-slice (SEMS) flow imaging sequence, used for imaging velocities in systems with flowing liquids. Cannot work with gases until very high pressures or hyperpolarized gases due to lower SNR in traditional imaging sequences compared to pure-phase encoding sequences.

```
#include <standard.h>
#include "sgl.c"

#include <math.h>
#include <stdio.h>

#define max(A,B)  ( (A) > (B) ? (A):(B))    /* LSB */

GENERIC_GRADIENT_T ssr1_grad; // LSB flow comp slice select refocus
GENERIC_GRADIENT_T ssr2_grad; // LSB flow comp slice select refocus
GENERIC_GRADIENT_T fw1_grad, fw2_grad; // bipolar flow weighting gradient   // LSB
GENERIC_GRADIENT_T ro8_grad, ro7_grad; // readout grad flow comp prephaser // LSB
GENERIC_GRADIENT_T fc180l_grad, fc180r_grad; // 180 flow comp // LSB

/* Phase cycling of 180 degree pulse */
static int ph180[2] = {1,3};

pulsesequence()
{

  /* Internal variable declarations *********************/
  double   freq90[MAXNSLICE],freq180[MAXNSLICE];
  double   te_delay1,te_delay2,tr_delay,tau1,tau2,thk2fact,te_delay3=0.0,te_delay4=0.0,
      navTime=0.0;
  double   crushm0,pem0,gcrushr,gcrushp,gcrushs,pecrush;
  double   refsign=1,crushsign=1,navsign=1;
  int      shape90,shape180,table=0,sepRefocus;
  char     slprofile[MAXSTR];

  /* sequence dependent diffusion variables */
  double Gro,Gss;          // "gdiff" for readout/readout refocus and slice/slice refocus
  double dgro,dgss;        // "delta" for readout/readout refocus and slice/slice refocus
  double Dgro,Dgss;        // "DELTA" for readout/readout refocus and slice/slice refocus
  double dcrush,dgss2;     // "delta" for crusher and gss2 gradients
  double Dcrush,Dgss2;     // "DELTA" for crusher and gss2 gradients
```

```
int    i;

/* Real-time variables used in this sequence **********/
int  vpe_steps  = v1;    // Number of PE steps
int  vpe_ctr    = v2;    // PE loop counter
int  vms_slices = v3;    // Number of slices
int  vms_ctr    = v4;    // Slice loop counter
int  vpe_offset = v5;    // PE/2 for non-table offset
int  vpe_mult   = v6;    // PE multiplier, ranges from -PE/2 to PE/2
int  vph180     = v7;    // Phase of 180 pulse
int  vph2       = v8;    // alternate phase of 180 on odd transients
int  vssc       = v9;    // Compressed steady-states
int  vtrimage   = v10;   // Counts down from nt, trimage delay when 0
int  vacquire   = v11;   // Argument for setacqvar, to skip steady state acquires
int  vtrigblock = v12;   // Number of slices per trigger block

// LSB needed variables
double G1, G2, G3, G4, G5, G6, G7, G8, G9, G10; // LSB
double tplateau, tplateau2, tplateau7, tplateau3; // LSB
double tramp, tramp2, tramp3, tramp7; // LSB
double gssr1_grad, tssr1_grad, gssr2_grad, tssr2_grad; // LSB
double rfFraction, rfDuration, rfDelayCenterBack; // LSB
double gfw1_grad, tfw1_grad, gfw2_grad, tfw2_grad; // LSB
double gamma, m1, venc; // LSB
double fwamp, fwampx, fwampy, fwampz; // LSB
double gro8_grad, gro7_grad, tro8_grad, tro7_grad; // LSB
double gfc180l_grad, gfc180r_grad, tfc180l_grad, tfc180r_grad; // LSB

/*  Initialize paramaters *****************************/
init_mri();

thk2fact=getval("thk2fact");
pecrush=getval("pecrush");
sepRefocus=getvalnwarn("sepRefocus");
sepRefocus=0; // LSB hardcode this option - we always want PE grad at beginning
getstrnwarn("slprofile",slprofile);

/*  Check for external PE table ***********************/
init_tablepar("pelist");          // Initialize pelist parameter
if (strcmp(petable,"n") && strcmp(petable,"N") && strcmp(petable,"")) {
  loadtable(petable);
  writetabletopar(t1,"pelist");   // Write t1 table to pelist parameter
  table = 1;
}
```

```
// initialize variables

fwampx=getval("fwampx"); // LSB pull these parameter values from VNMRJ environment
fwampy=getval("fwampy"); // LSB
fwampz=getval("fwampz"); // LSB

/* RF Power & Bandwidth Calculations ******************/
shape_rf(&p1_rf,"p1",p1pat,p1,flip1,rof1,rof2);
shape_rf(&p2_rf,"p2",p2pat,p2,flip2,rof1,rof2);
calc_rf(&p1_rf,"tpwr1","tpwr1f");
calc_rf(&p2_rf,"tpwr2","tpwr2f");

/* Initialize gradient structures *********************/
init_slice(&ss_grad,"ss",thk);
init_slice(&ss2_grad,"ss2",thk*thk2fact);
init_dephase(&crush_grad,"crush");
init_slice_refocus(&ssr_grad,"ssr");
if (FP_LT(tcrushro,alfa)) tcrushro=alfa;
//  init_readout_butterfly(&ro_grad,"ro",lro,np,sw,gcrushro,tcrushro); // LSB
init_readout(&ro_grad,"ro",lro,np,sw); // LSB
init_readout_refocus(&ror_grad,"ror");
init_phase(&pe_grad,"pe",lpe,nv);
init_generic(&spoil_grad,"spoil",gspoil,tspoil);

/* Gradient calculations ******************************/
calc_readout(&ro_grad, WRITE,"gro","sw","at");
ro_grad.m0ref *= grof;
calc_readout_refocus(&ror_grad,&ro_grad,NOWRITE,"gror");
calc_phase(&pe_grad,WRITE,"gpe","tpe");
calc_slice(&ss_grad,&p1_rf,WRITE,"gss");
calc_slice(&ss2_grad,&p2_rf,WRITE,"gss2");
calc_slice_refocus(&ssr_grad,&ss_grad,WRITE,"gssr");
calc_generic(&spoil_grad,WRITE,"","");

// LSB flow weighting gradient

fwamp=max(max(fabs(fwampx),fabs(fwampy)),fabs(fwampz)); // LSB

gfw1_grad=fwamp; // LSB
gfw2_grad=-fwamp; // LSB
tfw1_grad=5e-3; // 5ms long  // LSB
tfw2_grad=5e-3; // 5ms long  // LSB
tramp=600e-6; // 600us ramp time    // LSB
```

```
init_generic(&fw1_grad,"fw1",gfw1_grad,tfw1_grad); // LSB
init_generic(&fw2_grad,"fw2",gfw2_grad,tfw2_grad); // LSB

fw1_grad.tramp=tramp; // LSB
fw2_grad.tramp=tramp; // LSB
fw1_grad.amp=fwamp; // LSB
fw2_grad.amp=fwamp; // LSB
fw1_grad.calcFlag=MOMENT_FROM_DURATION_AMPLITUDE_RAMP; // LSB
fw2_grad.calcFlag=MOMENT_FROM_DURATION_AMPLITUDE_RAMP; // LSB

calc_generic(&fw1_grad,WRITE,"gfw1_grad","tfw1_grad"); // LSB
calc_generic(&fw2_grad,WRITE,"gfw2_grad","tfw2_grad"); // LSB

tplateau=fw1_grad.duration-2.0*fw1_grad.tramp; // LSB
tramp=fw1_grad.tramp; // LSB
printf("␣M1:␣FIRST␣MOMENT␣OF␣BIPOLAR␣GRADIENT:\n"); // LSB
m1=fwamp*(tplateau + tramp)*(tplateau + 2.0*tramp); // LSB
printf("␣␣␣␣␣m1=%f␣␣[gauss/cm␣s2]␣\n", m1); // LSB
printf("␣VELOCITY␣ENCODING␣CORRESPONDING␣TO␣M1:\n"); // LSB
gamma=2.0*M_PI*42.2e6; // LSB
venc=100.0*M_PI/gamma/m1; // 100x factor arises from conversion of T to gauss, and cm to m
    .  // LSB
printf("␣␣␣␣␣venc=%f␣␣[m/s]␣\n", venc); // LSB



// LSB calc flow comp ss refocus pulses

G1=ss_grad.amp;  // LSB
tplateau=ss_grad.duration-2.0*ss_grad.tramp; // LSB
tplateau2=0.3*tplateau; // LSB
rfFraction=ss_grad.rfFraction; // LSB
rfDuration=ss_grad.rfDuration; // LSB
tramp=ss_grad.tramp; // LSB
tramp2=100e-6; // LSB

G2=-(1.0/(12.0*(tplateau2 + tramp2)*(tplateau2 + 2.0*tramp2))) * // LSB
  (6.0*G1*pow(rfDuration,2.0)*pow(rfFraction,2.0) +  // LSB
   18.0*G1*rfDuration*rfFraction*tplateau2 +  // LSB
   12.0*G1*rfDuration*rfFraction*tramp + 9.0*G1*tplateau2*tramp +  // LSB
   4.0*G1*pow(tramp,2.0) + 36.0*G1*rfDuration*rfFraction*tramp2 +  // LSB
   18.0*G1*tramp*tramp2); // LSB
```

```
G3=-(1.0/(12.0*(tplateau2 + tramp2)*(tplateau2 + 2.0*tramp2))) * // LSB
  (-6.0*G1*pow(rfDuration,2.0)*pow(rfFraction,2.0) -  // LSB
   6.0*G1*rfDuration*rfFraction*tplateau2 -  // LSB
   12.0*G1*rfDuration*rfFraction*tramp - 3.0*G1*tplateau2*tramp -  // LSB
   4.0*G1*pow(tramp,2.0) - 12.0*G1*rfDuration*rfFraction*tramp2 -  // LSB
   6.0*G1*tramp*tramp2); // LSB

printf("␣G1=%f,␣G2=%f,␣G3=%f␣\n", G1, G2, G3); // LSB

gssr1_grad=G2; // LSB
gssr2_grad=G3; // LSB
tssr1_grad=tplateau2+2.0*tramp; // LSB
tssr2_grad=tplateau2+2.0*tramp; // LSB

init_generic(&ssr1_grad,"ssr1",gssr1_grad,tssr1_grad); //   init_slice_refocus(&ssr_grad,"
    ssr");  // LSB
init_generic(&ssr2_grad,"ssr2",gssr2_grad,tssr2_grad); // LSB

ssr1_grad.tramp=tramp; // LSB
ssr2_grad.tramp=tramp; // LSB
ssr1_grad.amp=G2; // LSB
ssr2_grad.amp=G3; // LSB
ssr1_grad.calcFlag=MOMENT_FROM_DURATION_AMPLITUDE_RAMP; // LSB
ssr2_grad.calcFlag=MOMENT_FROM_DURATION_AMPLITUDE_RAMP; // LSB

calc_generic(&ssr1_grad,WRITE,"gssr1_grad","tssr1_grad"); // LSB
calc_generic(&ssr2_grad,WRITE,"gssr2_grad","tssr2_grad"); // LSB

printf("␣G1.amp=%f,␣G2.amp=%f,␣G3.amp=%f␣\n", ss_grad.amp, ssr1_grad.amp, ssr2_grad.amp);
    // LSB
printf("␣G1.tramp=%f,␣G2.tramp=%f,␣G3.tramp=%f␣\n", ss_grad.tramp, ssr1_grad.tramp,
    ssr2_grad.tramp); // LSB

rfDelayCenterBack=ss_grad.rfFraction*ss_grad.rfDuration+ss_grad.pad2+ss_grad.rfDelayBack;
    // LSB
printf("␣RF1:␣amp=%f␣␣rfdelaycenterback=%f␣␣tramp=%f␣␣m0=%f␣\n", ss_grad.amp,
    rfDelayCenterBack, ss_grad.tramp, // LSB
       ss_grad.amp*(rfDelayCenterBack-0.5*ss_grad.tramp)); // LSB
printf("␣G2:␣m0=%f␣\n", G2*(ssr1_grad.duration-ssr1_grad.tramp)); // LSB
printf("␣G3:␣m0=%f␣\n", G3*(ssr2_grad.duration-ssr2_grad.tramp)); // LSB
printf("␣total␣m0=%f␣\n", ss_grad.amp*(rfDelayCenterBack-0.5*ss_grad.tramp) +  // LSB
       G2*(ssr1_grad.duration-ssr1_grad.tramp) +  // LSB
       G3*(ssr2_grad.duration-ssr2_grad.tramp)); // LSB
```

```
// LSB for backward compatibility
G5=crush_grad.amp;

// LSB 180 flow comp  //  fc180l_grad, fc180r_grad
tplateau2=crush_grad.duration-2.0*crush_grad.tramp; // LSB
tplateau3=3000e-6; // LSB
tramp3=600e-6; // LSB
tramp2=crush_grad.tramp; // LSB
tramp=ss2_grad.tramp; // LSB
G10=(1.0/(12.0*(tplateau3 + tramp3)*(tplateau3 + 2.0*tramp3))) * // LSB
  (-3.0*ss2_grad.amp*pow(tplateau,2.0) - 12.0*G5*tplateau*tplateau2 -  // LSB
   12.0*G5*pow(tplateau2,2.0) - 6.0*ss2_grad.amp*tplateau*tramp -  // LSB
   24.0*G5*tplateau2*tramp - 4.0*ss2_grad.amp*pow(tramp,2.0) - 12.0*G5*tplateau*tramp2 -
       // LSB
   36.0*G5*tplateau2*tramp2 - 24.0*G5*tramp*tramp2 - 24.0*G5*pow(tramp2,2.0)); // LSB

gfc180l_grad=G10; // LSB
gfc180r_grad=G10; // LSB
tfc180l_grad=tplateau3+2.0*tramp3; // LSB
tfc180r_grad=tplateau3+2.0*tramp3; // LSB

init_generic(&fc180l_grad,"fc180l",gfc180l_grad,tfc180l_grad); // LSB
init_generic(&fc180r_grad,"fc180r",gfc180r_grad,tfc180r_grad); // LSB

fc180l_grad.tramp=tramp3; // LSB
fc180r_grad.tramp=tramp3; // LSB
fc180l_grad.amp=G10; // LSB
fc180r_grad.amp=G10; // LSB
fc180l_grad.calcFlag=MOMENT_FROM_DURATION_AMPLITUDE_RAMP; // LSB
fc180r_grad.calcFlag=MOMENT_FROM_DURATION_AMPLITUDE_RAMP; // LSB

calc_generic(&fc180l_grad,WRITE,"gfc180l_grad","tfc180l_grad"); // LSB
calc_generic(&fc180r_grad,WRITE,"gfc180r_grad","tfc180r_grad"); // LSB

// LSB calc flow comp readout prephasers

tplateau7=600e-6; // LSB
tramp7=100e-6; // LSB
G9=ro_grad.amp; // LSB
G7=-(1.0/(24.0*(tplateau7 + tramp7)*(tplateau7 + 2.0*tramp7)))* // LSB
  (3.0*pow(ro_grad.acqTime,2.0)*G9 - 12.0*pow(ro_grad.acqTime,2.0)*ro_grad.echoFraction*G9
        // LSB
   + 12.0*pow(ro_grad.acqTime,2.0)*pow(ro_grad.echoFraction,2.0)*G9 -  // LSB
   12.0*ro_grad.acqTime*G9*ro_grad.pad1 + 24.0*ro_grad.acqTime*ro_grad.echoFraction*G9*
```

```
       ro_grad.pad1 +  // LSB
   12.0*G9*pow(ro_grad.pad1,2.0)- 18.0*ro_grad.acqTime*G9*tplateau7 +  // LSB
   36.0*ro_grad.acqTime*ro_grad.echoFraction*G9*tplateau7 + 36.0*G9*ro_grad.pad1*tplateau7
        -  // LSB
   12.0*ro_grad.acqTime*G9*ro_grad.tramp + 24.0*ro_grad.acqTime*ro_grad.echoFraction*G9*
       ro_grad.tramp +  // LSB
   24.0*G9*ro_grad.pad1*ro_grad.tramp + 18.0*G9*tplateau7*ro_grad.tramp + 8.0*G9*pow(
       ro_grad.tramp,2.0) -  // LSB
   36.0*ro_grad.acqTime*G9*tramp7 + 72.0*ro_grad.acqTime*ro_grad.echoFraction*G9*tramp7 +
        // LSB
   72.0*G9*ro_grad.pad1*tramp7 + 36.0*G9*ro_grad.tramp*tramp7); // LSB
G8=-(1.0/(24.0*(tplateau7 + tramp7)*(tplateau7 + 2.0*tramp7)))* // LSB
  (-3.0*pow(ro_grad.acqTime,2.0)*G9 + 12.0*pow(ro_grad.acqTime,2.0)*ro_grad.echoFraction*
      G9  // LSB
   - 12.0*pow(ro_grad.acqTime,2.0)*pow(ro_grad.echoFraction,2.0)*G9 +  // LSB
   12.0*ro_grad.acqTime*G9*ro_grad.pad1 - 24.0*ro_grad.acqTime*ro_grad.echoFraction*G9*
       ro_grad.pad1 -  // LSB
   12.0*G9*pow(ro_grad.pad1,2.0) + 6.0*ro_grad.acqTime*G9*tplateau7 -  // LSB
   12.0*ro_grad.acqTime*ro_grad.echoFraction*G9*tplateau7 - 12.0*G9*ro_grad.pad1*tplateau7
        +  // LSB
   12.0*ro_grad.acqTime*G9*ro_grad.tramp - 24.0*ro_grad.acqTime*ro_grad.echoFraction*G9*
       ro_grad.tramp -  // LSB
   24.0*G9*ro_grad.pad1*ro_grad.tramp - 6.0*G9*tplateau7*ro_grad.tramp - 8.0*G9*pow(
       ro_grad.tramp,2.0) +  // LSB
   12.0*ro_grad.acqTime*G9*tramp7 - 24.0*ro_grad.acqTime*ro_grad.echoFraction*G9*tramp7 -
        // LSB
   24.0*G*ro_grad.pad1*tramp7 - 12.0*G9*ro_grad.tramp*tramp7); // LSB

gro8_grad=G8; // LSB
gro7_grad=G7; // LSB
tro8_grad=tplateau7+2.0*tramp7; // LSB
tro7_grad=tplateau7+2.0*tramp7; // LSB

init_generic(&ro8_grad,"ro8",gro8_grad,tro8_grad); // LSB
init_generic(&ro7_grad,"ro7",gro7_grad,tro7_grad); // LSB

ro8_grad.tramp=tramp7; // LSB
ro7_grad.tramp=tramp7; // LSB
ro8_grad.amp=G8; // LSB
ro7_grad.amp=G7; // LSB
ro8_grad.calcFlag=MOMENT_FROM_DURATION_AMPLITUDE_RAMP; // LSB
ro7_grad.calcFlag=MOMENT_FROM_DURATION_AMPLITUDE_RAMP; // LSB

calc_generic(&ro8_grad,WRITE,"gro8_grad","tro8_grad"); // LSB
```

```
calc_generic(&ro7_grad,WRITE,"gro7_grad","tro7_grad"); // LSB

printf("RO8:␣amp=%f␣␣tramp=%f␣␣dur=%f␣␣m0=%f␣\n", ro8_grad.amp, ro8_grad.tramp, ro8_grad.
    duration, // LSB
       ro8_grad.amp*(-ro8_grad.tramp+ro8_grad.duration)); // LSB
printf("RO7:␣amp=%f␣␣tramp=%f␣␣dur=%f␣␣m0=%f␣\n", ro7_grad.amp, ro7_grad.tramp, ro7_grad.
    duration, // LSB
       ro7_grad.amp*(-ro7_grad.tramp+ro7_grad.duration)); // LSB
printf("ro:␣amp=%f␣␣tramp=%f␣␣timeToEcho=%f␣␣m0=%f␣\n", ro_grad.amp, ro_grad.tramp,
    ro_grad.timeToEcho, // LSB
       ro_grad.amp*(-0.5*ro_grad.tramp+ro_grad.timeToEcho) ); // LSB
printf("Total␣m0␣moment:␣%f␣\n", G8*(-ro8_grad.tramp+ro8_grad.duration) + // LSB
       G7*(-ro7_grad.tramp+ro7_grad.duration) + // LSB
       G9*(-0.5*ro_grad.tramp+ro_grad.timeToEcho) ); // LSB

/* Make sure crushing in PE dimension does not refocus signal from 180 */
crushm0=fabs(gcrush*tcrush);
pem0=0.0; gcrushp=0.0;
if (pecrush) pem0=pe_grad.m0;
calc_dephase(&crush_grad,WRITE,crushm0+pem0,"","");
gcrushr = crush_grad.amp*crushm0/crush_grad.m0;
if (pecrush) gcrushp = crush_grad.amp;
gcrushs = crush_grad.amp*crushm0/crush_grad.m0;

/* Allow phase encode and read dephase to be separated from slice refocus */
if (sepRefocus) { // LSB we have sepRefocus=0
  /* Equalize read dephase and PE gradient durations */
  calc_sim_gradient(&ror_grad,&pe_grad,&null_grad,0,WRITE);
  crushsign=-1;
} else { // LSB sepRefocus=0
  if (slprofile[0] == ’y’) {
    /* Combined slice refocusing and read dephasing,
       reverse gradient sign if ror > ssr integral */
    refsign = (ss_grad.m0ref > ro_grad.m0ref) ? 1.0 : -1.0;
    ss_grad.m0ref -= ro_grad.m0ref;
    calc_slice_refocus(&ssr_grad,&ss_grad,NOWRITE,"gssr");
  }
  /* Equalize both refocus and PE gradient durations */
  calc_sim_gradient(&ror_grad,&pe_grad,&ssr_grad,0,WRITE);
}

/* Create optional prepulse events *******************/
if (sat[0] == ’y’)  create_satbands();
if (fsat[0] == ’y’) create_fatsat();
```

```
if (mt[0] == 'y')   create_mtc();
if (ir[0] == 'y')   create_inversion_recovery();
if (diff[0] == 'y') init_diffusion(&diffusion,&diff_grad,"diff",gdiff,tdelta);

sgl_error_check(sglerror);

/* Min TE ********************************************/
te = granularity(te,2*GRADIENT_RES);
/* tau1, tau2 are the sum of events in each half echo period */
/* tau1, tau2 include a GRADIENT_RES as this is minimum delay time */
tau1 = ss_grad.rfCenterBack + ssr_grad.duration + crush_grad.duration + ss2_grad.
    rfCenterFront + 2*GRADIENT_RES; // LSB see below (my way)
tau2 = ss2_grad.rfCenterBack + crush_grad.duration + ro_grad.timeToEcho + GRADIENT_RES; //
     LSB see below (my way)
if (sepRefocus) tau2 += ror_grad.duration;  // LSB we have sepRefocus=0
temin = 2*MAX(tau1,tau2); // LSB moved down a bit

tau1 = ss_grad.rfCenterBack + ssr1_grad.duration + ssr2_grad.duration + pe_grad.duration +
     fw1_grad.duration + fw2_grad.duration + crush_grad.duration + ss2_grad.rfCenterFront
    + 8*GRADIENT_RES; // LSB

tau2 = ss2_grad.rfCenterBack + crush_grad.duration + fc180l_grad.duration + fc180r_grad.
    duration + ro7_grad.duration + ro8_grad.duration + ro_grad.timeToEcho + 3*GRADIENT_RES
    ; // LSB the right way

temin = 2*MAX(tau1,tau2); // LSB a bit

/* Diffusion ******************************************/
if (diff[0] == 'y') {
  /* granulate tDELTA */
  tDELTA = granularity(tDELTA,GRADIENT_RES);
  /* taudiff is the duration of events between diffusion gradients */
  taudiff = ss2_grad.duration + 2*crush_grad.duration + GRADIENT_RES;
  /* set minimum diffusion structure requirements for gradient echo: taudiff, tDELTA, te
      and minte[0] */
  set_diffusion(&diffusion,taudiff,tDELTA,te,minte[0]);
  /* set additional diffusion structure requirements for spin echo: tau1 and tau2 */
  set_diffusion_se(&diffusion,tau1,tau2);
  /* calculate the diffusion structure delays.
     address &temin is required in order to update temin accordingly */
  calc_diffTime(&diffusion,&temin);
}

/* TE delays ******************************************/
```

```
if (minte[0] == ’y’) {
  te = temin;
  putvalue("te",te);
}
if (FP_LT(te,temin)) {
  abort_message("TE␣too␣short,␣minimum␣TE␣=␣%.3f␣ms\n",temin*1000);
}
te_delay1 = te/2 - tau1 + GRADIENT_RES;
te_delay2 = te/2 - tau2 + GRADIENT_RES;

if (navigator[0] == ’y’) {
  /* tau1, tau2 are the sum of events in each half echo period */
  tau1 = ro_grad.timeFromEcho + pe_grad.duration + crush_grad.duration + ss2_grad.
      rfCenterFront;
  tau2 = ss2_grad.rfCenterBack + crush_grad.duration + ro_grad.timeToEcho;
  if (FP_GT(tau1,tau2)) {
    te_delay3 = GRADIENT_RES;
    te_delay4 = tau1-tau2+GRADIENT_RES;
  } else {
    te_delay3 = tau2-tau1+GRADIENT_RES;
    te_delay4 = GRADIENT_RES;
  }
  navTime = te_delay3 + ss2_grad.duration + 2*crush_grad.duration + ro_grad.duration +
      te_delay4 + 2*GRADIENT_RES;
}

/* Check nsblock, the number of slices blocked together
   (used for triggering and/or inversion recovery) */
check_nsblock();

/* Min TR ********************************************/
trmin = ss_grad.rfCenterFront  + te + ro_grad.timeFromEcho + pe_grad.duration + 2*
    GRADIENT_RES;

/* Increase TR if any options are selected ***********/
if (spoilflag[0] == ’y’) trmin += spoil_grad.duration;
if (navigator[0] == ’y’) trmin += navTime;
if (sat[0] == ’y’)       trmin += satTime;
if (fsat[0] == ’y’)      trmin += fsatTime;
if (mt[0] == ’y’)        trmin += mtTime;
if (ticks > 0)           trmin += GRADIENT_RES;

/* Adjust for all slices *****************************/
trmin *= ns;
```

```
/* Inversion recovery *********************************/
if (ir[0] == 'y') {
  /* tauti is the additional time beyond IR component to be included in ti */
  /* satTime, fsatTime and mtTime all included as those modules will be after IR */
  tauti = satTime + fsatTime + mtTime + GRADIENT_RES + ss_grad.rfCenterFront;
  /* calc_irTime checks ti and returns the time of all IR components */
  trmin += calc_irTime(tauti,trmin,mintr[0],tr,&trtype);
}

if (mintr[0] == 'y') {
  tr = trmin;
  putvalue("tr",tr);
}
if (FP_LT(tr,trmin)) {
  abort_message("TR␣too␣short,␣minimum␣TR␣=␣%.3f␣ms\n",trmin*1000);
}

/* TR delay *******************************************/
tr_delay = granularity((tr-trmin)/ns,GRADIENT_RES);

/* Calculate B values *********************************/
if (ix == 1) {
  /* Calculate bvalues according to main diffusion gradients */
  calc_bvalues(&diffusion,"dro","dpe","dsl");
  /* Add components from additional diffusion encoding imaging gradients peculiar to this
      sequence */
  /* Initialize variables */
  dgro = 0.5*(ror_grad.duration+ro_grad.timeToEcho);
  Gro = ro_grad.m0ref/dgro; Dgro = dgro;
  if (!sepRefocus) Dgro = te-ss_grad.rfCenterBack-ro_grad.timeToEcho; // LSB sepRefocus=0
  dgss = 0.5*(ss_grad.rfCenterBack+ssr_grad.duration);
  Gss = ss_grad.m0ref/dgss; Dgss = dgss;
  dgss2 = ss2_grad.duration/2; Dgss2 = dgss2;
  dcrush = crush_grad.duration-crush_grad.tramp; Dcrush = crush_grad.duration+ss2_grad.
      duration;
  for (i = 0; i < diffusion.nbval; i++)  {
    /* set droval, dpeval and dslval */
    set_dvalues(&diffusion,&droval,&dpeval,&dslval,i);
    /* Readout */
    diffusion.bro[i] += bval(Gro,dgro,Dgro);
    diffusion.bro[i] += bval(crushsign*gcrushr,dcrush,Dcrush);
    diffusion.bro[i] += bval_nested(gdiff*droval,tdelta,tDELTA,crushsign*gcrushr,dcrush,
        Dcrush);
```

```
if (!sepRefocus) {  // LSB sepRefocus=0
  diffusion.bro[i] += bval_nested(Gro,dgro,Dgro,gdiff*droval,tdelta,tDELTA);
  diffusion.bro[i] += bval_nested(Gro,dgro,Dgro,crushsign*gcrushr,dcrush,Dcrush);
}
/* Phase */
if (pecrush) {
  diffusion.bpe[i] += bval(gcrushp,dcrush,Dcrush);
  diffusion.bpe[i] += bval_nested(gdiff*dpeval,tdelta,tDELTA,gcrushp,dcrush,Dcrush);
}
/* Slice */
diffusion.bsl[i] += bval(Gss,dgss,Dgss);
diffusion.bsl[i] += bval(gcrushs,dcrush,Dcrush);
diffusion.bsl[i] += bval(ss2_grad.ssamp,dgss2,Dgss2);
diffusion.bsl[i] += bval_nested(gdiff*dslval,tdelta,tDELTA,gcrushs,dcrush,Dcrush);
diffusion.bsl[i] += bval_nested(gdiff*dslval,tdelta,tDELTA,ss2_grad.ssamp,dgss2,Dgss2)
    ;
diffusion.bsl[i] += bval_nested(gcrushs,dcrush,Dcrush,ss2_grad.ssamp,dgss2,Dgss2);
/* Readout/Phase Cross-terms */
diffusion.brp[i] += bval_cross(gdiff*dpeval,tdelta,tDELTA,crushsign*gcrushr,dcrush,
    Dcrush);
diffusion.brp[i] += bval_cross(gdiff*dpeval,tdelta,tDELTA,crushsign*gcrushr,dcrush,
    Dcrush);
if (pecrush) diffusion.brp[i] += bval_cross(gdiff*droval,tdelta,tDELTA,gcrushp,dcrush,
    Dcrush);
if (!sepRefocus) {  // LSB sepRefocus=0
  diffusion.brp[i] += bval_cross(Gro,dgro,Dgro,gdiff*dpeval,tdelta,tDELTA);
  if (pecrush) diffusion.brp[i] += bval_cross(Gro,dgro,Dgro,gcrushp,dcrush,Dcrush);
}
/* Readout/Slice Cross-terms */
diffusion.brs[i] += bval2(crushsign*gcrushr,gcrushs,dcrush,Dcrush);
diffusion.brs[i] += bval_cross(gdiff*droval,tdelta,tDELTA,gcrushs,dcrush,Dcrush);
diffusion.brs[i] += bval_cross(gdiff*dslval,tdelta,tDELTA,crushsign*gcrushr,dcrush,
    Dcrush);
diffusion.brs[i] += bval_cross(gdiff*droval,tdelta,tDELTA,ss2_grad.ssamp,dgss2,Dgss2);
if (!sepRefocus) {  // LSB sepRefocus=0
  diffusion.brs[i] += bval_cross(Gro,dgro,Dgro,gdiff*dslval,tdelta,tDELTA);
  diffusion.brs[i] += bval_cross(Gro,dgro,Dgro,gcrushs,dcrush,Dcrush);
  diffusion.brs[i] += bval_cross(Gro,dgro,Dgro,ss2_grad.ssamp,dgss2,Dgss2);
}
/* Slice/Phase Cross-terms */
diffusion.bsp[i] += bval_cross(gdiff*dpeval,tdelta,tDELTA,gcrushs,dcrush,Dcrush);
diffusion.bsp[i] += bval_cross(gdiff*dpeval,tdelta,tDELTA,ss2_grad.ssamp,dgss2,Dgss2);
if (pecrush) {
  diffusion.bsp[i] += bval2(gcrushs,gcrushp,dcrush,Dcrush);
```

```
      diffusion.bsp[i] += bval_cross(gdiff*dslval,tdelta,tDELTA,gcrushp,dcrush,Dcrush);
      diffusion.bsp[i] += bval_cross(gcrushp,dcrush,Dcrush,ss2_grad.ssamp,dgss2,Dgss2);
    }
  }  /* End for-all-directions */
  /* Write the values */
  write_bvalues(&diffusion,"bval","bvalue","max_bval");
}

/* Generate phase-ramped pulses **********************/
offsetlist(pss,ss_grad.ssamp,0,freq90,ns,seqcon[1]);
offsetlist(pss,ss2_grad.ssamp,0,freq180,ns,seqcon[1]);
shape90 = shapelist(p1_rf.pulseName,ss_grad.rfDuration,freq90,ns,ss_grad.rfFraction,seqcon
    [1]);
shape180 = shapelist(p2_rf.pulseName,ss2_grad.rfDuration,freq180,ns,ss2_grad.rfFraction,
    seqcon[1]);

/* Set pe_steps for profile or full image *************/
pe_steps = prep_profile(profile[0],nv,&pe_grad,&null_grad);
F_initval(pe_steps/2.0,vpe_offset);

/* Shift DDR for pro *********************************/
roff = -poffset(pro,ro_grad.roamp);

/* Adjust experiment time for VnmrJ ******************/
if (ssc<0) {
  if (seqcon[2] == 'c') g_setExpTime(trmean*(ntmean*pe_steps*arraydim - ssc*arraydim));
  else g_setExpTime(trmean*(ntmean*pe_steps*arraydim - ssc*pe_steps*arraydim));
}
else g_setExpTime(trmean*ntmean*pe_steps*arraydim + tr*ssc);

/* Slice profile *************************************/
if (slprofile[0] == 'y' && !sepRefocus) ror_grad.amp = 0;  // LSB sepRefocus=0

/* Set phase cycle table *****************************/
if (sepRefocus) settable(t2,1,ph180); // Phase encode is just before readout  // LSB we
    have sepRefocus=0
else settable(t2,2,ph180);  // LSB sepRefocus=0

/* PULSE SEQUENCE ************************************/
status(A);                           // Set status A
rotate();                            // Set gradient rotation according to psi, phi and
    theta
triggerSelect(trigger);              // Select trigger input 1/2/3
obsoffset(resto);                    // Set spectrometer frequency
```

```
delay(GRADIENT_RES);                // Delay for frequency setting
initval(fabs(ssc),vssc);            // Compressed steady-state counter
if (seqcon[2]=='s') assign(zero,vssc); // Zero for standard peloop
assign(one,vacquire);               // real-time acquire flag
setacqvar(vacquire);                // Turn on acquire when vacquire is zero

/* trigger */
if (ticks > 0) F_initval((double)nsblock,vtrigblock);

/* Begin phase-encode loop ****************************/
peloop(seqcon[2],pe_steps,vpe_steps,vpe_ctr);

  if (trtype) delay(ns*tr_delay);   // relaxation delay

  /* Compressed steady-states: 1st array & transient, all arrays if ssc is negative */
  if ((ix > 1) && (ssc > 0))
    assign(zero,vssc);
  sub(vpe_ctr,vssc,vpe_ctr);        // vpe_ctr counts up from -ssc
  assign(zero,vssc);
  if (seqcon[2] == 's')
    assign(zero,vacquire);          // Always acquire for non-compressed loop
  else {
    ifzero(vpe_ctr);
      assign(zero,vacquire);        // Start acquiring when vpe_ctr reaches zero
    endif(vpe_ctr);
  }

  /* Read external kspace table if set *****************/
  if (table)
    getelem(t1,vpe_ctr,vpe_mult);
  else {
    ifzero(vacquire);
      sub(vpe_ctr,vpe_offset,vpe_mult);
    elsenz(vacquire);
      sub(zero,vpe_offset,vpe_mult);      // Hold PE mult at initial value for steady
          states
    endif(vacquire);
  }

  /* Phase cycle *****************************************/
  getelem(t2,vpe_ctr,vph180);             // For phase encoding with slice rephase
  add(oph,vph180,vph180);                 // 180 deg pulse phase alternates +/- 90 from
      receiver
  mod2(ct,vph2);
```

```
dbl(vph2,vph2);
add(vph180,vph2,vph180);                // Alternate phase for 180 on odd transients

/* Begin multislice loop *****************************/
msloop(seqcon[1],ns,vms_slices,vms_ctr);

  if (!trtype) delay(tr_delay);         // Relaxation delay

  if (ticks > 0) {
    modn(vms_ctr,vtrigblock,vtest);
    ifzero(vtest);                      // if the beginning of an trigger block
      xgate(ticks);
      grad_advance(gpropdelay);
      delay(GRADIENT_RES);
    elsenz(vtest);
      delay(GRADIENT_RES);
    endif(vtest);
  }

  sp1on(); delay(GRADIENT_RES); sp1off();     // Scope trigger

  /* Prepulse options ***********************************/
  if (ir[0] == ’y’)   inversion_recovery();
  if (sat[0] == ’y’)  satbands();
  if (fsat[0] == ’y’) fatsat();
  if (mt[0] == ’y’)   mtc();

  /* Slice select RF pulse *****************************/
  obspower(p1_rf.powerCoarse);
  obspwrf(p1_rf.powerFine);
  delay(GRADIENT_RES);
  obl_shapedgradient(ss_grad.name,ss_grad.duration,0,0,ss_grad.amp,NOWAIT);
  delay(ss_grad.rfDelayFront);
  shapedpulselist(shape90,ss_grad.rfDuration,oph,rof1,rof2,seqcon[1],vms_ctr);
  delay(ss_grad.rfDelayBack);

  // LSB flow comp ss refocus
  delay(GRADIENT_RES); // LSB
  obl_shapedgradient(ssr1_grad.name,ssr1_grad.duration,0,0,G2,WAIT); // LSB
  delay(GRADIENT_RES); // LSB
  obl_shapedgradient(ssr2_grad.name,ssr2_grad.duration,0,0,G3,WAIT); // LSB
  delay(GRADIENT_RES); // LSB

  /* Slice refocus gradient ****************************/
```

```
if (sepRefocus)  // LSB we have sepRefocus=0
  obl_shapedgradient(ssr_grad.name,ssr_grad.duration,0,0,-ssr_grad.amp,WAIT);
else {  // LSB sepRefocus=0
  /* Include phase encode and readout dephase gradient if refocus gradients not
      separated */
  //        pe_shapedgradient(pe_grad.name,pe_grad.duration,ror_grad.amp,0,-ssr_grad.
      amp*refsign,pe_grad.increment,vpe_mult,WAIT); // LSB
  pe_shapedgradient(pe_grad.name,pe_grad.duration,0,0,0,pe_grad.increment,vpe_mult,
      WAIT); // LSB
}

// LSB bipolar flow weighting grad
delay(GRADIENT_RES); // LSB
obl_shapedgradient(fw1_grad.name,fw1_grad.duration,fwampx,fwampy,fwampz,WAIT);  // LSB
// LSB bipolar flow weighting grad
delay(GRADIENT_RES);
obl_shapedgradient(fw2_grad.name,fw2_grad.duration,-fwampx,-fwampy,-fwampz,WAIT);

if (diff[0] == 'y') {
  delay(diffusion.d1);
  diffusion_dephase(&diffusion,dro,dpe,dsl);
  delay(diffusion.d2);
}
else
  delay(te_delay1);

/* Refocusing RF pulse ********************************/ // with crushers
obspower(p2_rf.powerCoarse);
obspwrf(p2_rf.powerFine);
delay(GRADIENT_RES);
obl_shapedgradient(crush_grad.name,crush_grad.duration,crushsign*gcrushr,gcrushp,
    gcrushs,WAIT);
obl_shapedgradient(ss2_grad.name,ss2_grad.duration,0,0,ss2_grad.amp,NOWAIT);
delay(ss2_grad.rfDelayFront);
shapedpulselist(shape180,ss2_grad.rfDuration,vph180,rof2,rof2,seqcon[1],vms_ctr);
delay(ss2_grad.rfDelayBack);
obl_shapedgradient(crush_grad.name,crush_grad.duration,crushsign*gcrushr,gcrushp,
    gcrushs,WAIT);

// LSB 180 flow comp bipolar
delay(GRADIENT_RES); // LSB
obl_shapedgradient(fc180l_grad.name,fc180l_grad.duration,0,0,-G10,WAIT); // LSB
delay(GRADIENT_RES); // LSB
obl_shapedgradient(fc180r_grad.name,fc180r_grad.duration,0,0,G10,WAIT); // LSB
```

```
if (diff[0] == 'y') {
  delay(diffusion.d3);
  diffusion_rephase(&diffusion,dro,dpe,dsl);
  delay(diffusion.d4);
}
else
  delay(te_delay2);

 // LSB flow comp ro grad
obl_shapedgradient(ro8_grad.name,ro8_grad.duration,G8,0,0,WAIT); // LSB
  // LSB flow comp ro grad
delay(GRADIENT_RES); // LSB
obl_shapedgradient(ro7_grad.name,ro7_grad.duration,G7,0,0,WAIT); // LSB

/* Readout dephase, phase encode & readout gradients **/
roff = -poffset(pro,ro_grad.roamp);  // incase inverted navigator is acquired
if (slprofile[0] == 'y') {
  /* Readout gradient only if refocus gradients not separated */
  if (sepRefocus)   // LSB we have sepRefocus=0
    obl_shapedgradient(ror_grad.name,ror_grad.duration,0,0,-ror_grad.amp,WAIT);
  obl_shapedgradient(ro_grad.name,ro_grad.duration,0,0,ro_grad.amp,NOWAIT);   // LSB
      sepRefocus=0
} else {
  /* Readout gradient only if refocus gradients not separated */
  if (sepRefocus)   // LSB we have sepRefocus=0
    pe_shapedgradient(pe_grad.name,pe_grad.duration,-ror_grad.amp,0,0,-pe_grad.
        increment,vpe_mult,WAIT);
  obl_shapedgradient(ro_grad.name,ro_grad.duration,ro_grad.amp,0,0,NOWAIT);   // LSB
      sepRefocus=0
}

/* Acquisition ****************************************/
delay(ro_grad.atDelayFront-alfa);
startacq(alfa);
acquire(np,1.0/sw);
delay(ro_grad.atDelayBack);
endacq();

/* Rewind Phase encoding ******************************/
//      pe_shapedgradient(pe_grad.name,pe_grad.duration,0,0,0,pe_grad.increment,
    vpe_mult,WAIT); // LSB
obl_shapedgradient(spoil_grad.name,spoil_grad.duration,spoil_grad.amp,spoil_grad.amp,
    spoil_grad.amp,WAIT);
```

```
      /* Navigator acquisition ******************************/
      if (navigator[0] == 'y') {
        delay(te_delay3);
        obl_shapedgradient(crush_grad.name,crush_grad.duration,-crushsign*gcrushr,0,-gcrushs
            ,WAIT);
        obl_shapedgradient(ss2_grad.name,ss2_grad.duration,0,0,ss2_grad.amp,NOWAIT);
        delay(ss2_grad.rfDelayFront);
        shapedpulselist(shape180,ss2_grad.rfDuration,vph180,rof2,rof2,seqcon[1],vms_ctr);
        delay(ss2_grad.rfDelayBack);
        obl_shapedgradient(crush_grad.name,crush_grad.duration,-crushsign*gcrushr,0,-gcrushs
            ,WAIT);
        delay(te_delay4);
        obl_shapedgradient(ro_grad.name,ro_grad.duration,navsign*ro_grad.amp,0,0,NOWAIT);
        delay(ro_grad.atDelayFront-alfa);
        startacq(alfa);
        acquire(np,1.0/sw);
        delay(ro_grad.atDelayBack);
        endacq();
      }

      if (spoilflag[0] == 'y') {
        obl_shapedgradient(spoil_grad.name,spoil_grad.duration,navsign*spoil_grad.amp,0,
            spoil_grad.amp,WAIT);
      }

    endmsloop(seqcon[1],vms_ctr);

  endpeloop(seqcon[2],vpe_ctr);

  /* Inter-image delay **********************************/
  sub(ntrt,ct,vtrimage);
  decr(vtrimage);
  ifzero(vtrimage);
    delay(trimage);
  endif(vtrimage);

  /* Duty cycle *****************************************/
  calc_grad_duty(tr);

}
```

References

[1] E. Stejskal and J. Tanner, “Spin diffusion measurements: spin echoes in the presence of a time-dependent field gradient,” *J. Chem. Phys.*, vol. 42, no. 1, pp. 288–292, 1965.

[2] P. T. Callaghan, *Principles of Nuclear Magnetic Resonance Microscopy.* Clarendon Press, 1991.

[3] P. T. Callaghan, *Translational Dynamics and Magnetic Resonance: Principles of Pulsed Gradient Spin Echo NMR.* Oxford University Press, 2011.

[4] N. N. Jarenwattananon and L.-S. Bouchard, “Motional averaging of nuclear resonance in a field gradient,” *Phys. Rev. Lett.*, vol. 114, no. 19, p. 197601, 2015.

[5] N. N. Jarenwattananon, S. Glöggler, T. Otto, A. Melkonian, W. Morris, S. R. Burt, O. M. Yaghi, and L.-S. Bouchard, “Thermal maps of gases in heterogeneous reactions,” *Nature*, vol. 502, no. 7472, pp. 537–540, 2013.

[6] N. N. Jarenwattananon and L.-S. Bouchard, “Erratum: Motional averaging of nuclear resonance in a field gradient [phys. rev. lett. 114, 197601 (2015)],” *Phys. Rev. Lett.*, vol. 116, no. 21, p. 219903, 2016.

[7] N. N. Jarenwattananon and L.-S. Bouchard, “Jarenwattananon and bouchard reply,” *Phys. Rev. Lett.*, vol. 117, no. 24, p. 249702, 2016.

[8] R. R. Edelman and S. Warach, “Magnetic resonance imaging,” *N. Engl. J. Med.*, vol. 328, no. 10, pp. 708–716, 1993.

[9] M. A. Foster, *Magnetic Resonance in Medicine and Biology.* Pergamon Press, 1984.

[10] E. M. Haacke, R. W. Brown, M. R. Thompson, and R. Venkatesan, *Magnetic Resonance Imaging: Physical Principles and Sequence Design*, vol. 82. Wiley New York:, 1999.

[11] S. Stapf and S.-I. Han, *NMR imaging in chemical engineering.* John Wiley & Sons, 2006.

[12] A. T. Bell, *NMR Techniques in Catalysis*, vol. 55. CRC Press, 1994.

[13] A. E. Derome, *Modern NMR Techniques for Chemistry Research*, vol. 6 of *Organic Chemistry.* Elsevier, 2013.

[14] H. Günther, *NMR Spectroscopy: Basic Principles, Concepts and Applications in Chemistry.* John Wiley & Sons, 2013.

[15] C. A. Fyfe, *Solid state NMR for Chemists.* CFC Press, 1983.

[16] G. K. McMillan, D. M. Considine, *et al.*, *Process/Industrial Instruments and Controls Handbook*, vol. 7. McGraw Hill, 1999.

[17] L. M. Vandersypen and I. L. Chuang, “Nmr techniques for quantum control and computation,” *Rev. Mod. Phys.*, vol. 76, no. 4, p. 1037, 2005.

[18] J. Ø. Duus, C. H. Gotfredsen, and K. Bock, “Carbohydrate structural determination by nmr spectroscopy: modern methods and limitations,” *Chem. Rev.*, vol. 100, no. 12, pp. 4589–4614, 2000.

[19] W. Wolf, M. J. Albright, M. S. Silver, H. Weber, U. Reichardt, and R. Sauer, “Fluorine-19 nmr spectroscopic studies of the metabolism of 5-fluorouracil in the liver of patients undergoing chemotherapy,” *Magnetic resonance imaging*, vol. 5, no. 3, pp. 165–169, 1987.

[20] Y. Cohen, L. Avram, and L. Frish, “Diffusion nmr spectroscopy in supramolecular and combinatorial chemistry: An old parameter–new insights,” *Angew. Chem. Int. Ed.*, vol. 44, no. 4, pp. 520–554, 2005.

[21] E. G. Stein, L. M. Rice, and A. T. Brünger, “Torsion-angle molecular dynamics as a new efficient tool for nmr structure calculation,” *J. Magn. Reson.*, vol. 124, no. 1, pp. 154–164, 1997.

[22] C. Siciliano, E. Belsito, R. De Marco, M. L. Di Gioia, A. Leggio, and A. Liguori, “Quantitative determination of fatty acid chain composition in pork meat products by high resolution 1 h nmr spectroscopy,” *Food Chem.*, vol. 136, no. 2, pp. 546–554, 2013.

[23] P. J. Hore, *Nuclear Magnetic Resonance.* Oxford University Press, 1995.

[24] P. J. Hore, J. A. Jones, and S. Wimperis, *NMR: The Toolkit.* Oxford University Press, 2001.

[25] C. P. Slichter, *Principles of Magnetic Resonance.* Sl, 1990.

[26] M. H. Levitt, *Spin dynamics: basics of nuclear magnetic resonance.* John Wiley & Sons, 2001.

[27] A. Abragam, “Principles of nuclear magnetism (international series of monographs on physics),” 1961.

[28] E. Bodenhausen and A. Wokaun, *Principles of Nuclear Magnet Resonance in One and Two Dimensions.* Oxford, 1987.

[29] J. Keeler, *Understanding NMR spectroscopy.* John Wiley & Sons, 2011.

[30] D. G. Nishimura, *Principles of magnetic resonance imaging.* Stanford University, 1996.

[31] A. L. Horowitz, *MRI physics for radiologists.* Springer, 1995.

[32] M. Hollewand and L. Gladden, “Heterogeneities in structure and diffusion within porous catalyst support pellets observed by {NMR} imaging,” *J. Catal.*, vol. 144, no. 1, pp. 254 – 272, 1993.

[33] L. F. Gladden, "Applications of in situ magnetic resonance techniques in chemical reaction engineering," *Top. Catal.*, vol. 8, no. 1-2, pp. 87–95, 1999.

[34] L.-S. Bouchard, S. R. Burt, M. S. Anwar, K. V. Kovtunov, I. V. Koptyug, and A. Pines, "Nmr imaging of catalytic hydrogenation in microreactors with the use of para-hydrogen," *Science*, vol. 319, no. 5862, pp. 442–445, 2008.

[35] A. A. Lysova and I. V. Koptyug, "Magnetic resonance imaging methods for in situ studies in heterogeneous catalysis," *Chem. Soc. Rev.*, vol. 39, no. 12, pp. 4585–4601, 2010.

[36] G. A. Somorjai and Y. Li, *Introduction to surface chemistry and catalysis.* John Wiley & Sons, 2010.

[37] G. Ertl, H. Knözinger, and J. Weitkamp, *Handbook of heterogeneous catalysis.* VCH Weinheim, 1997.

[38] J. R. Ross, *Heterogeneous catalysis: fundamentals and applications.* Elsevier, 2011.

[39] M. Schmal, *Heterogeneous Catalysis and Its Industrial Applications.* Springer, 2016.

[40] E. L. Hahn, "Spin echoes," *Phys. Rev.*, vol. 80, no. 4, p. 580, 1950.

[41] H. Y. Carr and E. M. Purcell, "Effects of diffusion on free precession in nuclear magnetic resonance experiments," *Phys. Rev.*, vol. 94, no. 3, p. 630, 1954.

[42] S. Meiboom and D. Gill, "Modified spin-echo method for measuring nuclear relaxation times," *Rev. Sci. Instrum.*, vol. 29, no. 8, pp. 688–691, 1958.

[43] J. E. Tanner, "Use of the stimulated echo in nmr diffusion studies," *The Journal of Chemical Physics*, vol. 52, no. 5, pp. 2523–2526, 1970.

[44] R. Cotts, M. Hoch, T. Sun, and J. Markert, "Pulsed field gradient stimulated echo methods for improved nmr diffusion measurements in heterogeneous systems," *Journal of Magnetic Resonance (1969)*, vol. 83, no. 2, pp. 252–266, 1989.

[45] S. R. De Groot and P. Mazur, *Non-equilibrium thermodynamics.* Courier Corporation, 2013.

[46] W. Jäger, R. Rannacher, and J. Warnatz, *Reactive flows, diffusion and transport.* Springer, 2007.

[47] K. S. Førland and T. Førland, *Irreversible thermodynamics: theory and applications.* John Wiley & Sons Inc, 1988.

[48] O. Inderwildi, D. Starukhin, H.-R. Volpp, D. Lebiedz, O. Deutschmann, and J. Warnatz, "Reaction processes on catalytically active surfaces," in *Reactive Flows, Diffusion and Transport*, pp. 311–340, Springer, 2007.

[49] A. Hanf, H.-R. Volpp, and J. Wolfrum, “Determination of kinetic parameters in laminar flow reactors. ii. experimental aspects,” in *Reactive Flows, Diffusion and Transport*, pp. 251–289, Springer, 2007.

[50] H. Bock, O. Deutschmann, S. Körkel, L. Maier, H. Minh, J. Schlöder, S. Tischer, and J. Warnatz, “Optimization of reactive flows in a single channel of a catalytic monolith: Conversion of ethane to ethylene,” *Reactive Flows, Diffusion and Transport*, pp. 291–310, 2007.

[51] J. Hagen, *Industrial Catalysis: A Practical Approach.* John Wiley & Sons, 2015.

[52] I. Chorkendorff and J. W. Niemantsverdriet, *Concepts of modern catalysis and kinetics.* John Wiley & Sons, 2006.

[53] G. Rothenberg, *Catalysis: Concepts and Green Applications.* John Wiley & Sons, 2015.

[54] H. F. Rase, *Handbook of commercial catalysts: heterogeneous catalysts.* CRC Press, 2000.

[55] R. Schwiedernoch, S. Tischer, O. Deutschmann, and J. Warnatz, “Experimental and numerical investigation of the ignition of methane combustion in a platinum-coated honeycomb monolith,” *Proc. Comb. Inst.*, vol. 29, no. 1, pp. 1005–1011, 2002.

[56] I. L. Buurmans and B. M. Weckhuysen, “Heterogeneities of individual catalyst particles in space and time as monitored by spectroscopy,” *Nature Chem.*, vol. 4, no. 11, pp. 873–886, 2012.

[57] E. de Smit *et al.*, “Nanoscale chemical imaging of a working catalyst by scanning transmission x-ray microscopy,” *Nature*, vol. 456, no. 7219, pp. 222–225, 2008.

[58] R. Horn, O. Korup, M. Geske, U. Zavyalova, I. Oprea, and R. Schlögl, “Reactor for in situ measurements of spatially resolved kinetic data in heterogeneous catalysis,” *Rev. Sci. Instrum.*, vol. 81, no. 6, p. 064102, 2010.

[59] T. Schwalbe, V. Autze, and G. Wille, “Chemical synthesis in microreactors,” *CHIMIA International Journal for Chemistry*, vol. 56, no. 11, pp. 636–646, 2002.

[60] P. Watts, “Chemical synthesis in micro reactors,” *Chemie Ingenieur Technik*, vol. 76, no. 5, pp. 555–559, 2004.

[61] P. Watts and S. J. Haswell, “Chemical synthesis in microreactors,” *Microengineering in Biotechnology*, pp. 109–120, 2010.

[62] J. P. McMullen and K. F. Jensen, “Integrated microreactors for reaction automation: new approaches to reaction development,” *Annual review of analytical chemistry*, vol. 3, pp. 19–42, 2010.

[63] T. R. Dietrich, A. Freitag, and R. Scholz, "Production and characteristics of microreactors made from glass," *Chemical engineering & technology*, vol. 28, no. 4, pp. 477–483, 2005.

[64] B. Ahmed-Omer, J. C. Brandt, and T. Wirth, "Advanced organic synthesis using microreactor technology," *Organic & biomolecular chemistry*, vol. 5, no. 5, pp. 733–740, 2007.

[65] A. R. Bogdan, B. P. Mason, K. T. Sylvester, and D. T. McQuade, "Improving solid-supported catalyst productivity by using simplified packed-bed microreactors," *Angewandte Chemie International Edition*, vol. 46, no. 10, pp. 1698–1701, 2007.

[66] J. Kobayashi, Y. Mori, K. Okamoto, R. Akiyama, M. Ueno, T. Kitamori, and S. Kobayashi, "A microfluidic device for conducting gas-liquid-solid hydrogenation reactions," *Science*, vol. 304, no. 5675, pp. 1305–1308, 2004.

[67] B. M. Weckhuysen, "Chemical imaging of spatial heterogeneities in catalytic solids at different length and time scales," *Angew. Chem. Int. Ed.*, vol. 48, no. 27, pp. 4910–4943, 2009.

[68] M. Tada, Y. Akatsuka, Y. Yang, T. Sasaki, M. Kinoshita, K. Motokura, and Y. Iwasawa, "Photoinduced reversible structural transformation and selective oxidation catalysis of unsaturated ruthenium complexes supported on sio2," *Angewandte Chemie International Edition*, vol. 47, no. 48, pp. 9252–9255, 2008.

[69] F. Meunier, D. Reid, A. Goguet, S. Shekhtman, C. Hardacre, R. Burch, W. Deng, and M. Flytzani-Stephanopoulos, "Quantitative analysis of the reactivity of formate species seen by drifts over a au/ce (la) o 2 water–gas shift catalyst: first unambiguous evidence of the minority role of formates as reaction intermediates," *J. Catal.*, vol. 247, no. 2, pp. 277–287, 2007.

[70] P. Van Der Voort, P. Ravikovitch, K. De Jong, A. Neimark, A. Janssen, M. Benjelloun, E. Van Bavel, P. Cool, B. Weckhuysen, and E. Vansant, "Plugged hexagonal templated silica: a unique micro-and mesoporous composite material with internal silica nanocapsules," *Chem. Comm.*, vol. 9, pp. 1010–1011, 2002.

[71] M. Hunger and J. Weitkamp, "In situ ir, nmr, epr, and uv/vis spectroscopy: Tools for new insight into the mechanisms of heterogeneous catalysis," *Angew. Chem. Int. Ed.*, vol. 40, no. 16, pp. 2954–2971, 2001.

[72] J. M. Thomas, "Design, synthese und in-situ-charakterisierung neuer feststoffkatalysatoren," *Angew. Chem.*, vol. 111, no. 24, pp. 3800–3843, 1999.

[73] J. M. Thomas, C. R. A. Catlow, and G. Sankar, "Determining the structure of active sites, transition states and intermediates in heterogeneously catalysed reactions," *Chem. Comm.*, pp. 2921–2925, 2002.

[74] J. W. Niemantsverdriet, *Spectroscopy in catalysis.* John Wiley & Sons, 2007.

[75] J. F. Haw, *In situ Spectroscopy in Heterogeneous Catalysis.* Wiley Online Library, 1994.

[76] B. M. Weckhuysen, *In-situ Spectroscopy of Catalysts*, vol. 255. American Scientific Publishers Stevenson Ranch, CA, 2004.

[77] A. Urakawa and A. Baiker, "Space-resolved profiling relevant in heterogeneous catalysis," *Top. Catal.*, vol. 52, no. 10, pp. 1312–1322, 2009.

[78] H. Jeziorowski and H. Knoezinger, "Raman and ultraviolet spectroscopic characterization of molybdena on alumina catalysts," *J. Phys. Chem.*, vol. 83, no. 9, pp. 1166–1173, 1979.

[79] E. M. van Schrojenstein Lantman, T. Deckert-Gaudig, A. J. Mank, V. Deckert, and B. M. Weckhuysen, "Catalytic processes monitored at the nanoscale with tip-enhanced raman spectroscopy," *Nature Nanotechnol.*, vol. 7, no. 9, pp. 583–586, 2012.

[80] S. Tinnemans, M. Kox, T. Nijhuis, T. Visser, and B. Weckhuysen, "Real time quantitative raman spectroscopy of supported metal oxide catalysts without the need of an internal standard," *Phys. Chem. Chem. Phys.*, vol. 7, no. 1, pp. 211–216, 2005.

[81] S. J. Taylor and J. P. Morken, "Thermographic selection of effective catalysts from an encoded polymer-bound library," *Science*, vol. 280, no. 5361, pp. 267–270, 1998.

[82] O. Korup, S. Mavlyankariev, M. Geske, C. F. Goldsmith, and R. Horn, "Measurement and analysis of spatial reactor profiles in high temperature catalysis research," *Chem. Eng. Process.*, vol. 50, no. 10, pp. 998–1009, 2011.

[83] T. Dietrich, *Microchemical Engineering in Practice.* John Wiley & Sons, 2011.

[84] K. Jensen, I.-M. Hsing, R. Srinivasan, M. Schmidt, M. Harold, J. Lerou, and J. Ryley, "Reaction engineering for microreactor systems," in *Microreaction Technology*, pp. 2–9, Springer, 1998.

[85] J.-D. Grunwaldt and A. Baiker, "Axial variation of the oxidation state of pt-rh/al 2 o 3 during partial methane oxidation in a fixed-bed reactor: An in situ x-ray absorption spectroscopy study," *Catal. Lett.*, vol. 99, no. 1, pp. 5–12, 2005.

[86] P. M. Bertsch and D. B. Hunter, "Applications of synchrotron-based x-ray microprobes," *Chem. Rev.*, vol. 101, no. 6, pp. 1809–1842, 2001.

[87] C. Rau, A. Somogyi, and A. Simionovici, "Microimaging and tomography with chemical speciation," *Nucl. Instrum. Meth. B*, vol. 200, pp. 444–450, 2003.

[88] R. Horn, K. Williams, N. Degenstein, and L. Schmidt, "Syngas by catalytic partial oxidation of methane on rhodium: Mechanistic conclusions from spatially resolved measurements and numerical simulations," *J. Catal.*, vol. 242, no. 1, pp. 92–102, 2006.

[89] J.-S. Choi, W. P. Partridge, and C. S. Daw, “Spatially resolved in situ measurements of transient species breakthrough during cyclic, low-temperature regeneration of a monolithic pt/k/al 2 o 3 no x storage-reduction catalyst,” *Appl. Catal. A.*, vol. 293, pp. 24–40, 2005.

[90] S. Lundgren, K.-E. Keck, and B. Kasemo, “A flow reactor system for catalytic reaction studies, allowing time-and space-resolved measurements of gas composition and temperature around the catalyst,” *Rev. Sci. Instrum.*, vol. 65, no. 8, pp. 2696–2703, 1994.

[91] I. V. Koptyug, A. A. Lysova, R. Z. Sagdeev, V. A. Kirillov, A. V. Kulikov, and V. N. Parmon, “In situ mri of the structure and function of multiphase catalytic reactors,” *Catal. Today*, vol. 105, no. 3, pp. 464–468, 2005.

[92] I. V. Koptyug, A. A. Lysova, R. Z. Sagdeev, and V. N. Parmon, “Application of multinuclear mri and solid state mri in heterogeneous catalysis,” *Catalysis Today*, vol. 126, no. 1, pp. 37–43, 2007.

[93] L. F. Gladden, M. D. Mantle, and A. J. Sederman, “Chemical mapping of chemical conversion in heterogeneous catalytic reactors using mri,” *Catalysis*, vol. 20, pp. 286–308, 2007.

[94] M. Hollewand and L. Gladden, “Heterogeneities in structure and diffusion within porous catalyst support pellets observed by nmr imaging,” *J. Catal.*, vol. 144, no. 1, pp. 254–272, 1993.

[95] J. Timonen, L. Alvila, P. Hirva, T. Pakkanen, D. Gross, and V. Lehmann, “Nmr imaging of aluminum oxide catalyst spheres,” *Appl. Catal. A*, vol. 129, no. 1, pp. 117–123, 1995.

[96] S. Rigby, K. Cheah, and L. Gladden, “Nmr imaging studies of transport heterogeneity and anisotropic diffusion in porous alumina pellets,” *Appl. Catal. A*, vol. 144, no. 1-2, pp. 377–388, 1996.

[97] K. Y. Cheah, N. Chiaranussati, M. P. Hollewand, and L. F. Gladden, “Coke profiles in deactivated alumina pellets studied by nmr imaging,” *Appl. Catal. A*, vol. 115, no. 1, pp. 147–155, 1994.

[98] I. V. Koptyug, A. V. Khomichev, A. A. Lysova, and R. Z. Sagdeev, “Spatially resolved nmr thermometry of an operating fixed-bed catalytic reactor,” *J. Am. Chem. Soc.*, vol. 130, no. 32, pp. 10452–10453, 2008.

[99] S. P. Rigby and L. F. Gladden, “The use of magnetic resonance images in the simulation of diffusion in porous catalyst support pellets,” *J. Catal.*, vol. 173, no. 2, pp. 484–489, 1998.

[100] U. Tallarek, D. Van Dusschoten, H. Van As, E. Bayer, and G. Guiochon, “Study of transport phenomena in chromatographic columns by pulsed field gradient nmr,” *J. Phys. Chem. B*, vol. 102, no. 18, pp. 3486–3497, 1998.

[101] U. Tallarek, F. J. Vergeldt, and H. V. As, "Stagnant mobile phase mass transfer in chromatographic media: intraparticle diffusion and exchange kinetics," *J. Phys. Chem. B*, vol. 103, no. 36, pp. 7654–7664, 1999.

[102] J. A. Bergwerff, A. A. Lysova, L. Espinosa-Alonso, I. V. Koptyug, and B. M. Weckhuysen, "Monitoring transport phenomena of paramagnetic metal-ion complexes inside catalyst bodies with magnetic resonance imaging," *Chem. Eur. J.*, vol. 14, no. 8, pp. 2363–2374, 2008.

[103] I. V. Koptyug, S. A. Altobelli, E. Fukushima, A. V. Matveev, and R. Z. Sagdeev, "Thermally polarized 1h nmr microimaging studies of liquid and gas flow in monolithic catalysts," *J. Magn. Reson.*, vol. 147, no. 1, pp. 36–42, 2000.

[104] M. Johns, A. Sederman, A. Bramley, L. Gladden, and P. Alexander, "Local transitions in flow phenomena through packed beds identified by mri," *AIChE J.*, vol. 46, no. 11, pp. 2151–2161, 2000.

[105] J. A. Bergwerff, A. A. Lysova, L. Espinosa Alonso, I. V. Koptyug, and B. M. Weckhuysen, "Probing the transport of paramagnetic complexes inside catalyst bodies in a quantitative manner by magnetic resonance imaging," *Angew. Chem. Int. Ed.*, vol. 46, no. 38, pp. 7224–7227, 2007.

[106] A. A. Lysova, I. V. Koptyug, R. Z. Sagdeev, V. N. Parmon, J. A. Bergwerff, and B. M. Weckhuysen, "Noninvasive in situ visualization of supported catalyst preparations using multinuclear magnetic resonance imaging," *Journal of the American Chemical Society*, vol. 127, no. 34, pp. 11916–11917, 2005.

[107] L. Y. Khitrina, I. Koptyug, N. Pakhomov, R. Sagdeev, and V. Parmon, "An 1h nmr microimaging visualization of hexachloroplatinate dianion redistribution within a porous γ-al2o3 pellet in the course of supported catalyst preparation," *J. Phys. Chem. B*, vol. 104, no. 9, pp. 1966–1970, 2000.

[108] E. Yuen, A. J. Sederman, and L. F. Gladden, "In situ magnetic resonance visualisation of the spatial variation of catalytic conversion within a fixed-bed reactor," *Appl. Catal. A*, vol. 232, no. 1, pp. 29–38, 2002.

[109] A. Heibel, T. Scheenen, J. Heiszwolf, H. Van As, F. Kapteijn, and J. Moulijn, "Gas and liquid phase distribution and their effect on reactor performance in the monolith film flow reactor," *Chemi. Eng. Sci.*, vol. 56, no. 21, pp. 5935–5944, 2001.

[110] A. Sederman and L. Gladden, "Magnetic resonance imaging as a quantitative probe of gas–liquid distribution and wetting efficiency in trickle-bed reactors," *Chemi. Eng. Sci.*, vol. 56, no. 8, pp. 2615–2628, 2001.

[111] P. A. Beckmann and C. Dybowski, "A thermometer for nonspinning solid-state nmr spectroscopy," *J. Magn. Reson.*, vol. 146, no. 2, pp. 379–380, 2000.

[112] C. Ammann, P. Meier, and A. Merbach, "A simple multinuclear nmr thermometer," *J. Magn. Reson.*, vol. 46, no. 2, pp. 319–321, 1982.

[113] G. Galiana, R. T. Branca, E. R. Jenista, and W. S. Warren, "Accurate temperature imaging based on intermolecular coherences in magnetic resonance," *Science*, vol. 322, no. 5900, pp. 421–424, 2008.

[114] A. Webb, "Temperature measurements using nuclear magnetic resonance," *Annual Reports on NMR Spectroscopy*, vol. 45, pp. 1–67, 2002.

[115] P. T. Callaghan, A. Coy, D. MacGowan, K. J. Packer, and F. O. Zelaya, "Diffraction-like effects in nmr diffusion studies of fluids in porous solids," *Nature*, vol. 351, pp. 467–469, 06 1991.

[116] D. Le Bihan, "Looking into the functional architecture of the brain with diffusion mri," *Nat. Rev. Neurosci.*, vol. 4, pp. 469–480, 06 2003.

[117] N. Bloembergen, E. M. Purcell, and R. V. Pound, "Relaxation effects in nuclear magnetic resonance absorption," *Phys. Rev.*, vol. 73, no. 7, p. 679, 1948.

[118] H. C. Torrey, "Bloch equations with diffusion terms," *Phys. Rev.*, vol. 104, no. 3, p. 563, 1956.

[119] R. Kubo and K. Tomita, "A general theory of magnetic resonance absorption," *J. Phys. Soc. Jpn.*, vol. 9, no. 6, pp. 888–919, 1954.

[120] D. G. Nishimura, *Principles of Magnetic Resonance Imaging.* Stanford University, 1996.

[121] D. Pines and C. P. Slichter, "Relaxation times in magnetic resonance," *Phys. Rev.*, vol. 100, pp. 1014–1020, Nov 1955.

[122] J. Stepišnik, "Time-dependent self-diffusion by {NMR} spin-echo," *Physica B*, vol. 183, no. 4, pp. 343 – 350, 1993.

[123] T. Li, S. Kheifets, D. Medellin, and M. G. Raizen, "Measurement of the instantaneous velocity of a brownian particle," *Science*, vol. 328, no. 5986, pp. 1673–1675, 2010.

[124] R. Huang, I. Chavez, K. M. Taute, B. Lukić, S. Jeney, M. G. Raizen, and E.-L. Florin, "Direct observation of the full transition from ballistic to diffusive brownian motion in a liquid," *Nature Phys.*, vol. 7, no. 7, pp. 576–580, 2011.

[125] T. Franosch, M. Grimm, M. Belushkin, F. M. Mor, G. Foffi, L. Forró, and S. Jeney, "Resonances arising from hydrodynamic memory in brownian motion," *Nature*, vol. 478, no. 7367, pp. 85–88, 2011.

[126] S. Kheifets, A. Simha, K. Melin, T. Li, and M. G. Raizen, "Observation of brownian motion in liquids at short times: Instantaneous velocity and memory loss," *Science*, vol. 343, no. 6178, pp. 1493–1496, 2014.

[127] S. F. Nørrelykke and H. Flyvbjerg, "Harmonic oscillator in heat bath: Exact simulation of time-lapse-recorded data and exact analytical benchmark statistics," *Phys. Rev. E*, vol. 83, no. 4, p. 041103, 2011.

[128] S. Chapman and T. G. Cowling, *The Mathematical Theory of Non-Uniform Gases: an Account of the Kinetic Theory of Viscosity, Thermal Conduction and Diffusion in Gases.* Cambridge University Press, 1970.

[129] W. Haynes, *CRC Handbook of Chemistry and Physics.* CRC Press, 2014-2015.

[130] W. Sutherland, "Xxv. molecular diameters," *Phil. Mag.*, vol. 17, no. 98, pp. 320–321, 1909.

[131] G. Uhrig, "Keeping a quantum bit alive by optimized π-pulse sequences," *Phys. Rev. Lett.*, vol. 98, p. 100504, Mar 2007.

[132] D. S. Grebenkov, "Nmr survey of reflected brownian motion," *Rev. Mod. Phys.*, vol. 79, no. 3, p. 1077, 2007.

[133] G. Q. Zhang and G. J. Hirasaki, "Cpmg relaxation by diffusion with constant magnetic field gradient in a restricted geometry: numerical simulation and application," *J. Magn. Reson.*, vol. 163, no. 1, pp. 81 – 91, 2003.

[134] L. J. Zielinski and M. D. Hürlimann, "Probing short length scales with restricted diffusion in a static gradient using the cpmg sequence," *J. Magn. Reson.*, vol. 172, no. 1, pp. 161–167, 2005.

[135] R. W. Mair, G. Wong, D. Hoffmann, M. D. Hürlimann, S. Patz, L. M. Schwartz, and R. L. Walsworth, "Probing porous media with gas diffusion nmr," *Phys. Rev. Lett.*, vol. 83, no. 16, p. 3324, 1999.

[136] M. Hurlimann, K. Helmer, T. Deswiet, and P. Sen, "Spin echoes in a constant gradient and in the presence of simple restriction," *J. Magn. Reson., Ser A*, vol. 113, no. 2, pp. 260–264, 1995.

[137] T. M. de Swiet and P. N. Sen, "Decay of nuclear magnetization by bounded diffusion in a constant field gradient," *J. Chem. Phys.*, vol. 100, no. 8, pp. 5597–5604, 1994.

[138] P. N. Sen, A. André, and S. Axelrod, "Spin echoes of nuclear magnetization diffusing in a constant magnetic field gradient and in a restricted geometry," *J. Chem. Phys.*, vol. 111, no. 14, pp. 6548–6555, 1999.

[139] P. Le Doussal and P. N. Sen, "Decay of nuclear magnetization by diffusion in a parabolic magnetic field: An exactly solvable model," *Phys. Rev. B*, vol. 46, pp. 3465–3485, Aug 1992.

[140] E. L. Cussler, *Diffusion: Mass Transfer in Fluid Systems.* Cambridge University Press, 2009.

[141] W. Ferstl, T. Klahn, W. Schweikert, G. Billeb, M. Schwarzer, and S. Loebbecke, "Inline analysis in microreaction technology: A suitable tool for process screening and optimization," *Chem. Eng. Technol.*, vol. 30, no. 3, pp. 370–378, 2007.

[142] R. W. Adams, J. A. Aguilar, K. D. Atkinson, M. J. Cowley, P. I. Elliott, S. B. Duckett, G. G. Green, I. G. Khazal, J. López-Serrano, and D. C. Williamson, "Reversible interactions with para-hydrogen enhance nmr sensitivity by polarization transfer," *Science*, vol. 323, no. 5922, pp. 1708–1711, 2009.

[143] C. R. Bowers and D. P. Weitekamp, "Parahydrogen and synthesis allow dramatically enhanced nuclear alignment," *J. Am. Chem. Soc.*, vol. 109, no. 18, pp. 5541–5542, 1987.

[144] T. C. Eisenschmid, R. U. Kirss, P. P. Deutsch, S. I. Hommeltoft, R. Eisenberg, J. Bargon, R. G. Lawler, and A. L. Balch, "Para hydrogen induced polarization in hydrogenation reactions," *J. Am. Chem. Soc.*, vol. 109, no. 26, pp. 8089–8091, 1987.

[145] S. B. Duckett and N. J. Wood, "Parahydrogen-based nmr methods as a mechanistic probe in inorganic chemistry," *Coord. Chem. Rev.*, vol. 252, no. 21, pp. 2278–2291, 2008.

[146] K. V. Kovtunov, I. E. Beck, V. I. Bukhtiyarov, and I. V. Koptyug, "Observation of parahydrogen-induced polarization in heterogeneous hydrogenation on supported metal catalysts," *Angew. Chem. Int. Ed.*, vol. 47, no. 8, pp. 1492–1495, 2008.

[147] R. Sharma and L.-S. Bouchard, "Strongly hyperpolarized gas from parahydrogen by rational design of ligand-capped nanoparticles," *Sci. Rep.*, vol. 2, 2012.

[148] R. Kubo, *A Stochastic Theory of Line Shape.* John Wiley & Sons, Inc., 2007.

[149] S. Whitaker, "Local thermal equilibrium: an application to packed bed catalytic reactor design," *Chem. Eng. Sci.*, vol. 41, no. 8, pp. 2029–2039, 1986.

[150] S. Torquato, *Random Heterogeneous Materials: Microstructure and Macroscopic Properties*, vol. 16. Springer Science & Business Media, 2013.

[151] S. Whitaker, *The Method of Volume Averaging*, vol. 13. Springer Science & Business Media, 2013.

[152] M. Quintard and S. Whitaker, "Transport in ordered and disordered porous media: volume-averaged equations, closure problems, and comparison with experiment," *Chem. Eng. Sci.*, vol. 48, no. 14, pp. 2537–2564, 1993.

[153] D. Johnston, "Stretched exponential relaxation arising from a continuous sum of exponential decays," *Phys. Rev. B*, vol. 74, no. 18, p. 184430, 2006.

[154] H. Deng, C. J. Doonan, H. Furukawa, R. B. Ferreira, J. Towne, C. B. Knobler, B. Wang, and O. M. Yaghi, "Multiple functional groups of varying ratios in metal-organic frameworks," *Science*, vol. 327, no. 5967, pp. 846–850, 2010.

[155] C. J. Doonan, W. Morris, H. Furukawa, and O. M. Yaghi, "Isoreticular metalation of metal- organic frameworks," *J. Am. Chem. Soc.*, vol. 131, no. 27, pp. 9492–9493, 2009.

[156] S. R. Burt, *MRI of Heterogeneous Hydrogenation Reactions Using Parahydrogen Polarization.* PhD thesis, University of California at Berkeley, 2008.

[157] M. Albert, G. Cates, B. Driehuys, W. Happer, B. Saam, C. Springer, and A. Wishnia, "Biological magnetic resonance imaging using laser-polarized 129xe," *Nature*, 1994.

[158] J. P. Butler, S. H. Loring, S. Patz, A. Tsuda, D. A. Yablonskiy, and S. J. Mentzer, "Evidence for adult lung growth in humans," *N. Engl. J. Med.*, vol. 367, no. 3, pp. 244–247, 2012.

[159] F. C. Horn, H. Marshall, G. J. Collier, R. Kay, S. Siddiqui, C. E. Brightling, J. Parra-Robles, and J. M. Wild, "Regional ventilation changes in the lung: Treatment response mapping by using hyperpolarized gas mr imaging as a quantitative biomarker," *Radiology*, p. 160532, 2017.

[160] S. Mori and J. Zhang, "Principles of diffusion tensor imaging and its applications to basic neuroscience research," *Neuron*, vol. 51, no. 5, pp. 527–539, 2006.